GRAIN-SCALE SUBCRITICAL FRACTURE IN ROCK: STATISTICAL MECHANICAL MODELING AND DISCOVERY OF TWO PHYSICALLY DISTINCT SUBCRITICAL FRACTURE MODES

by

Mehdi Morovati

A dissertation submitted to the faculty of
The University of North Carolina at Charlotte
in partial fulfillment of the requirements
for the degree of Doctor of Philosophy in
Mechanical Engineering

Charlotte

2024

Approved by:

Dr. Russell Keanini

Dr. Stuart Smith

Dr. Martha Cary Eppes

Dr. Wesley Williams

ABSTRACT

MEHDI MOROVATI. Grain-Scale Subcritical Fracture in Rock: Statistical Mechanical Modeling and Discovery of Two Physically Distinct Subcritical Fracture Modes. (Under the direction of DR. RUSSELL KEANINI)

Part I: An equilibrium statistical mechanics framework for investigating microfracture in rocks is proposed and tested. The framework consists of three elements: A) A simplified energy-based model describing atomic- to grain-scale mechanical and thermal rock fracture, B) A macroscopic, grain-scale statistical mechanics model that postulates existence of (thermomechanical) equilibrium, where (over appropriate timescales) rates of grain-scale microfracture (nominally) match rates of microfracture healing, and C) A resultant theoretical prediction connecting measurable fracture-induced acoustic emission (AE) with rock temperature. Comparisons of theoretical, temperature-dependent AE with AE observed during cyclic rock heating and cooling experiments support the validity of the model. Importantly, the results suggest that, for a given rock type - whether in pristine volumes devoid of grain-scale cracks or within volumes containing such cracks - the number of microfractures within the volume can be reasonably estimated as a calculable function of temperature and confining pressure, regardless of the rock's geological and weathering history.

PART II: The second part of the dissertation recasts traditional dimensional correlations between experimentally measured (tensile-driven) subcritical fracture speed, $\frac{da}{dt}$, and imposed stress intensity, K_I, in dimensionless form. To the best of our knowledge, all existing correlations are well-described by the so-called (dimensional) Charles crack growth law: $\frac{da}{dt} = AK_I^n$ where a, t, A, K_I and n are, respectively, crack length, time, a rock-dependent (constant) prefactor, stress intensity, and subcritical crack growth index. Puzzlingly, however, in granite and similar fine-grained rock, experimentally determined n's are anomalously large, on the order of 40 to 150 [1].

To tackle this puzzle, we apply dimensional analysis to existing (and difficult to obtain) Charles law correlations, recasting these in dimensionless form. While this practice is de rigueur in, e.g., fluid mechanics, physics, and heat transfer, it is new in the area of fracture mechanics. Importantly, recasting Charles' law in appropriate dimensionless form exposes two distinct regimes of subcritical fracture in rock: A) A slow growth regime, extant at stress intensities below a well-defined threshold, in which sub grain-scale cracks grow slowly along grain boundaries; and B) A fast subcritical growth regime, extant at stress intensities above the threshold, in which cracks grow intermittently across multiple grains. We show that each regime is well-captured by dimensionless Charles' law correlations, where slow regime n's are on the order of 1, and fast regime n's are clustered around approximately 4 to 6.

Crucially, these findings will allow development of improved, predictive crack growth models, suitable for predicting and interpreting geologically ubiquitous subcritical fracture in surface and near-surface rock, both on earth and on extraterrestrial bodies.

DEDICATION

To my cherished parents, whose steadfast encouragement and unwavering support have been the bedrock of my journey toward earning a Ph.D. Your belief in my dreams and your unwavering dedication to my educational pursuits have provided the foundation upon which I have built this academic achievement. Your sacrifices and love have guided me through the years, and it is with the deepest gratitude and profound affection that I dedicate this dissertation to you.

Additionally, to my esteemed advisor, Dr. Russell Keanini, whose exceptional mentorship and support proved invaluable, particularly during the challenging times of the COVID-19 pandemic. Your guidance, unwavering commitment to my research, and your timely assistance were instrumental in enabling me to persevere in my academic pursuits. I am forever grateful for your mentorship and encouragement. This dissertation stands as a tribute to the lasting impact of both my parents and Dr. Russell Keanini on my academic journey and research endeavors.

ACKNOWLEDGEMENTS

I would like to express my deepest gratitude to my parents for their unwavering mental, emotional, and financial support throughout my doctoral journey. Their encouragement and belief in me have been the bedrock of my success, and I could not have reached this milestone without their guidance and sacrifices.

I would also like to extend my heartfelt appreciation to Dr. Russell Keanini for her outstanding leadership, constant encouragement, and invaluable mentorship throughout this dissertation process. Her guidance has been instrumental in shaping both this work and my development as a researcher.

My sincere thanks go to the members of my dissertation committee, Dr. Stuart Smith, Dr. Martha Cary Eppes and Dr. Wesley Williams, for their insightful feedback, dedication, and expertise in fostering my academic growth. I am also grateful to Prof. Terry Xu and the Mechanical Engineering Department for their essential support through teaching assistantships, which provided both financial stability and academic enrichment.

Lastly, I would like to acknowledge the University for its generous support through GASP grants, which were vital in facilitating my research and academic progress.

PREFACE

This thesis explores two distinct yet interconnected areas of rock mechanics, offering novel approaches to understanding crack behavior in geological materials. The work is divided into two main sections, each contributing to our comprehension of rock fracture mechanics from different perspectives.

The first section, "Statistical Mechanics of Crack Initiation and Propagation in Rocks," applies principles of statistical mechanics to develop and derive formulas simulating crack propagation across various rock types. This approach provides a robust framework for predicting and analyzing the complex behavior of cracks in heterogeneous geological materials. The second section, "Dimensional Analysis as a Tool for Exposing Slow and Fast Subcritical Fracture Modes in Rocks," focuses on deriving dimensionless formulas for crack velocity and stress intensity factor. This innovative application of dimensional analysis enables the distinction between two primary crack regimes in rocks, offering new insights into subcritical fracture behavior. Together, these sections aim to advance our understanding of rock fracture mechanics and provide valuable tools for both theoretical analysis and practical applications in geotechnical engineering and related fields.

TABLE OF CONTENTS

LIST OF TABLES

LIST OF FIGURES

CHAPTER 1: INTRODUCTION

Fracture and cracking in different rock types is a complex phenomenon that occurs across multiple scales, from atomic bonds within mineral grains to large-scale faults spanning miles. Understanding the mechanics of rock fracture is a key for many engineering applications as well as for fundamental geophysics and geology. The first part of this dissertation leverages concepts from statistical physics and fracture mechanics to develop improved models of rock fracture, with a focus on acoustic emissions resulting from microfractures.

The framework put forward integrates three main components including an energy-based model describing fracture initiation and propagation at the grain scale, a statistical model for the distribution and abundance of microcracks within a rock volume, and a bridge relation that connects the model predictions to experimentally measurable acoustic emissions. This integrated framework is applied to acoustic emission data sets from three experimental studies of fracture in rock samples under thermal and mechanical loading.

A key finding is that for a given rock type and pristine sample volume, the number of microfractures can be estimated as a function of temperature and confining pressure regardless of geologic history. This points to fundamental physics underlying the microfracture process.

The second part of the dissertation outlines the dimensional analysis which I used to express given tensile-driven subcritical fracture speed as a function of imposed stress intensity factor in dimensionless form, and also how the applied dimensionless formulas resulted in exposing two distinct modes of subcritical fracture.

In other words, by applying the derived dimensionless formulas on both crack velocity and stress intensity factor in rocks, two regimes of subcritical crack growth called slow growth along grain boundaries and fast, sequential fractures across multiple grains are distinguishable. Moreover, as a result of this analysis, quantitative indices, i.e., subcritical crack growth index on both regimes are extracted to characterize these regimes.

CHAPTER 2: LITERATURE REVIEW

Comprehending and forecasting the phenomenon of rock fracture has been a foundational challenge in the field of geology for over a century [8]. Many researchers have studied crack initiation and propagation in different rock types using different techniques ([9], [10], [11]). Addressing rock fracture issues involves the utilization of diverse observational and experimental methodologies, and, since the 1970s, numerical modeling and experimental approaches have been increasingly employed in this pursuit.

Some researches have done some studies to explore landscape formation considering rock fracture as one of the main elements. Hales et al developed a 1D thermal transfer simulation. This model aimed to forecast the extent and strength of ice separation within the underlying rock layers, taking into account yearly temperature averages and fluctuations. [12]. Clarke et al conducted a comparative study of two mountain ranges in New Zealand - the Southern Alps and Fiordland - to understand how bedrock fracturing influences landscape morphology and landsliding [13]. Scott et al conducted a review and synthesis of research on how bedrock fractures influence geomorphic processes and landform development across various spatial scales and geomorphic domains (hillslope, glacial, fluvial, coastal) [14].

Seismicity as one to popular topic which can be originated from rock fracture in high depth has been explored by researchers. Cook measured and analyzed deformation and seismic activity in the rock mass around underground excavations created by mining. This included installing seismic monitoring networks and precise instruments to measure rock displacements and strains. [15]. House conducted a study in crystalline rock that focused on identifying micro earthquakes triggered by hydraulic fracturing at depth [16]. Meredith et al conducted controlled fracture experiments on rocks while monitoring acoustic emission and b-values, proposed a model connecting b-value variations to the physical failure process, and demonstrated consistency between model predictions, lab data and some field observations. This provided insights into using seismicity changes as failure precursors [17].

Some research has explored how climate change impacts rock failure. Marshall studied the use of stable isotopic data from marine limestones and various terrestrial carbonates to understand ocean circulations and shifts in global climate. Stable isotopes, specifically oxygen and carbon isotopes, can provide quantitative evidence for environmental changes over time[18]. Gruber et al analyzed evidence linking warming permafrost to increased rock slope failures, including observations of massive ice exposures after failures and increased activity during hot periods. They also discussed physical processes that could link warming/thawing permafrost to slope destabilization, like loss of ice bonding, volume expansion, ice segregation, hydro-static pressure changes [19]. Eppes et al developed theoretical models grounded in fracture mechanics to argue for the climate dependence of subcritical cracking in rocks, validated and applied these models using available data, and explored variability and implications for relating climate and weathering [20]. Liu et al generated an innovative thermo-hydro-mechanical coupling model for frozen cracked and fractured rocks, studied key coupling parameters, and validated the model's ability to simulate complex freezing and thawing processes seen in cold region rock engineering [21]. Hall convincingly argued that thermal stresses significantly contribute to rock weathering in cold regions, a factor that has often been underestimated. The high-resolution data they presented reveals this potential [22]. Gage et al monitored relevant temperatures in situ along this escarpment to demonstrate the potential for the processes of freeze-thaw and thermal weathering, dependent on site factors like aspect and lithology. They highlighted the key role fractures play in moderating these mechanisms [23]. Eppes et al conducted an 11-month field study monitoring the cracking activity and environmental conditions of a granite boulder situated on the ground surface and found out that most cracking events coincided with times of peak solar-induced thermal stresses, and that weather changes driving surface temperature fluctuations appeared to trigger event clusters. This indicates that thermal stresses are a significant factor in rock breakdown processes [24]. Sumner et al found out that solar-induced thermal stresses play a crucial role in rock weathering across different environments, and they challenge some established notions about weathering "zones". Also, they concluded that more research is still needed into moisture conditions and interactions between thermal stresses and other weathering mechanisms [25]. Walder et al developed a physics-based framework for understanding and predicting frost crack growth in rocks by considering ice pressurization from water migration. Key factors are temperature regime, cooling rate, and time [26]. Alneasan et al investigated how temperature and loading mode mixity affect fracture parameters of mudstone using thermally treated SCB specimens tested under bending. The increasing brittleness with heating explained the improved fracture resistance [27]. Krautblatter et al investigated the effects of warm temperature on rocks stability. krautblatter2013permafrost [28]. Warren et al instrumented a natural granite boulder with sensors to measure acoustic emissions (AE), surface temperature, surface strain, and moisture content. The instrumentation system enables simultaneous, high-resolution monitoring of rock fracturing and environmental variables to decode mechanical weathering processes and their potential changes with climate [29]. Akara et al developed an integrated hydrologic model, evaluated future regional climate projections, and used the model to quantify potential impacts of climate change on groundwater and surface water resources in the study watershed [30]. Murton et al performed controlled freezing experiments, modeled fundamental processes, analyzed field evidence, and developed a conceptual model for ice segregation and fracture in cold region bedrock. This helped elucidate the mechanisms and impacts of climate changes on permafrost rock stability [31]. Han et al performed integrated mechanical testing, high-speed imaging, pore-scale analysis, and process-based evaluation to examine the fracture behavior of frozen sandstone at various temperatures relevant to cold-regions engineering [32].

Different studies have investigated subcritical crack growth in different rock types under varying environmental conditions, including different water pH levels, humidity, and temperature gradients. Nara et al., investigated subcritical cracking in rocks immersed in distilled water and sodium hydroxide solution with varying water pH levels using the double-torsion test [33]. Nara et al studied the electrolyte concentration influence in water on subcritical cracking growth in two different sandstones called Berea sandstone which has few clay minerals, and Shirahama sandstone which contains clay minerals. They found that electrolyte concentration significantly influences subcritical crack growth in clay-bearing sandstone but not in sandstone without clays. The effects are related to electric double layer thickness and clay condensation [34]. Nara et al investigated subcritical crack growth in two different types of marble called Carrara marble (CM) and Macedonian marble (MM) under different environmental conditions, i.e., different temperature and humidity, both in air and. For CM in air, they observed a region at higher crack velocities where the slope in crack velocity versus stress intensity factor plot decreased which is similar to Region II subcritical crack growth seen in glass, where crack velocity is controlled by transport of the reactive agent (water) to the crack tip. Region II is not typically seen in rocks since they contain water intrinsically [35]. Cao et al examined experimental subcritical crack growth rate data across different rock types using a consistent testing methodology.

The obtained results demonstrated time-dependent crack growth behavior in various rocks that is dependent on rock elastic properties which has implications for long-term stability in rock engineering applications [36]. Jinyin et al aimed to systematically compare the fracture toughness, subcritical crack growth behavior, and resulting long-term strength estimates across different rock types using double-torsion testing and 3D digital image correlation imaging. The earned results would help guide selection of optimal rocks for long-term stable underground engineering applications [37]. Nara et al investigated the calcium ions impact on subcritical crack growth in granite using double torsion tests. They observed that subcritical crack growth velocity was lower in a calcium hydroxide solution compared to distilled water. In addition, precipitation of calcium compounds was observed on crack surfaces from the solution, likely inducing crack tip closure and lowering velocity [38]. explored a comprehensive approach to understanding subcritical crack growth and fracture behavior. They concluded that the unified approach proposes micromechanical processes govern crack initiation and growth instead of extrinsic factors like crack closure. In addition, it connects smooth, notched, and cracked specimen behavior under monotonic and cyclic loading through a physics-based understanding [39]. Ji et al developed a computational method to analyze subcritical crack growth in underground excavations subjected to mode I tensile loading. For the subcritical crack growth model, they a dynamic time step control method to strike a balance between accuracy and computational efficiency. They also proposed a method to estimate the initial crack size for field-scale applications [40].

Thermoelastic fractures has been studied by some researchers to see the effect of temperature gradient in crack propagation. Wang et al in 1989 investigated studied thermal cracking and microfractures in different rock types under a set of confining pressure using observational and experimental techniques [2].

Beyond environmental conditions, some rocks properties such as anisotropy, etc can affect the crack propagation rate in rocks. Nara et al conducted double-torsion experiments on granite sample with different orientations to observe crack propagation pattern. They found that cracks propagated faster parallel to the plane with more microcracks compared to the plane with fewer microcracks [41].

Furthermore, subcritical crack growth in rocks have been studied considering different techniques such as double torsion test to see the effect of different techniques in crack propagation rates and patterns. Nara et al conducted double torsion experiments on andesite to study subcritical crack growth. They tested different guide groove shapes and found a rectangular shape gave the most reproducible results [42]. Tae et al applied constant stress-rate test to get the relationship between fracture strength and stress rate to determine subcritical parameters without needing to measure crack propagation velocity or crack length which ends to characterize subcritical crack growth in rocks, providing an alternative to the conventional double-torsion test [43]. Robina et al explored the effect of cyclic heating on subcritical cracking under bending test. They used linear elastic fracture mechanics to calculate stress intensity factors and relate them to crack velocity via a power law, and also employed the compliance method to interpret crack growth based on crack mouth opening displacement [44]. Jinyin et al performed relaxation and rapid displacement loading tests on 5 rock types to study differences in subcritical crack growth and dynamic fracture. [45]. Tao et al investigated real-time Mode I and Mode II subcritical crack growth behavior in gypsum rock using a new DC voltage fluctuation method. Their new method has enabled real-time monitoring of entire subcritical crack growth process and accurate measurement of velocities. Also, the obtained results give insight into time-dependent rock fracture stages and quantitative relationships between crack growth, load, and mode [46].

Different experimental techniques have been applied by researchers to study subcritical cracks in different rock types under different conditions. Heating and cooling experiments is among those techniques which has been addressed by some researchers. Mahmutoglu provided useful insights into how fractures influence mechanical properties and failure modes of rocks by using controlled heating and cooling to simulate the effects. The technique could be useful for studying fractured rock behavior [47]. Takaerli et al systematically characterized the effects of repeated heating/cooling cycles on granitic rocks (both dried and water-saturated) through detailed physical and mechanical testing. They also examined the effect of microstructural changes from the thermal cycling on mechanical properties like compressive strength and elastic modulus. This was done through uniaxial compression tests on fresh and thermally aged samples [48]. Rutqvist et al conducted analysis and modeling of air permeability response to thermal loading and unloading to study coupled Thermal-Hydrological-Mechanical (THM) processes and identify potential irreversible hydrologic changes in the fractured rock [49]. Johnson et al investigated the formation of thermally-induced microcracks in two types of rocks, Sioux quartzite and Westerly granite, when subjected to slow and uniform temperature changes. The goal was to understand the mechanisms behind the development of microcracks in these rocks due to intergranular thermal stresses [50]. Meredith et al provided insights into the thermo-mechanical behavior of volcanic rocks, highlighting the importance of microstructure and mineral composition in controlling thermal cracking and presenting implications for understanding magma chamber dynamics [51]. Yin et al conducted a study in which they developed a PFC2D (Particle Flow Code in 2 Dimensions) model based on the XRD (X-ray diffraction) component distribution of a granite specimen. They employed discrete element method to build their model, and its parameters were calibrated using data from uniaxial compression tests on the granite specimen [52]. Wu et al investigated thermally treated granite specimens, analyzed the resulting changes in microstructure, and related this to effects on key thermal/transport properties relevant for geothermal energy applications [53]. Ge et al established an experiment to investigate the mechanical behavior of rock subjected to heating and cooling cycles. Their findings have implications for deep geo-engineering applications, including geothermal energy extraction, geological disposal of nuclear waste, and tunnel fire safety. [54]. Wu et al subjected granite samples to various heating/cooling treatments and analyzed the resulting changes in physical properties, tensile strength, and fracture surface characteristics in detail [55]. Kang et al performed integrated experiments subjecting granite samples to various heating/cooling treatments and thoroughly characterized the resulting physical, mechanical, and cracking behavior [56]. Du et al performed integrated experiments and simulations to analyze the fracturing effects of liquid nitrogen cooling on coal and sandstone samples. The focus was explaining the differences in physical damage and permeability enhancement observed between the two rock types [57]. Li et al performed numerical simulations and experiments to explore the thermal cooling capacity of shale under different cooling modes, particularly focusing on thermal shock caused by the injection of cryogenic fluids [58]. Pan et al conducted to investigate the thermal shock damage effect on the physical and mechanical properties of granite and limestone in different cooling media, including air, water, and high-viscosity liquid [59]. Isaka et al sought to characterize the changes in mechanical properties and provide a detailed microstructural analysis of Harcourt granite subjected to various pre-heating temperatures and two cooling methods called rapid and slow [60]. Shen et al aimed to explore the effects of different cooling methods on high-temperature granite, particularly in the context of geothermal energy exploitation and breaking hard rocks in deep geo-engineering [61]. Browning et al performed integrated heating/cooling experiments on volcanic rock samples, monitoring acoustic emissions contemporaneously. They demonstrated and explained why thermal cracking is dominated by the cooling phase, relating microcrack observations to changes in physical properties [62]. Daoud et al performed integrated heating/cooling experiments on different rock types, analyzing acoustic emissions to quantify contemporaneous thermal cracking. They identified important microstructural controls leading to distinct cracking behaviors, proposing a "temperature memory effect" analogy [63]. Zhang et al studied the characteristics and underlying mechanisms controlling thermal cracking in granite through well-designed heating/cooling experiments along with quantitative image analysis and comparison against literature data. Their findings can help better understand thermal damage and fracturing processes relevant for deep geothermal energy and other rock engineering applications [64]. Zhu et al studied how cyclic heating/cooling affected granite strength, damage accumulation, and failure modes using mechanical testing coupled with acoustic emission monitoring and quantitative analysis [65]. Kim et al studied how rapid cooling induced thermal stresses affected cracking and mechanical properties in a variety of rock types using coupled experimental-modeling approaches [66]. Wu et al systematically characterized the physical, mechanical, and microstructural damage in granite caused by liquid nitrogen cooling after heating. The extremely low temperature of liquid nitrogen leads to more intense thermal shocking and damage of hot rock [67]. Rong et al systematically studied the progressive physical, mechanical, and microstructural damage in granite through cyclic heating and liquid nitrogen quenching experiments along with quantitative analysis [68]. Wang et al explored how rapid cooling with water, air, or liquid nitrogen affected heated granite samples. Also, they studied granite subjected to up to 24 cycles of heating to 300 $°C$ followed by liquid nitrogen or air cooling [69]. Shen et al experimentally induced and analyzed thermal shock cracks, modeled the process in simulations, and analyzed the underlying mechanisms [70]. Yin et al concentrated on investigating the effect of cyclic heating and cooling treatments on mode I fracture characteristics of granite, particularly in the context of geothermal reservoirs. The research involved fracture tests using semi-circular bend specimens, monitoring acoustic emission (AE) events, analyzing the morphology of fracture surfaces, measuring open porosity, and using scanning electron microscopy (SEM) to study variations in microstructure [71]. Li et al studied the detrimental thermal shock effects on granite and sandstone in enhanced geothermal systems. Both inter- and intra-granular cracks induced by temperature changes and cold water injection compromise the rock's microstructural integrity and mechanical properties. The findings underscore the importance of considering cooling rates and temperature gradients in geothermal reservoir management [72].

Nara et al investigated the effects different environmental conditions such as relative humidity and temperature on subcritical crack growth in two igneous rocks called andesite and granite. This experimental study found humidity has a very strong influence on subcritical crack propagation in igneous rocks, beyond what stress corrosion theory predicts. The implications are important for underground construction and time-dependent rock strength [73]. Andersson et al systematically characterized the sulfur defects on pyrite surfaces using a combined experimental spectroscopy and computational modeling approach. This allowed them to systematically introduce defects [74]. Chang et al conducted an experimental and modeling study to explore fracture and damage mechanisms in rocks under triaxial compression using acoustic emission (AE) monitoring and moment tensor analysis. They combined advanced AE monitoring and moment tensor analysis techniques to relate microscale fracture processes to macroscale failure in rocks under triaxial compression [75]. Chichinina et al showed via theory and experiments that seismic attenuation anisotropy provides additional insight into fractured transversely isotropic (TI) media compared to just velocity anisotropy, and can help distinguish between liquid versus gas saturation of fractures [76]. Vernik et al investigated the physical properties of black, kerogen-rich shales through a series of experiments, including maturation analysis, SEM observations, and physical modeling [77]. Mollhoff et al demonstrated and compared different techniques for estimating rock fracture compliance from elastic wave data, providing guidance on the most reliable approaches which highlights the potential of using seismic phase delays for fracture characterization [78]. Fair et al studies the mechanical anisotropy and fracture behavior of the layered perovskite. They found that the large elastic and fracture anisotropy of the layered perovskite structure enables easy interlayer damage and crack deflection, resulting in soft, deformable mechanical characteristics. The weak interlayer bonding is the key factor determining this behavior [79]. Goldsby et al studied behavior of rocks at the microscopic level, particularly on the contacting asperities on the sliding surface. They employed rate and state-variable friction laws, which are commonly used to describe the frictional rocks behavior in laboratory settings and are often applied in earthquake models. These laws capture a diverse range of natural phenomena associated with earthquakes [80]. Haifeng et al analyzed the dynamics of hydraulic fracture propagation and interaction with natural fractures in shale reservoirs using principles of rock fracture mechanics and their obtained results provide insights into designing hydraulic fracturing treatments in these unconventional reservoirs [81]. He et al simulated rock burst near underground excavations by running laboratory tests on limestone samples under triaxial loading conditions, with sudden unloading of one horizontal stress [82].

Kendelewicz et al characterized the early stages of pyrite oxidation using surface-sensitive XPS to gain insight into the atomic-level mechanisms, especially regarding the roles of O2 and H2O. Also, they concluded oxygen can oxidize pyrite without water present, contradicting the assumption water is required for pyrite oxidation [83].

Understanding the mechanical properties of cracked rocks and the relationship between weathering and rock fracture is a key area of research, as it plays a significant role in crack formation. Many researchers are actively studying these topics. Dverstorp et al used a calibrated discrete fracture network model to study tracer migration in sparsely fractured rock, offering valuable insights into the intricate behavior of fluid flow and transport within these geological formations [84]. Sagy et al analyzed an interesting natural joint system, experimentally simulated similar features in the lab, and used comparisons between the field and experiments to infer dynamic joint propagation and a possible mechanism for high fracture densities in layered rocks [85]. Pachero et al conducted a study focused on weathering in a fractured rock environment made up of granites and metasediments in northern Portugal [86]. Hasenmueller et al extensively characterized the physical, chemical and biological properties of deep tree root systems and associated bedrock fractures in order to understand root-rock interactions and weathering processes [87]. Lebedeva et al developed theoretical models spanning scales from individual fractures to whole hillslopes to elucidate controls on bedrock weathering rates and block size distributions in weathering profiles [88]. Cuccuru et al investigated the physical and mechanical behavior of weathered granite through a combination of physical mechanical experiments and microstructural analysis. Their fieldwork and microscopy revealed that a widespread microfracture system had developed along pre-existing magmatic quartz anisotropies [89]. The study of the Royne et al revealed a feedback where chemical reactions generate stresses that propagate fractures, which in turn accelerate weathering by exposing new reactive surfaces, generating a hierarchical structure that nonlinearly enhances total reaction rates [90]. Zhang et al carried out an in-depth study examining how weathering and fracturing affect the physical properties and distribution of oil and gas in various volcanic rock types within the Junggar Basin [91]. Eppes et al conducted an 11-month experiment monitoring cracking activity and environmental conditions on the surface of a granite boulder sitting in open sun [24]. Hall et al conducted weathering studies with a focus on rock temperature data. They identified a major limitation in existing studies, which was the lack of rock temperature data collected at sufficiently frequent intervals [92]. Ehlen conducted a study on the variability of weathered materials, specifically weathered granite, for geotechnical characterization in the context of engineering purposes. The focus was on understanding the connections between fracture patterns and weathering grades in rock. The study involved investigating fracture characteristics in 13 exposures of weathered granite across five study areas in eastern Asia [93]. Eppes et al investigated the cracks formation as a crucial aspect of physical weathering processes in desert environments, specifically in the Mojave (U.S.), Gobi (Mongolia), and Strzelecki (Australia) deserts. The research combines new field data to support the hypothesis that cracks with orientations not readily attributable to rock anisotropies or shape in boulders or cobbles are generated by tensile stresses from directional heating and cooling during the sun's daily movement [94]. Marechal et al investigated a test catchment composed of hard bedrock. They focused on analyzing the water flow characteristics within the weathered and fractured upper layer. To accomplish this, they employed a variety of hydraulic experiments conducted at multiple scales [95]. Aldred et al studied how temperature fluctuations caused by sunlight contribute to rock degradation in regions with moderate, moist climates. Their research focused on understanding the impact of these thermally-induced pressures on the physical disintegration of stone materials [96].

Segall et al examined a single steeply dipping joint set in the Mount Givens Granodiorite, central Sierra Nevada, to clarify the mechanics of fracture and joint formation in granitic rocks. The joints, filled with fluids depositing epidote and chlorite, exhibited relative displacements normal to the joint surfaces, ruling out a shear origin [97]. Zhao et al systematically studied how pre-crack geometry and crack stop holes impact strength, failure modes, and energy evolution in granite under uniaxial compression which could help optimize underground excavation and slope stability in jointed granite rock masses [98]. Yan et al discussed how the crack geometry (parallel, uniform cracks) and dominant effect of high strain rate loading may explain why crack intensity did not affect fragmentation and dissipation as much [99]. Qi et al performed compression tests on three distinct rock samples featuring various crack types to investigate their mechanical responses under different conditions. Utilizing an electro-hydraulic testing machine, they analyzed how crack dip angles affected compressive strength, stress-strain curves, and failure patterns [100]. Song et al developed a theoretical model to analyze seismic wave dispersion and reduction in fluid-saturated porous rocks with aligned cracks. The model incorporates poroelasticity theory and describes the cracks using poroelastic linear slip conditions [101]. Bastola et al used a lattice-spring based numerical modeling approach (LS-SRM) to study the progressive failure and mechanical properties of pre-cracked marble specimens and they considered both planar and non-planar cracks were considered [102].

Stress relaxation and fracture tests is one of experimental techniques which is being used by many researchers to study fracture in different types of rocks. Zafar et al analyzed the fracture processes under different time-dependent loading conditions using multiple monitoring techniques [103]. Zafar et al conducted a comprehensive experimental study using advanced techniques like acoustic emission and digital image correlation to investigate the micro-cracking processes during stress relaxation in brittle rocks, providing insights into the behavior and potential applications for underground structures [104]. Rinne provided a comprehensive model incorporating SCG in brittle rock materials, considering various loading conditions and demonstrating good agreement with laboratory experiments. Also, the findings contribute to a deeper understanding the time-dependent behavior of rocks and have implications for assessing rock stability in different contexts [105]. Zafar et al studied stress relaxation experiments and acoustic emission sensor calibration to explore the micromechanics of fractures in crystalline rocks under time-dependent loading conditions. Their findings have implications for understanding and predicting the behavior of rocks in scenarios involving time-dependent failure [106]. Liu et al studied the effect of stress relaxation durations on strength, crack growth, and failure patterns of granite using experiments, microscopy, and modeling. Key finding was the load-history dependent transition from brittle tensile cracking to shear-influenced mixed-mode failure when relaxation periods were included [107]. Yang et al examined the stress relaxation behavior and failure modes of pre-cracked granite specimens under different loading conditions. They conducted laboratory experiments including monotonic loading, multistage relaxation (holding strain constant), and multistage creep (holding load constant). They used acoustic emission sensors and digital image correlation to monitor the fracturing processes [108]. Xu et al conducted generalized stress relaxation tests on sandstone specimens under triaxial loading conditions. They used a 3D digital image correlation (DIC) system to monitor the surface strain evolution [109]. Lam et al examined stress relaxation behavior of brittle rocks (two types of limestone) using laboratory tests as well as how loading/unloading conditions affect stress relaxation in pre-cracked granite specimens [110]. Zhong et al conducted a biaxial compression test on a rhyolite rock specimen containing a pre-fabricated inverted U-shaped opening. They found that strain energy was stored elastically initially and then released through crack growth and propagation [111]. Atkinson comprehensively reviewed the state of knowledge of subcritical cracking of rocks, compile pertinent experimental data, discuss potential implications, and identify avenues for future research [112].

The exploration of natural and experimental thermal, mechanical, and chemical influences across extensive length and time scales is made possible by employing experimental techniques such as lidar and optical imaging on fractured rock. This methis is also has been used by some researchers. Lato et al a quantitative methodology to correct orientation biases inherent in static lidar scanning of rock slopes. This has enabled more reliable discontinuity analysis from lidar when optimal multi-scan coverage is not possible [113]. Voyat et al improved rock mass surveying by employing photogrammetry and laser scanning to create accurate 3D digital models. They automated discontinuity detection, ranging from interactive identification to macro-area selection with automatic segmentation [114]. Song et al developed and demonstrated a new real-rock microfluidic approach for lab-on-a-chip style investigation of geo-chemical processes in reservoir rock at the pore scale [115]. Wang et al systematically conducted laser irradiation experiments on granite samples while varying key parameters, and thoroughly analyzed the thermal-mechanical effects and quantified drilling/fracturing efficiencies and damages [116]. Zhou et al performed comprehensive lab experiments to understand the effects of elevated temperatures on the strength, deformation, fracturing behavior, and microstructure of flawed granite specimens containing pre-existing fissures [117]. Yang et al developed an experimental methodology to quantitatively characterize the hydromechanical behavior of argillaceous rocks under coupled moisture and mechanical loading conditions [118]. Kumari et al analyzed the thermal, microstructural, mechanical, and hydrological changes in granite caused by quenching treatment, to better understand its effects on reservoirs during thermal stimulation for geothermal energy applications [119]. Wang et al critically reviewed recent uses of atomic force microscopy (AFM), covering aspects such as surface topography, mechanical properties, surface dynamics, and advanced techniques like AFM-based infrared spectroscopy. Their studies aims to highlight the accessibility, versatility, limitations, and potential developments of AFM techniques in energy geoscience [120]. Otter et al conducted a study on photo-induced force microscopy (PiFM), a cutting-edge technique that combines atomic force microscopy with infrared spectroscopy. Their work involved reviewing the historical development, working principles, data acquisition, and evaluation of PiFM, comparing it to traditional geochemical methods [121]. Jahanbakhsh et al conducted a comprehensive review of micromodels and imaging techniques for visualizing fluid flow in porous media, focusing on their applications in geoscience and geo-energy engineering. Their study covered fabrication methods for micromodels, including glass-based, photoresist-based, polymer-based, silicon-based, and hybrid geomaterial-based micromodels [122]. Viswanathan et al conducted a comprehensive review of recent advances in fractured rock research, focusing on the prediction of natural and induced phenomena in subsurface formations. They emphasized the critical role of fractures in influencing fluid flow, solute transport, and mechanical behavior, particularly in the context of various applications such as CO2 sequestration, nuclear waste disposal, hydrogen storage, geothermal energy production, nuclear nonproliferation, and hydrocarbon extraction [123].

Gucsik et al examined both unshocked and experimentally shock-metamorphosed Hospital Hill quartzite from South Africa by employing cathodoluminescence images, spectroscopy, and Raman spectroscopy. The cathodoluminescence images of all samples revealed luminescent patchy areas and bands within non-luminescent quartz, along with dark irregular fractures [124]. Reed explained electron microprobe analysis to analyze small solid sample areas using a focused electron beam to excite X-rays which provides qualitative analysis by identifying characteristic lines in the X-ray spectrum and allows for quantitative determination of element concentrations with high accuracy and low detection limits [125].

Geophysical sounding is one of the other tools that helps researchers address geophysical studies. Lubczynsk et al applied magnetic resonance sounding (MRS)for groundwater applications. It highlights the need for further hydrogeological testing and interdisciplinary collaboration to develop MRS as a novel geophysical tool for water resource characterization for groundwater applications. Their study highlights the need for further hydrogeological testing and interdisciplinary collaboration to develop MRS as a novel geophysical tool for water resource characterization [126]. Mota et al applied multiple resistivity and self-potential techniques to characterize fracturing and contaminant transport at a waste disposal site. Their methods successfully detected likely leakage and fracture-guided propagation of landfill contamination into the surrounding granite [127].

Rock fracture exhibits inherent randomness, making statistical mechanics a promising and quickly growing approach for modeling fracture. Statistical techniques have been utilized for both rock engineering issues and geophysical inversion of shallow rock structures by different researchers as well as eathquake modeling and prediction. Rothman leveraged statistical mechanics concepts and Monte Carlo optimization to enable a globally-optimal nonlinear inversion approach for geophysical problems where traditional linearized techniques struggle. The key innovation was using statistical mechanics to reformulate the inversion in a way that enables global optimization through Monte Carlo methods [128]. Bashkirov et al proposed a new theoretical non-equilibrium statistical mechanics model using maximum entropy and the Tsallis distribution to explain the characteristic two-stage power law distribution and knee point seen in impact fragmentation experiments [129]. Daub et al reviewed the multiscale earthquake rupture problem, from the grain scale up to the fault scale. At smaller scales, they focused on the physics of deformation and plasticity in amorphous materials like fault gouge. At the fault scale, they discussed dynamic earthquake rupture propagation [130]. Kawamura et al reviewed reviews research on the statistical physics of fracture, friction, and earthquakes. It discussed fundamental physics of fracture and friction, including the Griffith theory of fracture, rate- and state-dependent friction laws, and microscopic models of friction and statistical physics models of earthquakes, including spring-block models like the Burridge-Knopoff (BK) model, continuum elastic models, and simplified coupled lattice models like the Olami-Feder-Christensen (OFC) model [131]. Xue et al utilized renormalization group (RG) theory and stress transfer mechanism to model the fracture process of rocks. They derived theoretical expressions for the axial strain ratio at peak stress to the axial strain at volumetric strain reversal as a function of the Weibull shape parameter for 1D, 2D and 3D RG models [132]. Wu et al developed a theoretical framework, calculation tools, and engineering applications for characterizing and analyzing the mechanical properties and behaviors of jointed rock masses using concepts from statistical physics and probability [133]. Wu et al developed an integrated set of technologies for intelligent and rapid in-situ data acquisition, interpretation, mechanical testing, theoretical calculation, and real-time quality evaluation of engineering rock masses. The innovations has enhanced the efficiency, accuracy, and intelligence of rock mass assessment [134].

Beyond rocks, subcritical crack growth has been explored by researchers in other materials such as ceramics and glass. Bermejo et al demonstrated that subcritical crack growth is a limiting factor affecting the strength and lifetime of low temperature co-fired ceramics components, especially in humid conditions. A modified crack velocity-stress intensity factor model provides insight into the changing mechanisms governing subcritical crack growth in dry environments [135]. Grutzik et al generated a unified kinetic model to anticipate subcritical crack growth behavior and thresholds in glass by linking fracture, diffusion, and viscoelastic relaxation processes. The prediction of fatigue thresholds is a notable achievement [136]. Mazerat et al revealed relationships between subcritical crack growth parameters and chemical composition in SiC fiber tows, highlighting the impact of composition on lifetime predictions [137].

Hizebry et al revealed relationships between composition, microstructure, poling, and crack growth mechanisms in lead zirconate titanate (PZT) ceramics. Domain switching is shown to be key in governing both R-curve and subcritical crack growth (SCG) behavior [138]. Kumar et al developed a multi-scale model considering crack growth from nano to micro to macro scales in concrete under fatigue loading. Also, they concluded that the notable aspects are the nano-scale foundation, multi-scale modeling approach, use of scaling laws, and capturing size and frequency effects on fatigue crack growth in concrete [139]. Krautgasser et al studied subcritical crack growth in low temperature co-fired ceramics with tailored compressive residual stresses in the surface layers. They showed that compressive residual stresses restricts subcritical crack growth in low temperature co-fired ceramics and introduces threshold behavior, substantially increasing reliability and lifetime [140]. Belli et al studied subcritical crack growth in the dental material Enamic using biaxial flexure tests.Their research provided multiple pieces of evidence that this dental composite does not exhibit an R-curve or crack bridging behavior as previously claimed. Similar static and cyclic crack growth parameters contradict the notion of bridging [141].

CHAPTER 3: STATISTICAL MECHANICS

3.1 Introduction

In this section a statistical thermodynamics developed by our group [3] is applied to model and interpret thermally-induced microfracturing in rocks. In fact, the statistical mechanics model accurately captures observed temperature-dependent acoustic emissions observed during thermal microfracturing experiments. Unlike other models, it does not require detailed knowledge of the mechanical loading history.

The introduced framework remains valid for natural field conditions where microcracks are randomly created and sealed at similar rates. Analysis of a fracture experiment from 2017 suggests the average microcrack population acts as an equilibrium thermodynamic variable that depends on temperature, volume, and pressure, regardless of process history. This enables predicting rock microfractures using equilibrium thermodynamics. In other words, microfracture population acts as a thermodynamic state variable, allowing estimates based solely on the current temperature, volume, and confining pressure of the rock. This dramatically simplifies prediction and interpretation. By combining the framework with atomic-scale modeling of grain boundary fracture, acoustic emissions analysis allows deducing single and multi-mode grain boundary microfractures.

3.2 Overview of predicting thermal microfractures in rocks using statistical thermodynamics

The application of Gibbs' statistical thermodynamics framework [142] to model subcritical fracture in rocks is a novel approach first put forward by our research group in [3]. We adapt the equilibrium framework to thermal microfracturing and demonstrate its utility combined with acoustic emissions data for interpreting and predicting the microfracture process.

We analyze data from an experimental study carried out in 2016 [5] in which small granite samples were cyclically heated and cooled between $\sim 23^o$ C to 65^o C, a temperature range relevant to terrestrial climates. The central assumption in our model is that for rock volumes subjected to random temperature fluctuations about a mean temperature T, over timescales τ_{eq}, under confining pressure P, and containing on the order of N grains, thermo-mechanical equilibrium exists, in which the average rate of microcrack creation balances the rate of healing. Based on this assumption, the microfracture population can then be treated as an equilibrium thermodynamic variable dependent on the current temperature, pressure, and volume. This dramatically simplifies the modeling.

By applying this adapted framework to thermal microfracturing and integrating it with AE measurements, we propose a new diagnostic tool for analyzing and forecasting subcritical fracture behavior in rocks under various thermal and pressure conditions.

3.2.1 Model Components

1) We consider an ensemble of $\tilde{N}$ identical rock volumes with temperature T, confining pressure P, and volume V. The grain structure is idealized as cubic mineral grains surrounded by an intergranular scaffold of atomically-thin, elastic grain boundaries that concentrate thermal stresses (Figs. 3.1 - 3.2).

2) Microcracks initiate and propagate along atomically thin grain boundaries, either between adjacent grains or at interfaces surrounding mineral inclusions.

Support for this assumption comes from extensive documentation of 1 nm-scale boundary widths with sharp property variations (mechanical, structural, chemical) across boundaries in minerals like olivine [143].

3) We model grain boundary microcracks as elliptical pancakes within the intergranular interface plane. This relies on the established relationship for the angle-dependent mode I stress intensity factor, $K_I(\theta)$, around a thin elliptic crack subject to out-of-plane tensile stress σ [144].

4) Stress fields surrounding a crack decay over distances proportional to $\sqrt{a}$, where a denotes the characteristic crack size. Since experiments show maximum grain boundary fracture dimensions approach the mean grain diameter d_g, we assume that detectable acoustic emissions are produced by cracks with axes between $0.1d_g$ and d_g.

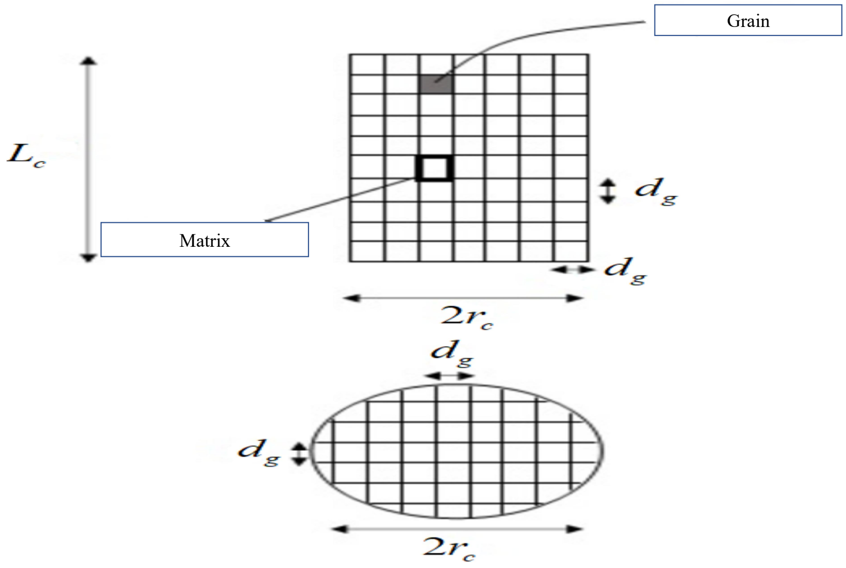

Figure 3.1: Idealized cubic grain geometry and intergranular fracture model used in simulations. Grain diameter $d_g \approx 1$ mm. The experiment uses a sample with height $L_c = 40mm$, radius $r_c = 10mm$. Thermal stresses focus on the atomically-thin grain boundary, making it the exclusive location of microfracture.

Table 3.1: Estimated parameters underlying statistical mechanics model. All temperatures, T, T_{min}, T_{bond}, are absolute; σ_T, rock bulk tensile strength; ν, bulk Poisson's ratio; d_g, average, equivalent grain diameter; $\Delta\alpha$, average difference in adjacent grain thermal expansion coefficients; E, bulk Young's modulus.

Parameter	Approximation	Approximate magnitude(granite)
Fracture strength	$K_c \sim \pi\sqrt{nd_g}\sigma_T$	n=30, $K_c \sim$ 1.7 MPa $\mathrm{m}^{-3/2}$
Grain boundary bond strength	$\epsilon_{gb} \sim \sigma_T d_o^3$	$\epsilon_{gb} \sim 10^{-3}\ \epsilon_{SiO_2}$; Appendix A
Grain bond fracture temperature	$T_{bond} \sim \epsilon_{gb}\tilde{\nu}\left(\Delta\alpha E d_o^3\right)^{-1}$	$T_{bond} \sim$ 5 K; Appendix A
Min. microfracture temperature	$T_{min} \sim \sigma_T\tilde{\nu}(\Delta\alpha E)^{-1}$	$T_{min} \sim$ 5 K; Appendix B
Min. temp.-dependent GB crack diameter	$\frac{d_{min}}{d_g} \sim \left[K_c\tilde{\nu}\left(\Delta\alpha\bar{E}\right)^{-1}\right]^2 T^{-2}$	$10^{-3} < \frac{d_{min}(T)}{d_g} < 10^{-2}$; Exps. 1-3 ; Appendix C
Min. AE-detectable microfracture area	$\sim 0.1 \cdot d_g^2 < A_{detect} <\sim d_g^2$	Appendix D

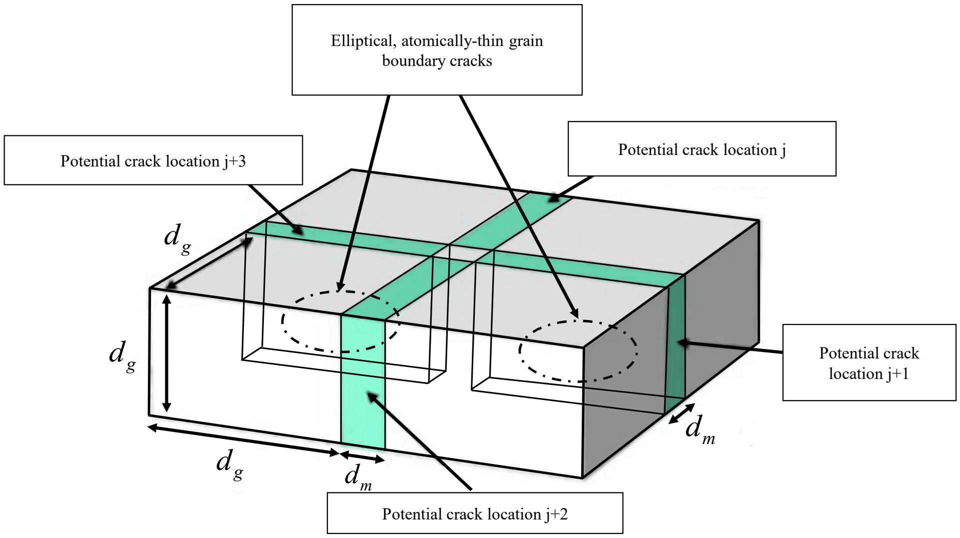

Figure 3.2: Zoomed in depiction of grain boundary fracture model

3.2.2 A Consistent Approach for Obtaining Linear Growth in Cumulative Acoustic Emissions

Arguments and analysis are presented by our group in [3] that lead to the following theoretical expression for the equilibrium, temperature-, pressure- and volume-dependent ensemble average, cumulative number of detectable microfractures, $\langle r^{(\alpha)}\left(\theta^{(\alpha)}, V, P\right)\rangle$, taking place in a rock volume V, under confining pressure, P, at absolute temperature, T :

$$\langle r^{(\alpha)}\left(\theta^{(\alpha)}, V, P\right)\rangle - 1 = \frac{e^{\eta_0^{(\alpha)}}}{\left(e^{\eta_0^{(\alpha)}} - 1\right)^2} - \frac{e^{\eta^{(\alpha)}}}{\left(e^{\eta^{(\alpha)}} - 1\right)^2} \tag{3.1}$$

The reader is directed to [3] for the statistical mechanical arguments leading to this expression.

Given the theoretical expression for $\langle r^{(\alpha)}\left(\theta^{(\alpha)}, V, P\right)\rangle$ in Eq. (3.1), and given the

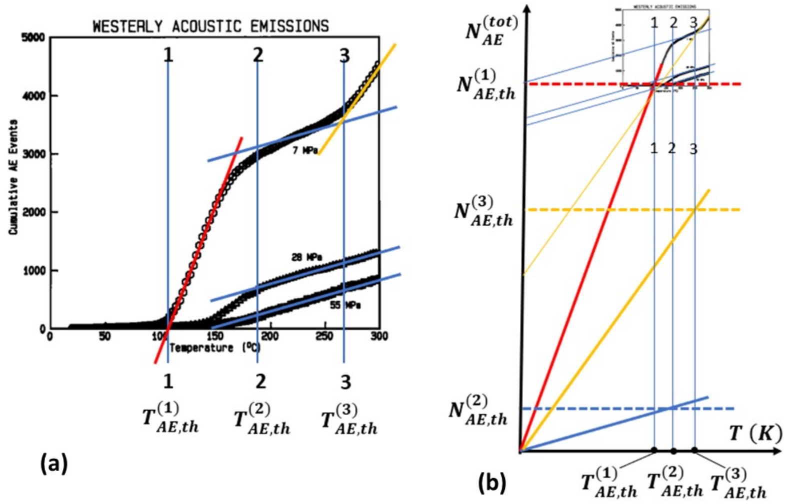

Figure 3.3: Scaling analyses and the microfracture model predict that grain boundary cracks start at near 0 K with atomically-thin, quasi-elliptical shapes, stop growing at grain diameter sizes, and accumulate linearly with temperature. The inset in (b) is shown at full scale in (a), with consistent slopes of cumulative AE lines for each mode α . This data was obtained by Wang et al [2]. The threshold area for acoustic detection is about the grain cross-section size. Acoustic emission histograms reveal up to three fracture modes at 7 MPa, two at 28 MPa, and one above 55 MPa, with each mode generating microcracks at a constant rate. Mode-specific threshold temperatures indicate when cracks approach detection limits. This analysis ties model predictions to acoustic emissions, validating temperature- and pressure-dependent fracture behavior during experimental thermal loading. Figure taken from [3].

apparent nominally linearly increasing acoustic emission observed during heating and cooling of small rock samples, see respectively Figs. 3.7 and 3.8 below, we arrive at an apparent theoretical inconsistency. In this section, we show that the proposed statistical mechanics model, leading to Eq. (3.1), does in fact predict the observed (linear) temperature-dependent growth of detectable acoustic emission.

In order to carry out the argument, it proves advantageous to consider the microfracture processes that occur during experiments in which high, linearly increasing temperatures are imposed on small rock samples [3]. As shown in Fig. 3.3, AE measurements indicate that at any given confining pressure, P, a sequence of distinct modes of microfracture, the set of which we'll denote generically as mode α microfracture (where $\alpha = 1, 2, 3..$) are sequentially activated and depleted as sample temperature, T, increases.

Two key observations indicate that initiation of mode α acoustic emission and associated depletion of mode $\alpha - 1$ acoustic emission - i.e., *transition* from mode $\alpha - 1$ to mode α microfracture - takes place over small temperature ranges, $\delta T^{(\alpha)}$. First, changes in the acoustic emission rate, illustrated in Fig. 3.3, emerge over small temperature intervals, as shown by variations in cumulative emission. Second, Gaussian fits of the temperature-dependent acoustic emission detailed in [3] indicate that mode α acoustic emission peaks at, and persists near $T_0^{(\alpha)}$, the nominal $\alpha - 1$ to α transition temperature (nominally) determined by plots of cumulative acoustic emission; see Fig. 3.3.

To model these characteristics, we assume that observable mode α microfracturing commences over a confined temperature range, starting at $T_o^{(\alpha)}$, as follows:

$$T_o^{(\alpha)} \leq T_{initiation}^{(\alpha)} \leq T_o^{(\alpha)} + \delta T^{(\alpha)} \tag{3.2}$$

where $\delta T^{(\alpha)} << T_0^{(\alpha)}$.

Significantly, this assumption results in consistent predictions of both the nominally linearly increasing acoustic emission observed during the experiment described in section 3.3.1 below, as well as those observed in two other experiments presented in [3]. First, define $f^{(\alpha)}(T)$ from Eq. (3.1) as:

$$f^{(\alpha)}(T) = \frac{e^{\eta^{(\alpha)}}}{\left(e^{\eta^{(\alpha)}} - 1\right)^2} \tag{3.3}$$

and then express $f^{(\alpha)}(T)$ as:

$$f^{(\alpha)}(T) = f^{(\alpha)}\left[T_0^{(\alpha)}\left(1+\epsilon^{(\alpha)}\right)\right] \tag{3.4}$$

where $\epsilon^{(\alpha)}$ is defined as:

$$\epsilon^{(\alpha)} = \frac{\left(T - T_0^{(\alpha)}\right)}{T_0^{(\alpha)}} \tag{3.5}$$

A two-term Taylor expansion in ϵ then gives us the following equation:

$$f^{(\alpha)}(T) = f^{(\alpha)}\left(T_0^{(\alpha)}\right) + \left(\frac{df}{dT}\right)_{T_0} \cdot \left(T - T_0^{(\alpha)}\right) + O\left(\epsilon^{(\alpha)2}\right) \tag{3.6}$$

In which the maximum value of $\epsilon^{(\alpha)2}$ is approximately 0.1 for the experiments examined here and in [3]. Evaluating the derivative at $T_o^{(\alpha)} + \delta T^{(\alpha)}$ to avoid a non-zero derivative, we then obtain:

$$f^{(\alpha)}(T) = f^{(\alpha)}\left(T_0^{(\alpha)}\right) - \left(\frac{2k_B'}{E_{co}^{(\alpha)}\delta T^{(\alpha)2}}\right) \cdot \left(T - T_o^{(\alpha)}\right) + O\left(\epsilon^{(\alpha)2}\right) \tag{3.7}$$

Finally, substituting Eq. (3.6) into (3.1) gives us a theoretical formula for the cumulative number of detectable mode α microfractures as follows:

$$\left\langle r^{(\alpha)}(T,V,P)\right\rangle = \left(\frac{2k_B'}{E_{co}^{(\alpha)}\delta T^{(\alpha)2}}\right) \cdot \left(T - T_o^{(\alpha)}\right) + 1, \quad T_0^{(\alpha)} \le T < T_0^{(\alpha+1)} \tag{3.8}$$

or

$$\left\langle r^{(\alpha)}(T,V,P)\right\rangle = R_T^{(\alpha)}\left(T - T_0^{(\alpha)}\right) + 1, \quad T_0^{(\alpha)} \le T < T_0^{(\alpha+1)} \tag{3.9}$$

where, we denote the coefficient multiplying the mode α relative temperature, $\left(T - T_0^{(\alpha)}\right)$, as $R_T^{(\alpha)}$. Hence, we have:

$$R_T^{(\alpha)} = \left(\frac{2k_B'}{E_{co}^{(\alpha)}\delta T^{(\alpha)2}}\right) \tag{3.10}$$

Physically, $R_T^{(\alpha)}$ can be viewed as a linear response function that quantifies the average number of detectable, grain-scale mode α grain boundary cracks produced per unit temperature increment. Importantly, Eq. (3.8) and its derivation from Eq. (3.3), provides a theoretical framework for interpreting experimental cumulative acoustic emissions, $\langle r^{(\alpha)}(T, V, P)\rangle$.

3.3 Experiment: Statistical Thermodynamic Evaluation of Terrestrial-scale Periodic Heating and Cooling of Rock

Fracturing due to periodic heating and cooling of surface rocks on earth plays a crucial role in various geological processes, such as landscape and sediment formation [145], water movement in surface and shallow subsurface environments [146], rates of desertification in arid climates [147], long-term shifts in flora and climate [148], and absorption and discharge of atmospheric gases from the surface. Advancing quantitative, predictive understanding of these critical surface processes depends substantially on developing predictive models of fracturing in surface and shallow subsurface rocks [149],[150].

This Experiment probes thermal microfracture taking place during a sequence of five cycles of heating and cooling, imposing temperatures on the same scale as those extant on Earth's surface: 23^oC to 65^oC, a temperature span for which surprisingly few such measurements exist [5]. The experimental setup is illustrated in Fig. 3.4. Cylindrical granite samples, measuring 20 mm in diameter and 40 mm in length were extracted as cores near the center of a half-boulder. Acoustic emissions (AE) were then monitored during five heating and cooling cycles in which the maximum sample temperature reached approximately 65^o C. A fixed radiant heat flux, q_{rad}, was set to achieve an initial $1^oC/\text{min}$ rate of sample temperature rise during each heating interval. Due to increasing convective heat loss from the sample, q_{conv}, the initial sample heating rate tapers off, approaching an asymptotic value, $T_{asymp} \approx 65^{o}$C (reflecting $q_{conv} \rightarrow q_{rad}$). See Fig. 3.5 and Section 3.8. Each heating period was 3 hours; subsequently, the heater was turned off and the sample allowed to convectively cool for at least 30 hours. Sample temperatures, $T\left(t\right) \approx T_{surf}\left(t\right),$ were recorded using a single thermocouple attached to the mid height of the sample, with individual measurements triggered by detected acoustic emissions from the sample. Acoustic emissions were detected using an acoustic sensor attached to the top of an upper piston, with the sample held in place between a matched pair of sensors.

Applying the analysis resulting in Eq. (3.9) to the periodic heating and cooling intervals imposed during the Experiment gives a theoretical formula for the cumulative number of observable intergranular microcracks generated as a function of sample temperature:

$$\langle r^{(1)}\left(T,V,P\right)\rangle = R_{T}^{(1)}\left(\pm T \mp T_{0}^{(1)}\right) + 1, \quad T \geq T_{0}^{(1)} \tag{3.11}$$

Where the upper signs refer to heating periods and the lower signs to cooling periods. Since only small temperature variations are used, we assume activation of just a single mode of intergranular microfracturing.

3.3.1 Experimental Findings and Analysis

Recorded random-in-time temperature readings, along with theoretically predicted sample temperature histories, are presented for all five heating and cooling intervals in Figs. 3.5 and 3.6.

High temperature heating experiments presented in [3] show that for applied tem-

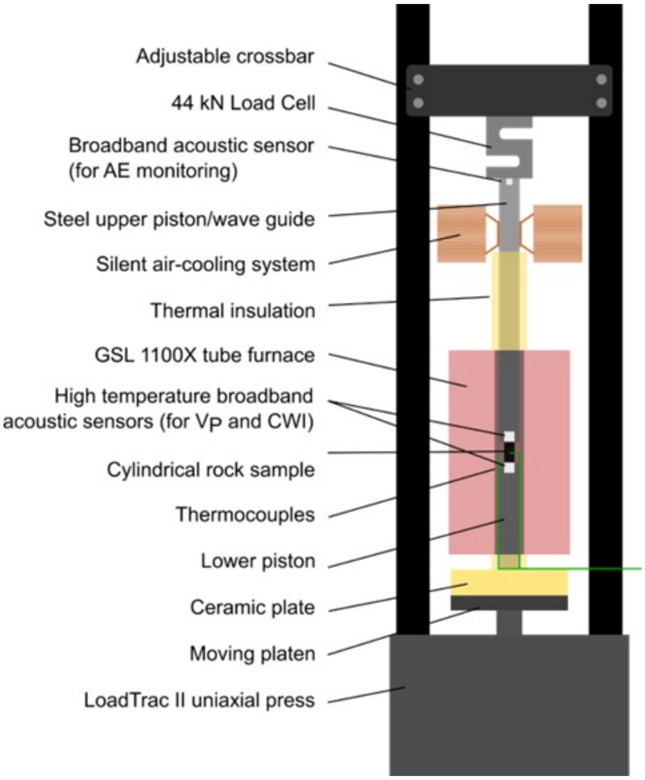

Figure 3.4: Experimental Apparatus [4]

perature changes, ΔT_{exp}, under roughly 100 K, microfracturing is limited to mode 1. Figs. 3.7 and 3.8 demonstrate that over the narrow range of temperatures used in the present experiment, cumulative acoustic emissions during individual heating and cooling periods, respectively, exhibit an approximately linear increase and decrease with temperature, consistent with Eq. (3.11). Quantile plots are used to show that experimental data is appropriately being modeled by the proposed theoretical formula. Specifically, quantile plots shown in Figs. 3.9 and 3.10 indicate that Eq. (3.11) provides reasonable predictions of the observed cumulative AE, especially for heating and cooling cycles after the first cycle.

Each heating and cooling interval fit takes $T_0^{(1)}$ as the sample temperature when the first acoustic emission is detected and determines the response coefficient $R_T^{(1)}$ as a single parameter. This assumption aligns with the premise that observable mode α

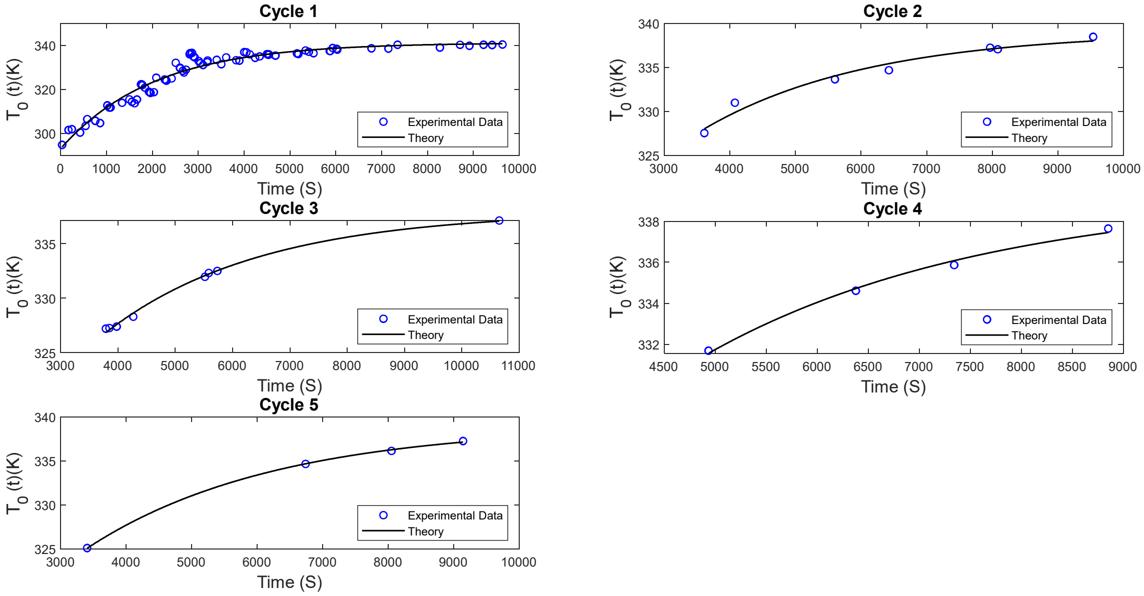

Figure 3.5: Simulated and measured rock temperatures for each of five cyclical heating runs in Experiment 1. Observed correlation coefficients over the repeated intervals are $R_1 = 0.96$, $R_2 = 0.97$, $R_3 = 0.99$, $R_4 = 0.99$, and $R_5 = 0.99$, respectively, indicating quantitative agreement between the thermal model and data across different cycles (Experimental data were collected by Luke Griffiths [5]).

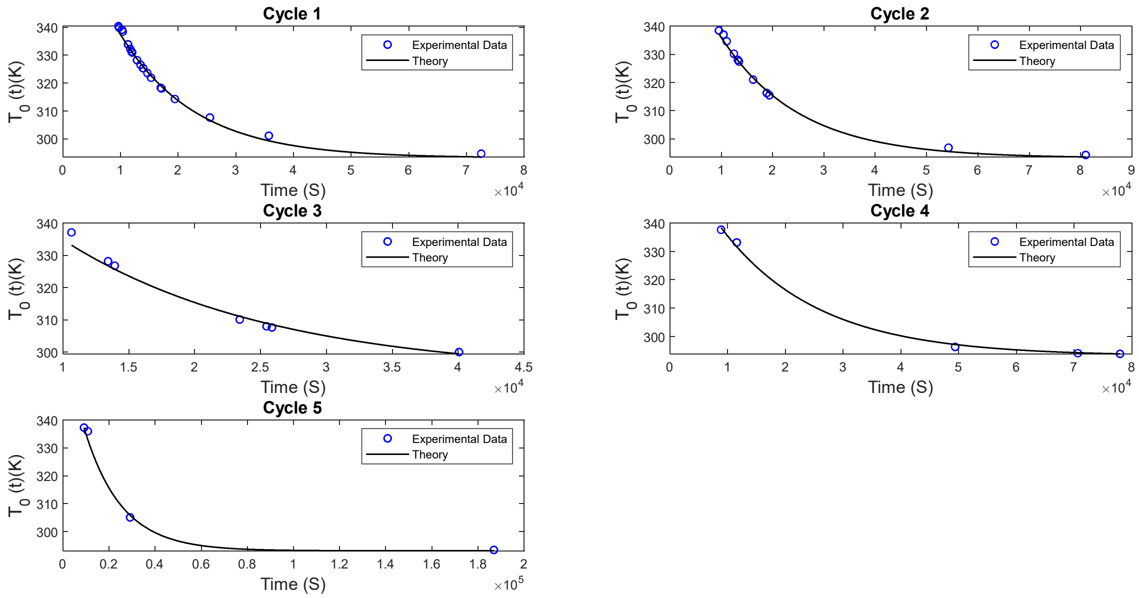

Figure 3.6: Simulated and measured rock temperatures for each of five cyclical heating runs in Experiment 1. Observed correlation coefficients over the repeated intervals are $R_1 = 0.99$, $R_2 = 0.99$, $R_3 = 0.98$, $R_4 = 0.99$, and $R_5 = 0.99$, respectively, indicating quantitative agreement between the thermal model and data across different cycles (Experimental data were collected by Luke Griffiths [5]).

microfracturing takes place over a narrow temperature range, $\delta T^{(\alpha)}$. Examination of Fig. 3.7 shows that $\delta^{(1)}/T^{(1)}_{0,min} \approx 0.1$, where $T^{(1)}_{0,min} = 295$ K. Similarly, analysis of the data in Fig. 3.8 demonstrates that $T^{(1)}_0$ stays nearly fixed at ~ 338 K, while the corresponding range of measured mode 1 transition temperatures is small, i.e., $\delta T^{(1)} \approx 1$ K.

The observed decreases in the estimated response coefficient, $R^{(1)}_T$, over successive heating and cooling cycles (Figs. 3.7 and 3.8) are interpreted as reflecting growth in the length of the mode transition interval, $\delta T^{(1)}$. Physically, the increase in $\delta T^{(1)}$ likely indicates depletion of mode 1 fracture sites with continued cycles of heating and cooling.

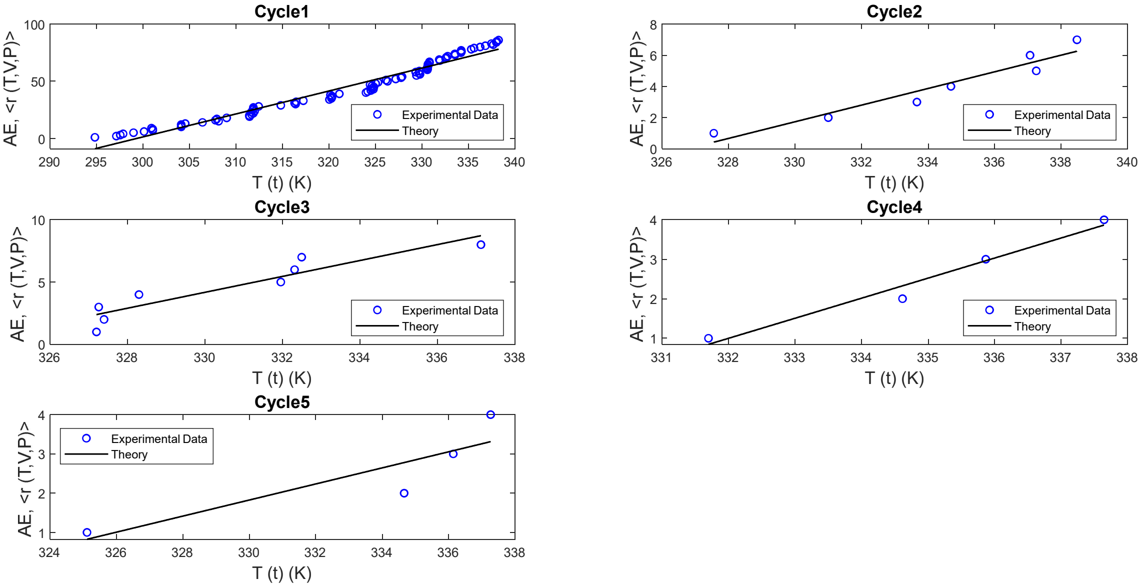

Figure 3.7: Theoretical versus observed rock sample acoustic emission histories during each of five repeated heating intervals. The correlation coefficient during each of five repeated heating intervals are $R_1 = 0.96$, $R_2 = 0.92$, $R_3 = 0.86$, $R_4 = 0.96$, $R_5 = 0.78$, respectively (Experimental data were collected by Luke Griffiths [5]).

In contrast to experiments reported in [3], where acoustic emissions were not detected at imposed temperatures below approximately 340 K, detectable AE here appears over the entire range of relatively low imposed temperatures: $\sim 295\,K \leq T \leq\sim 338\,K$. See Fig. 3.7. Thin section micrographs taken from the same boulder from which the experimental sample was extracted showed a relatively high density of preexisting microcracks (result not shown). This observation combined with our observation of low-temperature AE suggests that preexisting crack populations are prone to thermally induced microfracture at lower temperatures than those producing microfracture in the 'fresh', relatively unfractured samples used in [3].

As a final important point, we note that sound speed measurements (not shown) indicated that sound speed *increased* after the first cycle of heating and cooling, sug-

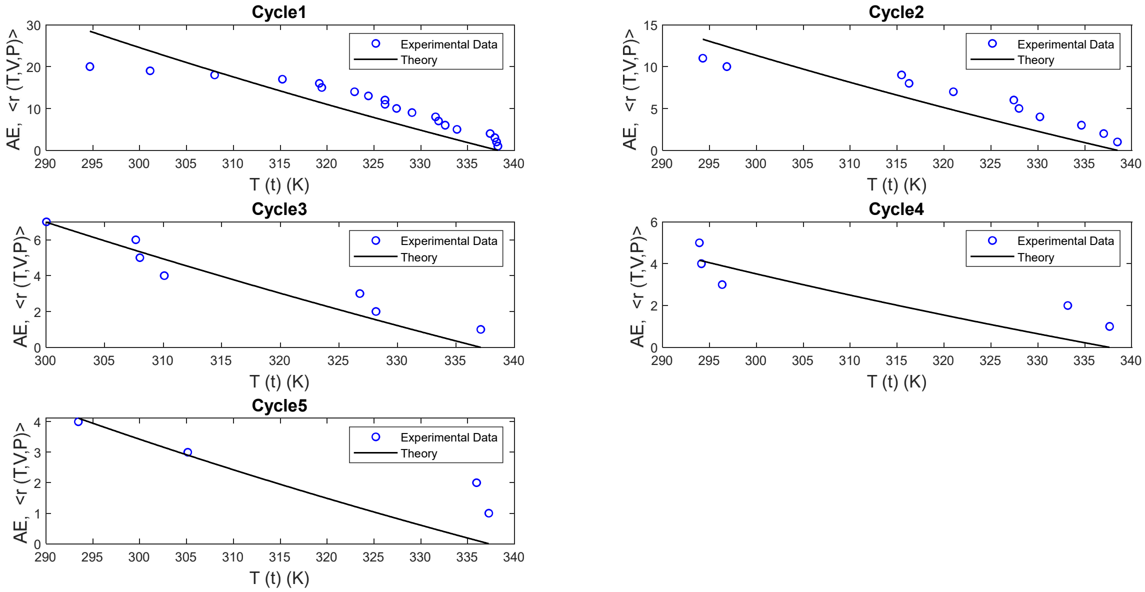

Figure 3.8: Theoretical versus observed rock sample acoustic emission histories during each of five repeated cooling intervals. The correlation coefficient during each of five repeated cooling intervals are $R_1 = 0.87$, $R_2 = 0.84$, $R_3 = 0.86$, $R_4 = 0.73$, $R_5 = 0.71$, respectively (Experimental data were collected by Luke Griffiths [5]).

gesting that the initial heating and cooling cycle sealed more cracks than it opened. Hence, this experiment gives us observable, short-term (hour time scale) evidence supporting a key tenet underlying the equilibrium fracture model: Over adequate timescales, the rate of intergranular fracturing matches the rate of closure.

3.3.2 Independence of Thermal Path in Equilibrium Microcrack Distributions

The concept of path independence is crucial for equilibrium thermodynamic variables, as it enables geologists and materials scientists to estimate cumulative microfracture populations, i.e., $\langle r\,(T, V, P)\rangle$, using only the current temperature, volume, and confining pressure of the rock. There are two pieces of evidence supporting our hypothesis that $\langle r\,(T, V, P)\rangle$ can be treated as an equilibrium thermodynamic

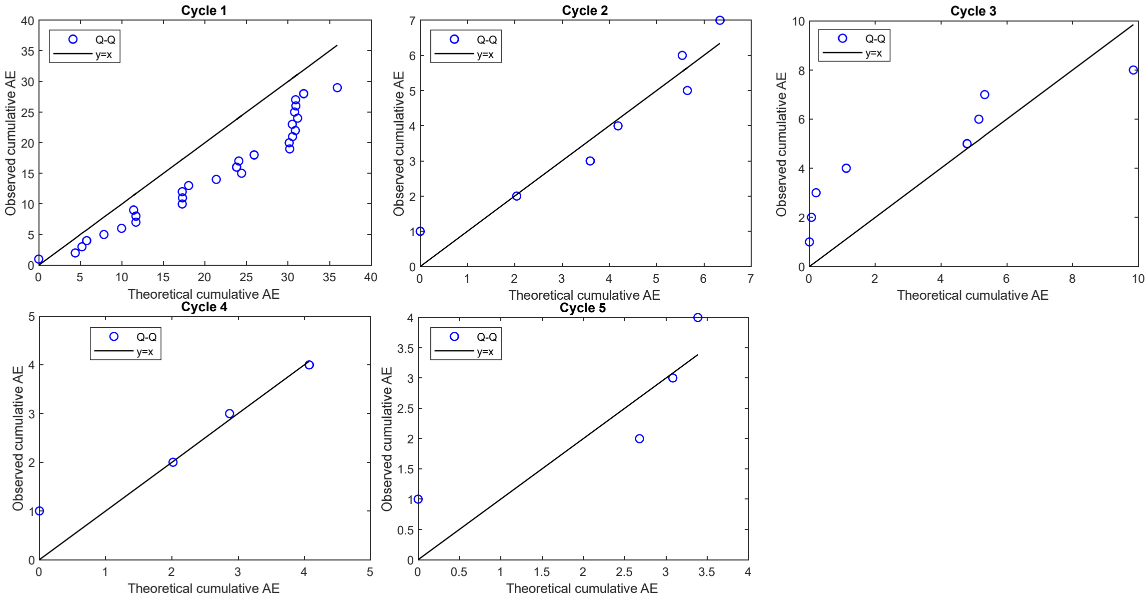

Figure 3.9: Q-Q plots comparing theoretical and observed rock sample acoustic emission histories during each of five repeated heating intervals. The correlation coefficient during each of five repeated heating intervals are $R_1 = 0.85$, $R_2 = 0.92$, $R_3 = 0.76$, $R_4 = 0.91$, $R_5 = 0.89$, respectively (Experimental data were collected by Luke Griffiths [5]).

variable:

1) In three separate experiments - the experiment reported here and two reported by our group in [3] - and as predicted by our model, Eq. (3.11), we observe (nominally) linearly increasing acoustic emission with (increasing) temperature, over temperatures ranging from approximately 300 K up to approximately 720 K.

2) As reported in [3], normalized histograms of measured temperature- and pressure-dependent acoustic emission are well-fit by theoretical Gaussian probability densities derived from our model. The model assumes an equilibrium canonical ensemble of $\tilde{N} >> 1$, microfracturing (and healing) replica rock samples, which in turn leads to a theoretical (temperature- and pressure-dependent) Gaussian distribution in mi-

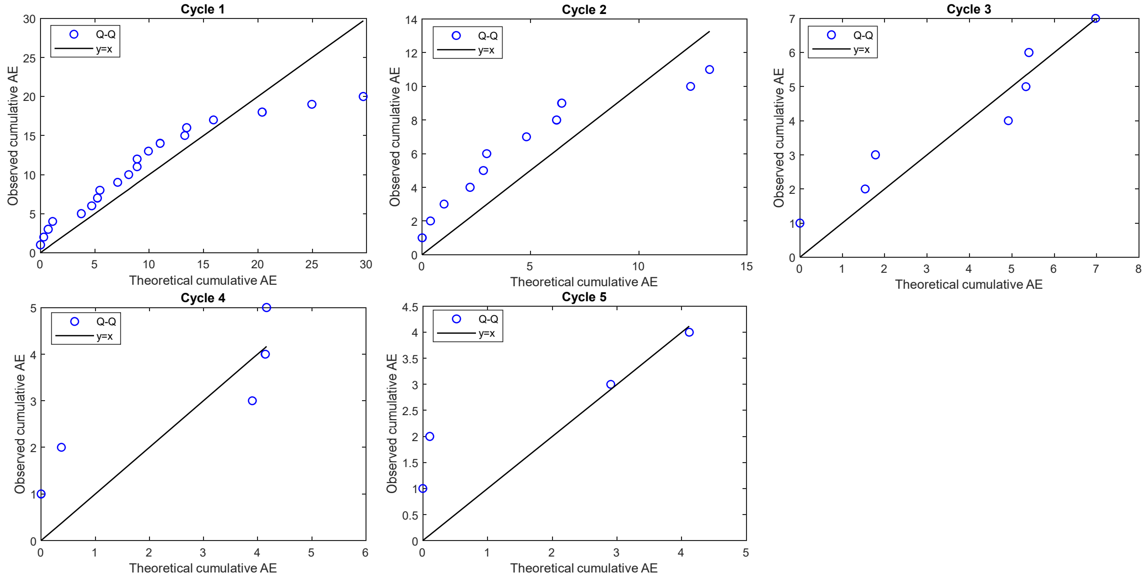

Figure 3.10: Q-Q plots comparing theoretical and observed rock sample acoustic emission histories during each of five repeated cooling intervals. The correlation coefficient during each of five repeated cooling intervals are $R_1 = 0.87$, $R_2 = 0.76$, $R_3 = 0.82$, $R_4 = 0.65$, $R_5 = 0.83$, respectively (Experimental data were collected by Luke Griffiths [5]).

crofracture number. Of relevance here, by Gibbs' construction of equilibrium statistical thermodynamics, existence of such a distribution is consistent with, and indeed demands path independence.

3.3.3 An Experimental Model for Investigating Weathering via Daily Heating and Cooling Cycles

Four key observations indicate that the present experiment can serve as an effective laboratory analog for investigating the weathering of surface rocks through daily heating and cooling cycles. First, the cyclic thermal stresses applied in this experiment are comparable to those induced by diurnal surface heating, around $\sigma \sim 10$ MPa.

Second, as shown in Fig. 3.11 and discussed in Section 3.5, measured cumulative acoustic emission here exhibits an exponential decay with cycle number, a short (hour) time-scale result that mimics the exponential drop in fracture intensity, taking place over 1000 to 70,000 year timescales, recently observed by our group in a long-term study carried out at three climatically distinct field sites.

Third, our measurements reveal that subsequent to the initial heating and cooling cycle, a Kaiser-effect-like suppression of thermal fracturing takes place. Although the Kaiser effect appears only when succeeding cycles of heating produce sequences of increasing maximum thermal stress, referring to Fig. 3.12 and Section 3.5, microfracture initiation following cycle 1 emerges only when the imposed thermal stress approaches the maximum applied. Kaiser-effect suppression of fracture undoubtedly occurs under natural, in-situ conditions. Experiments like this one suggest that under natural conditions, once a crack population is established, for example, by an extreme environmental stress event, continued fracture creation, as well as growth of existing cracks, likely remains (nominally) deactivated. Crack activation subsequently occurs only when either a new, higher stress is imposed or after a long, low stress period of fracture healing sets in.

Last, evidence presented in Section 3.6 suggests that simultaneous fracturing and crack healing takes place during heating and cooling, under moderate confining pressures. As discussed in Appendix E, the statistical mechanics model implicitly incorporates the energetics of thermoelastic crack closure by decomposing the rock specimen into two subsystems: the set of atomically-thin solid shells bounding all microcracks, and the remaining intact rock. As shown in Appendix E, acoustic and thermal data from this experiment indicate that during the initial heating interval, thermal expansion simultaneously unseals new microcracks while sealing preexisting cracks, with many of the latter remaining closed over subsequent heating and cooling cycles. Again, we expect that similar physical features underlie in situ diurnal heating and cooling of terrestrial surface rock.

3.4 Heat Transfer Modeling: Heating and Cooling Models

As mentioned before, the rate of heat transfer to each sample is sufficiently small that, following a short initial transient heating period on the order of 1 to 5 minutes, spatial temperature gradients within each sample become negligible. the characteristic time required for the thermal boundary layer to grow through the entire sample is denoted as τ_T which is approximately 60 seconds, after which the temperature distribution within the sample can be considered uniform. The calculation of τ_T is based on the sample radius R_s ($R_s = 2 \times 10^{-2}$ m) and the thermal diffusivity α_T ($\alpha_T \approx 1.6 \times 10^{-6}\ m^2 s^{-1}$) of the material, which governs the rate of heat transfer through the sample and can be written as $\tau_T = R_s^2/\alpha_T$.

Given that the experimentally imposed heat flux, q_{in}, is small and results in a sample temperature increase of only 1 K/min, a spatially lumped model of sample heat transfer is suitable. This approach is then validated by the results presented in Figs. 3.5 and 3.6, and can be used as follows:

$$\rho V c_p \frac{dT}{dt} = -A_0 h \left[T\left(t\right) - T_\infty\right] + q_{in} A_0; \qquad 0 \le t \le t_{heat} \tag{3.12}$$

where h, ρ, V, c_p, T_∞, q_{in}, A_0, $T\left(t\right)$, and t_{heat} are the convective heat transfer coefficient, rock density, rock volume, rock specific heat, the fixed test chamber temperature, the fixed imposed radiant heat flux, rock lateral area, the instantaneous temperature of the rock sample, and the length of the heating interval, respectively.

Assuming that all of the parameters in the lumped heat transfer model equation are fixed, and also by assuming $\theta(t)$ and t as $\theta(t) = T_0(t) - T_\infty$ and $0 \leq t \leq t_{heat}$, respectively, Eq. (3.12) can be written as follows:

$$\rho V C_P \frac{d\theta(t)}{dt} = -A_0 h \theta(t) + q_{in} A_0 \rightarrow \frac{d\theta(t)}{dt} + \frac{A_0 h}{\rho V C_P}\theta(t) = \frac{q_{in} A_0}{\rho V C_P} \tag{3.13}$$

Now, by assuming K_1 and K_2 as $K_1 = f(t) = \frac{A_0 h}{\rho_0 V_0 C_{P_0}}$ and $K_2 = q(t) = \frac{q_{in} A_0}{\rho_0 V_0 C_{P_0}}$, respectively, we can get $\theta(t)$ as follows:

$$\theta(t) = \frac{K_2}{K_1}(1 - e^{-K_1 t}) \rightarrow \theta(t) = \frac{q_{in}}{h}(1 - e^{-\frac{A_0 h}{\rho V C_P}t}) \tag{3.14}$$

Finally, time dependent temperature, $T(t)$, during heating interval can be written as follows:

$$T(t) = \frac{q_{in}}{h}\left(1 - e^{-\frac{A_0 h}{\rho V c_p}t}\right) + T_\infty \tag{3.15}$$

Heat transfer during cooling intervals is governed by a similar equation as follows:

$$\rho V c_p \frac{dT}{dt} = -A_0 h \left[T\left(t\right) - T_\infty\right]; \qquad t_{heat} \leq t \leq t_{cycle} \tag{3.16}$$

As you see, in the above equation time interval is between t_{heat} and t_{cycle}. Defining $\theta(t)$ as $T_0(t) - T_\infty$ and substituting that in Eq. (3.16) results in the following equation for $\theta(t)$:

$$\theta(t) = (T_0(t_{heat}) - T_\infty) e^{\frac{A_0 h}{\rho V C_P} t_{heat}} e^{\frac{-A_0 h}{\rho V C_P} t} \tag{3.17}$$

By simplifying the above equation, we can get a very useful formula that gives us time dependent heat transfer during cooling interval as follows:

$$T(t) = \left[T\left(t_{heat}\right) - T_{\infty}\right] e^{\frac{A_0 h}{\rho V c_p}\left(t_{heat}-t\right)} + T_{\infty} \tag{3.18}$$

3.5 Exponential Decay in Fracture Intensity and Kaiser-like Effects in Rock Weathering

The cyclic thermal stresses imposed during the experiment were of similar magnitudes, i.e., $\sigma \sim 10$ MPa as those produced by diurnal surface heating. Interestingly, the observed cumulative acoustic emission (AE) exhibited an exponential decay with increasing cycle number, as shown in Fig. 3.11. Recently, the research group observed similar exponential decays in fracture intensity during a large-scale study conducted at multi-continent, climatically-distinct field sites. In that field study, the exponential decay was observed over timescales ranging from approximately 100 to 70,000 years [151]. Thus, the experiment suggests that lab-based analog experiments can expose at least some of the physical mechanisms underlying the apparently universal exponential decay observed in the fracturing and weathering of surface rocks.

In this experiment, we identified a Kaiser-like effect where incipient grain boundary fracture sites were significantly exhausted during the first heating and cooling cycle. Previous work focused on seismological stress scales which is $\sigma \sim 2 \times 10^2$ MPa and has shown that acoustic emission does exhibit a Kaiser effect [152]. In these studies, detectable AE during load cycle $n+1$ is not observed until the imposed stress, σ_{n+1}, approximately exceeds the maximum stress, $\sigma_{n,max}$, from the previous cycle, n at least at stresses below the dilatancy limit where rock volume increases due to fracture. Although our measurements during cyclic heating and cooling indicate that Kaiser effect is not strictly operative at low, diurnal thermal stress magnitudes, the detected fractures, following cycle 1, first appeared at thermal stresses near the maximum imposed. See Fig. 3.12.

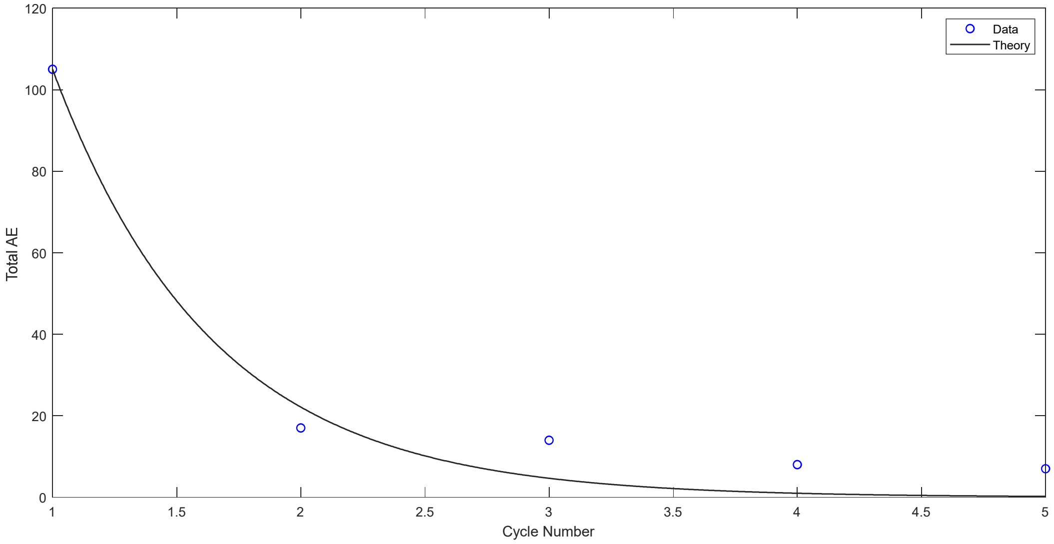

Figure 3.11: Total acoustic emission observed in granite during five successive diurnal-scale heating and cooling cycles. The correlation coefficient for the fit is $R = 0.97$ (Experimental data were collected by Luke Griffiths [5]).

3.6 Evidence of Thermoelastic Fracture and Crack Closure Dynamics under Moderate Confining Pressures during the Experiment

Heating and cooling of rock simultaneously induces fracture formation and crack closure processes under moderate confining pressures. The statistical mechanics model accounts for the energies of thermoelastic crack closure by decomposing the rock sample into two subsystems including being the set of atomically-thin solid shells encompassing all microcracks, and also being the remaining solid rock matrix.

Acoustic and thermal measurements obtained during the experiment indicate that during the first heating interval, thermal expansion both opens new microcracks and closes existing microcracks, with a significant fraction of the latter remaining permanently closed during subsequent heating and cooling cycles.

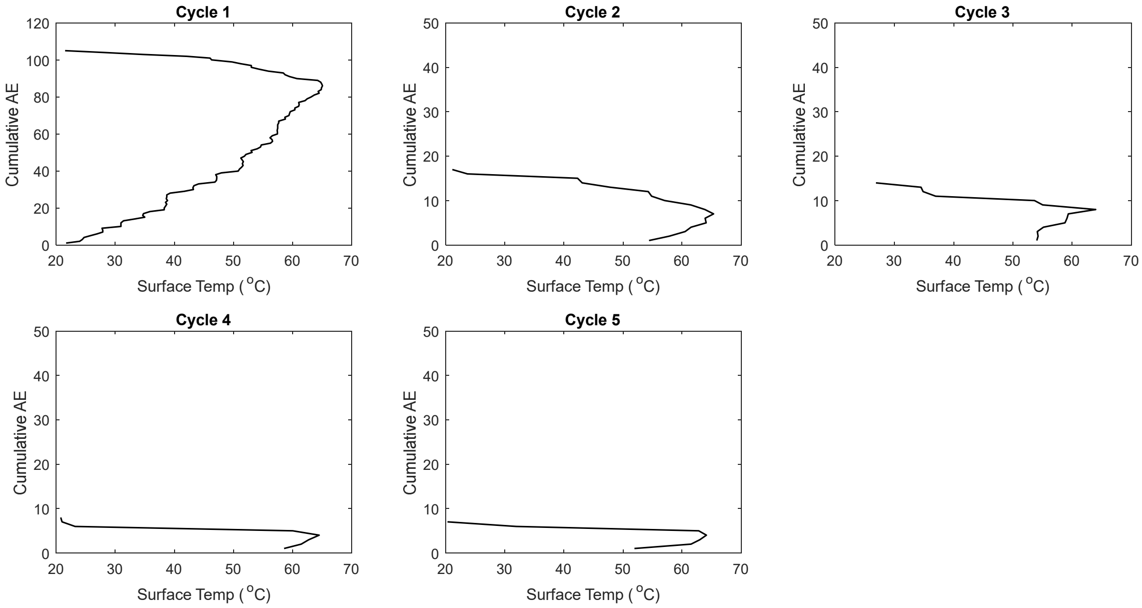

Figure 3.12: Kaiser effect observed in rock sample acoustic emission histories during each of five repeated heating and cooling cycles (Data were collected by Luke Griffiths [5])

After the first heating and cooling cycle, the p-wave velocity, v_p, increases and maintains a nominally fixed magnitude during cycles 2 through 4, where measurements were not taken during the fifth cycle (results not shown). Similarly, the sample's specific heat, c_p, also increases after the first cycle. This is evident from the comparison of observed and predicted sample temperature histories shown in Fig. 3.13. According to the rock sample heat transfer model in section 3.9, during the heating intervals, the observed gap in sample temperature at any time, t, can be described by:

$$\frac{T_1(t) - T_k(t)}{q/h} = \exp\left[\frac{A_o h t}{m c_{p,1}}\right] - \exp\left[\frac{A_o h t}{m c_{p,k}}\right] \tag{3.19}$$

where $T_1(t)$ and $T_k(t)$ are instantaneous sample temperatures during heating intervals 1 and k $(k = 2, 3, 4)$, respectively, A_o is the lateral (heated) sample surface area, m is the sample mass, and $c_{p.1}$ and $c_{p,k}$ are corresponding (bulk) sample specific heats. Experimental fits for the parameters q and h show that these remain nominally fixed during all five heating intervals. Likewise, since the ratio of detected atomically-thin microcracks (from acoustic emissions) to the approximate number of grains in the sample is on the order of 1 to 300, the sample area, A_o, remains nominally fixed. Thus, Eq. 3.19 and Fig. 3.13 demonstrate that the specific heat increases and remains nominally fixed over the second through fourth thermal cycles.

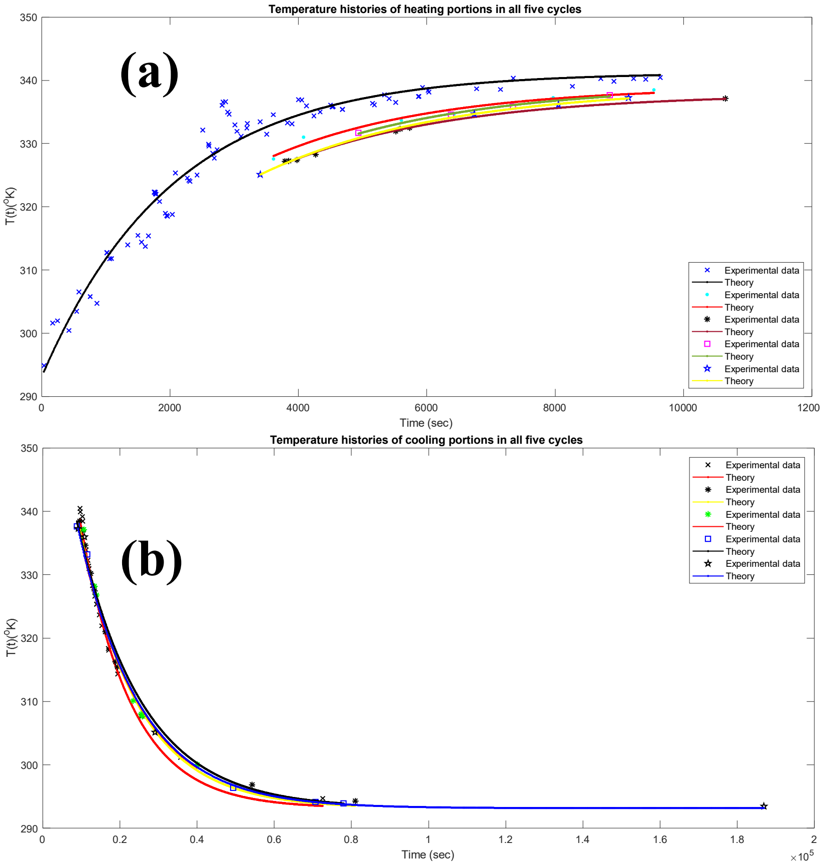

Figure 3.13: Experimental and theoretical variations in sample temperatures over five heating and cooling cycles. (a) The nearly constant decrease in temperature rise, at any time t, indicates thermal closure of microcracks and an associated increase in heat capacity, as described by Eq. (3.19). (b) Predicted temperature histories, depicted as solid curves, are presented individually in Figs. 3.5 and 3.6 (Experimental data were collected by Luke Griffiths [5]).

CHAPTER 4: DIMENSIONAL ANALYSIS AS A TOOL FOR EXPOSING SLOW AND FAST SUBCRITICAL FRACTURE MODES IN ROCK

4.1 Introduction

This chapter applies dimensional analysis to recast existing dimensional experimental correlations relating crack growth rate in rock to stress intensity, a process that has not been applied to this broad area of experimental research, and also exposes, for the first time, two distinct modes of subcritical fracture in rock. In this chapter, we cover the following items:

a) First briefly reviewing the process of dimensional analysis, highlighting an example from fluid dynamics; see Section 4.2

b) Describing a series of double torsion stress relaxation experiments, reported by Nara et al. [7] and some other researchers with more details, in which dimensional subcritical fracture velocities were measured in granite, under various environmental conditions, as a function of dimensional stress intensity; see Section 4.3

c) Proposing and discussing a list of guessed dimensional variables that we believe are essential for exposing high quality, dimensionless rock fracture rate correlations; see section 4.5.
d) Presenting the data from Nara's experiments in both dimensional and dimensionless forms; see Section 4.6.

e) Presenting a preliminary analysis of the apparent slow and fast subcritical crack growth that occurs during double torsion stress relaxation tests; see Section 4.7.

4.2 Dimensional Analysis Overview (An Example of Dimensional Analysis Using Buckingham Pi Theorem)

In this part, the application of dimensional analysis using Buckingham pi theorem in order to derive wing drag coefficients in terms of Reynolds number is shown. For this purpose, we should first try to identify the relevant variables. In this case, the relevant variables can be listed as follows:

Drag force (D), Air density (ρ), Wing area (S), Air velocity (V), Air viscosity (μ) and wing chord length (c). Next, we should select the primary dimensions as mass (M), length (L), and time (T). Then, we express each variable in terms of the primary dimensions as follows:

Drag force (D): MLT^{-2} ; Air density (ρ): ML^{-3} ; Wing area (S): L^2 ; Air velocity (V): LT^{-1} ; Air viscosity (μ): $ML^{-1}T^{-1}$; Wing chord length (c): L

After that, we try to find the number of dimensionless groups, i.e., π terms using the Buckingham Pi theorem as follows:

Number of π terms = Number of variables - Number of primary dimensions

Number of π terms = 6 - 3 = 3

Then, we form the π terms by combining the variables in such a way that each term is dimensionless. Let's choose ρ, V, and c as the repeating variables. Therefore, the dimensionless π groups can be written as follows:

$\pi 1 = D \;/\; \rho V^2 c^2$ (Dimensionless)

$\pi 2 = \mu \;/\; (\rho V c)$ (Dimensionless)

$\pi 3 = S \;/\; c^2$ (Dimensionless)

Then, we express the functional relationship between the π terms, i.e., $\pi 1$ = f($\pi 2$, $\pi 3$).

In the next step, we identify the physical meaning of each π term as follows:

$\pi 1 = D \ / \ \rho V^2 c^2$ is the drag coefficient, denoted as C_D.

$\pi 2 = \mu \ / \ (\rho V c)$ is the Reynolds number, denoted as Re

$\pi 3 = S \ / \ c^2$ is the aspect ratio, denoted as AR.

Finally, having used the Pi theorem to boil out the dimensionless variables associated with our guessed list of essential dimensional variables, we can now express the generic, *dimensionless*, a prior unknown relationship between dimensionless drag, i.e., the drag coefficient, C_D, and the remaining dimensionless variables ('pi terms') as the all-important experimental design equation:

$$C_D = f\,(Re, AR) \tag{4.1}$$

Three important points follow from Eq. (4.1). First, assuming that we have chosen all of the essential dimensional variables and parameters that describe the complicated relationship between dimensional drag force, air speed, fluid properties, and the shape of the aerodynamic body, then Eq. (4.1) states that a series of experiments in which Re and AR are systematically varied will result in a (relatively simple) experimentally determined correlation giving C_D as a function of Reynolds number and aspect ratio. Second, by re-expressing the guessed *dimensional experimental design equation* as follows:

$$D = F\,(V, \rho, \mu, S, c) \tag{4.2}$$

In equivalent, and simpler dimensionless form, Eq. (4.1), we have *greatly* reduced the number of experiments required in order to fill out the (complicated) dependence of D on the set of dimensional variables listed in Eq. (4.2). For example, if we hadn't taken advantage of the Pi theorem and had used Eq. (4.2) to measure D at, say 10 different values of each of the five variables on the right of Eq. (4.2), we would need 10^5 separate experimental runs! By recasting Eq. (4.2) in dimensionless form, Eq. (4.1), we can obtain the same amount of experimental information using only 10^2 experiments (in this case varying Re and AR each over 10 representative magnitudes). Third, the much simpler dimensionless experimental design equation, Eq. (4.1), exposes, in much simpler fashion than Eq. (4.2), the essential physical and geometric features that determine the drag force on wings.

In the section 4.4, we will apply dimensional analysis to the important problem of recasting existing dimensional correlations connecting measured stress intensities and crack velocities observed in double torsion stress relaxation experiments in rock [1], [153], [34], [38], [35].

4.3 Double Torsion (DT) Stress Relaxation Test

The double torsion method provides a useful experimental approach for investigating time-dependent fracture processes in brittle materials like rock under various environmental conditions. It uses a special specimen configuration and loading setup, with forces applied to create a torsional stress state. The load relaxation (RLX) method is commonly used with the DT test to determine the relationship between stress intensity factor (K_I) and crack velocity (V). This $K_I - V$ relationship allows researchers to evaluate subcritical crack growth parameters like the subcritical crack growth index denoted by n. The test procedure typically involves the following items:

1) Pre-cracking the specimen to a specified initial crack length.
2) Setting and controlling environmental conditions, i.e., temperature and humidity.
3) Applying load and measuring load relaxation over time.

Care must be taken with specimen thickness and loading conditions to prevent unwanted effects like friction or locking at the crack surfaces. The DT test allows subcritical crack growth to be measured under controlled environmental conditions to study factors like temperature, humidity, and presence of water. Data from DT tests can be used to estimate long-term strength of materials by extrapolating subcritical crack growth behavior. Researches have been used this method for the mentioned purposes. For example, Nara et al. [7] employed the double torsion technique to study the effect of temperature and environmental humidity on different rock strength. The researchers followed a consistent procedure for all experiments, using the same apparatus and loading conditions as described in their previous studies. They began by pre-cracking the specimen to a standardized initial crack length of 25 mm, as recommended by another researcher. The environmental conditions were then carefully controlled and maintained constant throughout the testing period. After allowing the apparatus and specimen to equilibrate in the testing environment for over 20 hours, they conducted the subcritical crack growth measurements using the DT-RLX method. This approach enabled them to obtain the relationship between stress intensity factor and crack velocity , which is crucial for evaluating subcritical crack growth parameters and understanding the influence of environmental factors on crack propagation in igneous rocks.

In another research from Nara et al., [42] they investigated the effects of different guide groove shapes on DT test results for andesite rock specimens. Three guide groove shapes were tested: rectangular, semi-circular, and triangular. The experiments were performed under controlled temperature and humidity conditions. The results showed that samples having rectangular guide grooves produced the most consistent and reproducible stress intensity factor versus crack velocity relationships. The data for rectangular grooves exhibited the highest linearity and least scattering compared to the semi-circular and triangular grooves. Based on these findings, Nara concluded that rectangular guide grooves are most appropriate for DT testing of rock specimens, as they allow cracks to propagate along the path of least resistance without artificial constraints.

Ma et al. [45] conducted double torsion tests on five rock types called basalt, granite, marble, red sandstone, and white sandstone to investigate subcritical crack growth (SCG) and dynamic fractures. Their samples for double-torsion test had 1 mm deep guide groove along the center, and a 10 mm initial notch. The test procedure involved three main steps called pre-cracking, relaxation, and rapid loading. In the pre-cracking step, samples were loaded at 0.05 mm/min until a load drop occurred, creating a steady crack front and extending the crack beyond 33 mm. During relaxation step, samples were reloaded to 90% of the peak pre-cracking load at 0.5 mm/min, then held at constant displacement for 15 minutes to allow relaxation. During rapid loading step, samples were finally loaded at 5 mm/min until complete fracture. They applied digital image correlation (DIC) to analyze the fracture process zone (FPZ) evolution and extract key fracture parameters. This method allowed them to examine differences in fracture behavior at microscopic and mesoscopic scales between subcritical and dynamic fractures for the various rock types. Li et al. [154] demonstrated the effectiveness of the double-torsion method, combined with 3D-DIC, in investigating the thermal effects on fracture behavior and subcritical crack growth in granite, which is crucial for assessing the long-term stability of nuclear waste disposal projects. Some important findings from double-torsion (DT) tests can be summarized as follows:

1) Relationship between stress intensity factor and crack propagation velocity followed Charles' law during relaxation tests.

2) As treatment temperature increased to 400^oC, subcritical crack propagation velocity accelerated, resulting in longer subcritical cracks during relaxation tests.

3) Subcritical crack growth index (n) showed a complex relationship with treatment

temperature, initially decreasing, then increasing, and finally decreasing again.

Nakagawa et al. [155] used DT test to investigate critical and subcritical propagation of slow-moving tensile cracks. The DT test involves growing a single crack along the center line of a thin rectangular plate supported at its four corners. A concentrated force is applied to one edge of the plate, causing bending and crack propagation. Measurements typically include displacement and force at the loading point, as well as crack length during the experiment. The test provides data on the relationship between crack velocity and strain energy release rate (or stress intensity factor). The crack growth behavior is typically divided into three regions called region I, region II, and dynamic propagation. Region I is known as slow, chemical-reaction-controlled growth. Region II is related to transport-dominated growth, and ultimately dynamic propagation. Their applied method improves the validity of results in Regions II and III. Also, it allows for quantitative estimation of crack behavior controlled by fluid transport and chemical interactions near the crack tip. Furthermore, their approach can be used to investigate the impact of humidity and fluid chemistry on subcritical crack growth in brittle solids.

4.4 Proposed Essential Dimensional Variables for Non-dimensionalizing Dimensional Rock Fracture Velocity Data

Our initial guesses for the set of essential dimensional parameters and their corresponding dimensions, along with detailed explanations for each parameter are as follows:

1) Stress intensity factor ($[K_I] = \frac{N}{m^{(3/2)}}$): Stress intensity factor measures the stress state near the tip of a crack and is crucial in determining whether a crack will prop-

agate. Higher values indicate greater potential for crack growth.

2) Crack length ($[a] = m$): Crack length is the measure of the size of the crack. It directly influences the stress intensity factor and, hence, the potential for crack propagation.

3) Applied Stress ($[\sigma] = \frac{N}{m^2}$): Applied stress is the external load per unit area acting on the material. It drives the crack growth process.

4) Crack Growth Rate ($[\frac{da}{dt}] = \frac{m}{s}$): This is the rate at which the crack length increases during any given stress relaxation experiment.

5) Material properties: Material properties include fracture toughness, Young's modulus and density.

6) Fracture Toughness ($[K_{IC}] or [K_C] = \frac{N}{m^{(3/2)}}$): Fracture toughness is the critical value of the stress intensity factor at which rapid crack propagation occurs. In fact, it represents the material's resistance to fracture.

7) Young's Modulus ($[E] = \frac{N}{m^2}$): It measures the material's stiffness, indicating how much it will deform elastically under a given stress.

8) Density ($[\rho] = \frac{kg}{m^3}$): It is the mass per unit volume of the material, influencing its inertial properties and wave propagation speeds.

9) Sound Speed (P-wave Velocity, $[v_p] = \frac{m}{s}$): The speed of P-waves through the material, influenced by its density and elastic properties, is critical for understanding

dynamic stress fields and crack propagation.

As discussed in analysis of the results, we find out that there are two distinct subcritical crack growth regimes called slow and fast regimes where a threshold stress intensity for initiation of slow growth, $K_{th,slow}$, is hypothesized and is given approximately by:

$$K_{th,slow} \approx \sigma_T \sqrt{d_{gb}} \tag{4.3}$$

where $d_{gb} \approx 10 \times (10^{-9})\,\mathrm{m}$ is the grain boundary thickness. Moreover, our data indicate that a second threshold stress intensity, $K_{th,fast}$, marking the beginning of the fast regime, is given approximately by:

$$K_{th,fast} \approx \sigma_T \sqrt{d_g} \tag{4.4}$$

Thus, using this information to construct the dimensional experimental design equation, we will include σ_T, d_{gb}, and d_g in the set of essential dimensional variables determining subcritical crack growth, where $[\sigma_T] = \frac{N}{m^2}$, $[d_{gb}] = m$, and $[d_g] = m$.

For completeness, we identify temperature and humidity as two essential environmental parameters that each play an important role in rock fracture. Temperature affects the material properties and the crack growth rate, particularly in thermally sensitive materials, while relative humidity can influence crack growth by promoting stress corrosion cracking in susceptible materials. In this study, representing the first application of dimensional analysis to rock fracture measurements obtained by the widely used double beam stress relaxation test, we will focus on data obtained under relatively fixed temperature and relative humidity conditions.

Based on the above list of guessed essential variables and parameters, and choosing dimensional fracture growth rate as the dependent variable of interest, we obtain a generic, dimensional experimental design equation:

$$\frac{da}{dt} = F\left(K_I, K_c, E, \rho, \sigma_T, d_g, d_{gb}, v_p, a, \sigma\right) \tag{4.5}$$

4.5 Derivation of Dimensionless Experimental Design Equations

With the aim of developing the simplest possible nondimensional experimental design equation, we limit attention to double torsion stress relaxation experiments carried out on a single, but geologically important rock type, Western granite [7]. Given the complexity of the *dimensional* experimental design equation, Eq. (4.5) - arising due to the large number of essential variables underlying subcritical rock fracture - it is essential that individual dimensionless correlations remain limited to either specific rock types or families of mineralogically similar rock types.

Importantly, once this choice is made, we can identify the rock material properties appearing in Eq. (4.5), v_p, K_c, E, ρ, and σ_T, as fixed parameters, and thus as potential candidates for elimination from Eq. (4.5). A similar remark applies to the structural properties, d_{gb} and d_g.

4.5.1 Constraining the Dimensionless Model Space Using Auxiliary Relationships

A further tack available for deriving maximally simplified dimensionless experimental design equations centers on identifying redundant dimensional variables in the guessed dimensional experimental design equation. In Eq. (4.5), we recognize from elastic fracture mechanics [144]

$$K_I \propto \sigma\sqrt{a} \tag{4.6}$$

a proportionality that suggests that we either eliminate K_I in favor of keeping σ and a, or vice versa. Since the first approach eliminates two variables from Eq.(4.5), this strategy is indicated and indeed, as shown in the results, proves advantageous. More generally and with regard to 'redundant dimensional variables,' we highlight four important points:

1) When inspecting a set of guessed essential dimensional variables, one should recall any known physical, geometric, and/or empirical relationships connecting subsets of variables on the list. Each one of these relationships can then be used to identify potentially redundant dimensional variables.

2) In cases where multiple relationships are identified, one should, on a first (or initial) attempt(s), use these to eliminate, as we've done here, the maximum number of dimensional variables possible.

3) The process of identifying auxiliary relationships and using these to eliminate redundant dimensional variables, in effect, shrinks and constrains the dimensionless model space within which we are attempting to expose fracture rate correlations.

4) In addition to physical, geometric and empirical relationships, order of magnitude analyses of physical processes underlying rock fracture can also be used to expose additional, qualitative relationships involving the set of guessed essential dimensional variables. Eqs. (4.3) and (4.4) are relevant examples, which we discuss below.

4.5.2 Questions and Arguments Leading to a Final Dimensionless Experimental Design Equation

Atkinson [156] first showed that the dimensional Charles' law correlation [157], relating subcritical fracture growth rate, $\dot{a}$, to stress intensity, K_I :

$$\frac{da}{dt} = \dot{a} = AK_I^n \tag{4.7}$$

holds for many rock types undergoing tensile-driven subcritical fracture. Here, n, the subcritical fracture index or stress corrosion index, can be taken as a rock-specific, temperature- and humidity-dependent rock material property [20]:

$$n = n\left(T, RH\right) \tag{4.8}$$

The coefficient, A, is likewise material-specific and temperature and humidity dependent. A typical set of experimental observations, obtained during double torsion stress relaxation experiments in Western granite, as reported by Nara et al. [7], is shown in Fig. 4.2.

While it is clear that the *dimensional* Charles' law well-correlates subcritical crack growth rate and stress intensity in rock, two important questions nevertheless emerge:

First, it is observed that measured stress corrosion indices in rock often assume large magnitudes; in granite, for example, typical values range over $30 < n < 90$ [7]. Power law exponents of these magnitudes, describing physical processes, appear to be quite unusual. Mathematically, large $n's$ indicate that tensile, subcritical fracture growth in rock is *extremely* nonlinear. We are thus lead to the question: Do large $n's$ observed in *dimensional* Charles law correlations reflect actual, highly-nonlinear physical processes, or might they reflect, for example, a simple mathematical pathology introduced by stating correlations in dimensional form?

Second, and referring to Fig. 4.2, we observe that while the slopes - corresponding to n - of measured crack growth rate, $\dot{a}$, versus measured stress intensity, K_I, remain nominally fixed over the series of individual (double - torsion) stress relaxation tests performed, the set of individual plots exhibit an obvious lateral spread. Here, we ask: Can the apparent offsets in individual plots be removed or minimized by expressing measured $\dot{a}'s$ and $K_I's$ in rescaled form, where plots of the rescaled variables fall on, or remain close to a single plot?

4.5.3 Nondimensionalization Based on the Generalized Compressibility Chart

Considering the second question first, we gain essential clues on how to proceed from the generalized compressibility chart [6], [158]. The chart, an example of which is shown in Fig. 4.1, and which corresponds to an empirical pressure-volume-temperature (PVT) equation of state for a large family of small, monatomic and polyatomic gasses, plots the so-called compressibility factor,

$$Z = \frac{PV}{RT} \tag{4.9}$$

versus dimensionless, or reduced pressure,

$$P_R = \frac{P}{P_c} \tag{4.10}$$

and reduced temperature

$$T_R = \frac{T}{T_c} \tag{4.11}$$

i.e., gives Z as an experimentally determined function of T_R and P_R :

$$Z = F\left(T_R, P_R\right) \tag{4.12}$$

Here, R is the universal gas constant, and P_c and T_c are gas-specific critical pressures and temperatures, respectively.

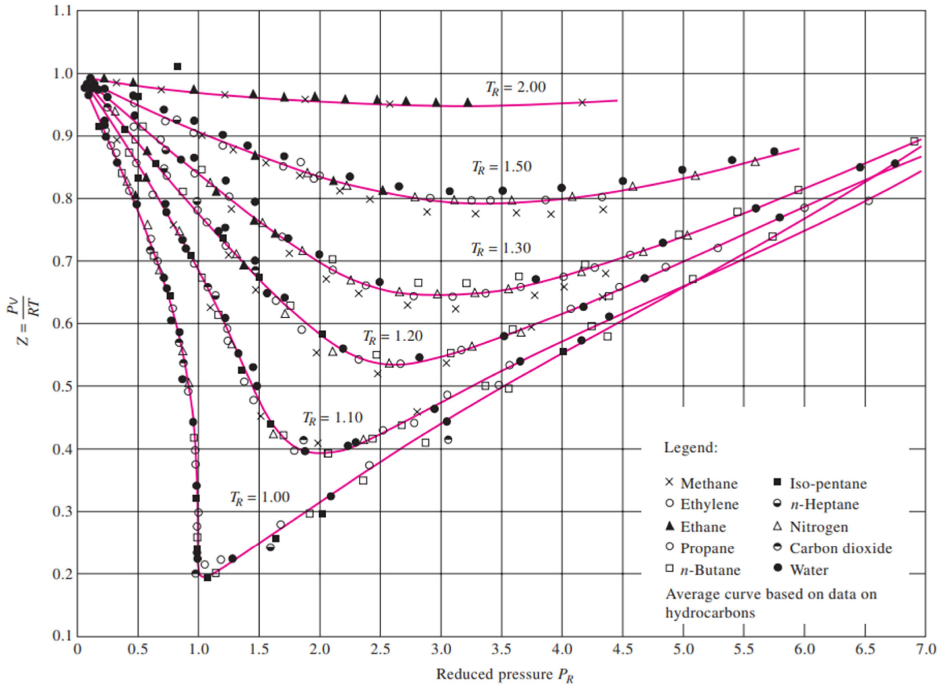

Figure 4.1: Compressibility chart for various gases under different conditions [6]

Importantly, the mathematical form and physical content of this correlation suggests strategies for recasting the dimensional Charles' law in dimensionless form:

1) The critical state, which appears when a fluid's temperature and pressure reach T_c and P_c, marks a distinct physical boundary: At fluid temperatures exceeding T_c, the fluid cannot be compressed into a liquid state, no matter how large the imposed pressure. [At temperatures slightly exceeding T_c, the fluid exists as a dense vapor. At $T >> T_c$, molecular kinetic energy is high enough to atomize vapor droplets into indi-

vidual atoms (atomic fluids) or molecules (molecular fluids).] Since all small-molecule fluids, at temperatures between T_c and the gas ionization temperature, $T_{ionization}$, $T_c \leq T \leq T_{ionization}$, exist in the same qualitatively distinct state – vaporous or atomized gas – and since T_c and $T_{ionization}$ are of similar orders of magnitude, then T_c provides a physically and quantitatively appropriate scale for correlating dimensionless gas temperatures. Similar comments apply to P_c.

2) Considering the qualitative nature of subcritical fracture in rock, we recognize crucial analogies with the states of gases:

a) Observable subcritical tensile fracture growth occurs over a bounded range of stress intensities:

$$K_{th} \leq K_I \leq K_c \tag{4.13}$$

where the threshold stress intensity for observable tensile fracture in granite, $K_{th} \approx 0.2 \times K_c$ [112]

b) Similar to the temperature-dependent transition from vaporous to ideal (atomized) gas states in small molecule gasses, we present evidence below that subcritical tensile rock fracture undergoes an analogous stress-intensity-dependent transition from slow, subgrain-scale fracture, and fast, multi-grain-scale fracture.

c) The critical fracture intensity, K_c, in analogy with the critical temperature in gasses, represents a measurable, rock-specific material property at which a fracturing rock system bifurcates from relatively slow, random, intermittent subcritical cracking to fast, deterministic, continuous fracture.

Thus, inspired by the example provided by the generalized compressibility correlation, we:

a) First hypothesize that the (apparently) random horizontal offsets in measured fracture rate, observed during repeat double torsion stress relaxation tests - as again illustrated in Fig. 4.2 - can be minimized by referencing individual $K_I^{(\alpha)}\prime s$ (measured during experimental run α) to the smallest stress intensity, $K_{I,min}^{(\alpha)}$, observed during the run;

b) Second, define a dimensionless stress intensity, $\tilde{K}_I$, by scaling the difference, $K_I^{(\alpha)} - K_{I,min}^{(\alpha)}$, with K_c :

$$\tilde{K}_I^{(\alpha)} = \frac{K_I^{(\alpha)} - K_{I,min}^{(\alpha)}}{K_c} \tag{4.14}$$

and

c) Third, define a corresponding dimensionless subcritical crack growth rate as

$$\tilde{\dot{a}}^{(\alpha)} = \frac{\dot{a}^{(\alpha)} - \dot{a}_{min}^{(\alpha)}}{v_p} \tag{4.15}$$

Note that our choice of v_p for the fracture velocity scale is determined by our choice of K_c for the stress intensity scale: Under conditions where critical fracture is not initiated, e.g., by impulsive rock motion along faults, the characteristic fracture speed is approximately v_p [159].

4.5.4 Final Generic Form of Dimensionless Experimental Design Equation

Based on the above arguments, we can now state a generic form of the dimensionless experimental design equation as follows:

$$\tilde{\dot{a}}^{(\alpha)} = \tilde{F}\left(\tilde{K}_I\right) \tag{4.16}$$

Also, by using the definitions of $\tilde{\dot{a}}$ and $\tilde{K}_I$ in Eqs. (4.15) and (4.14), Eq. (4.16) can be written as:

$$\frac{\dot{a}^{(\alpha)} - \dot{a}_{min}^{(\alpha)}}{v_p} = \tilde{F}\left(\frac{K_I^{(\alpha)} - K_{I,min}^{(\alpha)}}{K_c}\right) \tag{4.17}$$

4.5.5 Dimensionless Charles Laws for Slow, Subgrain-Scale and Fast, Multi-Grain-Scale Subcritical Fracture Growth

Since individual experimental measurements of tensile subcritical crack growth are well correlated by the dimensional Charles law, Eq. (4.7), we anticipate and show in the next section, that similar power law correlations hold when fracture data is recast in dimensionless form. Specifically, we find that the following dimensionless experimental design equations well-fit dimensionless tensile fracture data in Western granite:

$$\tilde{\dot{a}}_s = \tilde{A}_s \left[\frac{K_I - K_{atomic}}{K_c} \right]^{\tilde{n_s}} \qquad K_I < K_{th} \tag{4.18}$$

and

$$\tilde{\dot{a}}_f = \tilde{A}_f \left[\frac{K_I - K_{th}}{K_c} \right]^{\tilde{n_f}} \qquad K_I > K_{th} \tag{4.19}$$

where

$$\tilde{\dot{a}}_s = \frac{\dot{a}}{v_p} \tag{4.20}$$

and

$$\tilde{\dot{a}}_f = \frac{\dot{a} - \dot{a}_{th}}{v_p} \tag{4.21}$$

and where $\tilde{A}_s$ and $\tilde{A}_f$ are constants associated respectively with a slow, subgrain-scale fracture regime and a fast, multi-grain-scale regime, $\tilde{n}_s$ and $\tilde{n}_f$ are corresponding stress corrosion indices, and K_{atomic} is the threshold stress intensity for initiation of atomic-scale fracture, i.e., bond breaking.

4.6 Analysis of the Dimensional and Dimensionless Plots in Rocks

The following figures show both dimensional and dimensionless crack velocity versus stress intensity factor in Kumamoto Andesite, Oshima Granite and Inada Granite which are obtained under different enviromental conditions mainly different temperature and pH, respectively. It should be noted that dimensional plots are extracted from Nara's experimental work [7] which were done in 2013.

Figure 4.2 shows the relationship between crack velocity and stress intensity factor in Kumamoto andesite considering different temperature and pH conditions in distilled water. The plot includes data from eight different datasets, each representing different combinations of temperature and pH. As stress intensity factor increases, crack velocity shows a rise across all conditions tested. At lower temperatures of 284 - 286K and near-neutral pH of 6 - 7, crack velocity remains low, below $10^{-8}(m/s)$, even at relatively high stress intensity factors up to $1.3(MN/m^{(3/2)})$. However, when temperature is increased to 327 - 328K while maintaining a lower pH of 5, the crack velocity significantly increases, reaching velocities above $10^{-4}(m/s)$ at a stress intensity of $1.3(MN/m^{(3/2)})$. At an even higher temperature range of 344 â 346K and pH 5, the crack velocity further accelerates, surpassing $10^{-2}(m/s)$ at stress intensities above $1.3(MN/m^{(3/2)})$. The results demonstrate that higher temperatures promote faster crack propagation in Kumamoto andesite, likely due to thermally activated crack growth mechanisms. More neutral pH conditions also appear to retard crack velocity compared to the lower pH of 5 tested at higher temperatures.

By applying the developed dimensionless formulas which are obtained from dimensional analysis on both X and Y axes, i.e., stress intensity factors and crack velocity, respectively, the experimental data can be expressed in dimensionless form. Figure 4.3 shows the results of experimental data in Kumamoto andesite (KA) in dimensionless form which are obtained under both different temperatures and water pH. By expressing the crack velocity and stress intensity data in dimensionless form, two distinct crack growth regimes emerge in the Kumamoto andesite samples. At low dimensionless stress intensities almost below -3.5, the data shows a gradual linear rise

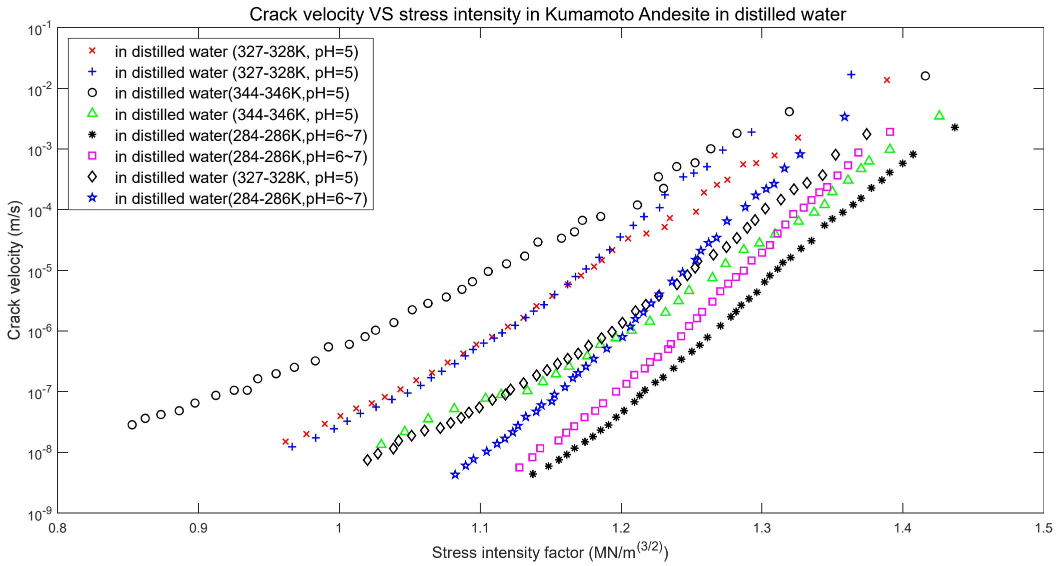

Figure 4.2: Crack velocity versus stress intensity in Kumamoto Andesite (KA) in distilled water under different temperature conditions obtained for eight separate data sets [7]

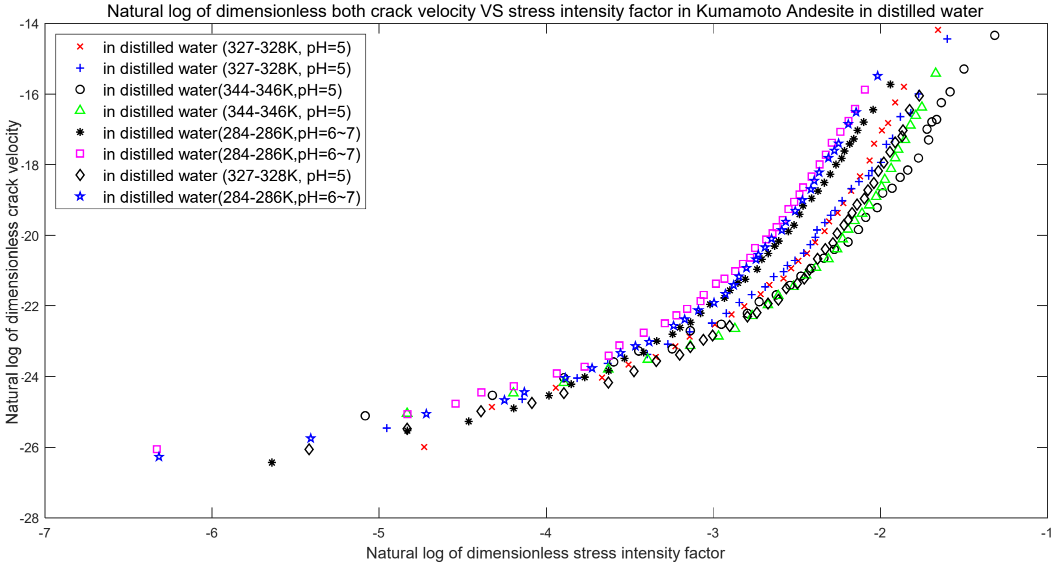

Figure 4.3: Dimensionless crack velocity versus dimensionless stress intensity factor in Kumamoto Andesite (KA) in distilled water under different temperature conditions

in natural log dimensionless velocity, representing stable, slow crack growth. However, above stress intensity factors of almost -3.5, the slope becomes much steeper, signaling the onset of unstable, fast crack growth.

The transition between slow and fast crack growth regimes occurs between -4 and -3 for the natural log of the dimensionless stress intensity factor. Across all temperature and pH conditions tested, the data exhibits this clear change in slope, demonstrating the accelerated crack velocity beyond a critical stress intensity point. Higher temperatures promote faster cracking, causing the unstable regime to appear at lower absolute stress intensities.

Applying the piecewise curve fitting on each of separate datasets obtained from dimensionless curve fitting leads to getting slopes (subcritical crack growth index) and intercepts in both slow and fast crack regimes in Kumamoto andesite (KA) datasets which are summarized in Table. 4.1.

Table 4.1: Piecewise curve fitting results of the Kumamoto Andesite in distilled water under different temperature conditions

Data sets	Slope (slow)	Intercept (slow)	Slope (fast)	Intercept (fast)	$R^2\%$
in distilled water (327-328K, pH=5)	1.879	-16.67	6.327	-4.915	99.22
in distilled water (327-328K, pH=5)	2.112	-16.08	7.875	-1.379	99.50
in distilled water (344-346K, pH=5)	1.542	-17.79	6.304	-6.23	99.10
in distilled water (344-346K, pH=5)	1.618	-17.72	7.701	-3.001	99.06
in distilled water (284-286K, pH=6-7)	1.746	-17.21	6.126	-4.077	99.31
in distilled water (284-286K, pH=6-7)	1.293	-18.52	5.998	-3.775	98.89
in distilled water (327-328K, pH=5)	1.505	-18.35	6.842	-4.37	99.29
in distilled water (284-286K, pH=6-7)	1.249	-18.91	6.309	-3.234	99.12

Figure 4.4 displays experimental crack propagation data for an igneous rock called

Oshima granite under air environments with varying temperature and humidity conditions. As seen in this figure, crack velocity shows nonlinear dependence on the increasing stress intensity factor across different temperatures and humidity levels. At higher temperatures of 330K and 86 % humidity, crack velocities accelerate rapidly, exceeding $10^{-3}(m/s)$ at stress intensities above $1.7(MN/m^{(3/2)})$. In contrast, at lower temperatures of 293K with 88-91% humidity, crack growth is significantly slower, with velocities plateauing around $10^{-5}(m/s)$ even at intensities of $1.8(MN/m^{(3/2)})$. The six separate data sets exhibit consistent velocity-intensity trends within each temperature regime. The cracking rise rate and subsequent plateau suggests a critical stress intensity threshold may exist for unstable fracture in the Oshima granite samples. Temperature demonstrates a distinct impact on the propagation rate, overtaking humidity effects.

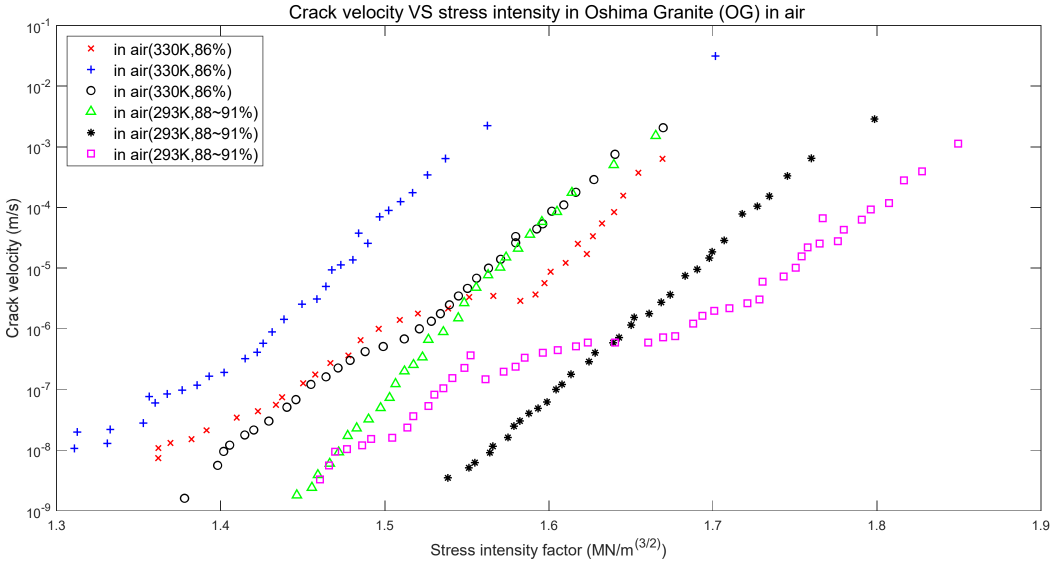

Figure 4.4: Crack velocity versus stress intensity in Oshima Granite (OG) in air under different temperature conditions obtained from six separate datasets [7]

Applying the introduced dimensionless formulas result in distinguishing two distinct crack regimes in each separate dataset. Figure 4.5 shows the obtained results from expressing experimental data in dimensionless form. As shown, below almost -3.5 for the natural log of the dimensionless stress intensity factor, the crack velocity increases gradually, representing micro-fracturing processes that dissipate energy ahead of the crack tip. However, beyond that point, in all separate datasets, indicating an unstable acceleration of fracture. This intensification aligns with breakdown of crack tip bonds and rapid release of stored strain energy. The transition between the two regimes therefore signals a shift from slow benign microcracking to dangerous unstable failure. Monitoring the natural log of the dimensionless stress intensity factor could give early warning of approaching critical levels in granite constructions such as dams or nuclear facilities. Accelerated slope changes beyond -3.5 intensity highlights zones where small stress perturbations may trigger runaway cracking.

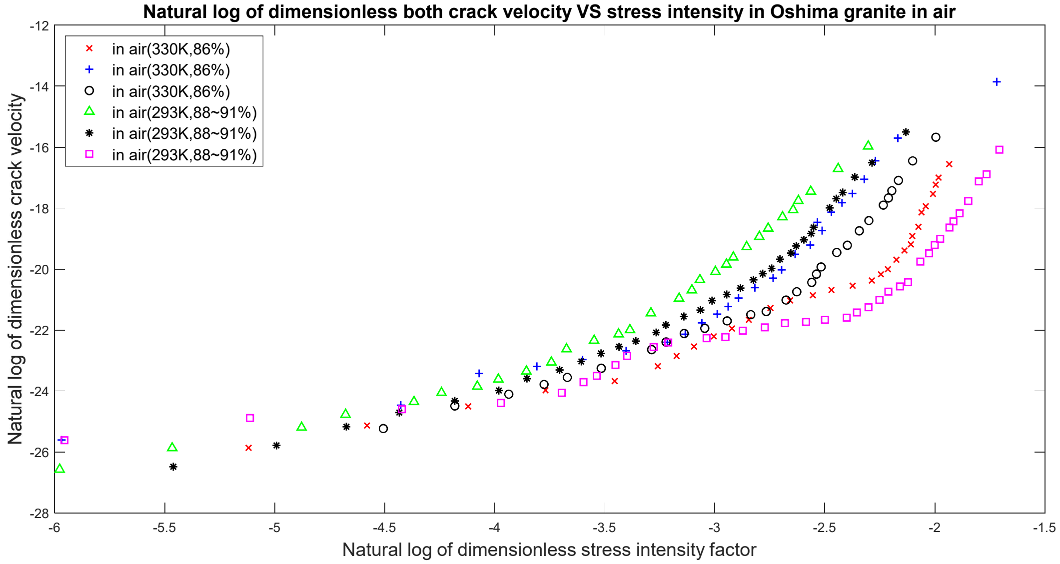

Figure 4.5: Dimensionless crack velocity versus dimensionless stress intensity factor in Oshima Granite (OG) in air under different temperature conditions

Based on the introduced dimensionless formulas for both stress intensity factors and crack velocity, and by applying picewise curvefitting on the obtained dimensionless data, two distinct crack regimes can be recognized for Oshima granite under different temperature conditions. Table 4.2 shows the piecewise curve fitting results of the Oshima granite under different temperature conditions in air.

Table 4.2: piecewise curve fitting results of the Oshima granite under different temperature conditions in air

Data sets	Slope (slow)	Intercept (slow)	Slope (fast)	Intercept (fast)	$R^2\%$
in air (293K, 88-91 %)	2.108	-15.72	13.46	9.501	98.66
in air (330K, 86 %)	1.224	-18.52	6.471	-2.241	99.09
in air (330K, 86 %)	2.31	-14.96	8.146	0.4621	99.81
in air (330K, 86 %)	1.685	-16.77	5.544	-3.337	99.65
in air (293K, 88-91 %)	2.153	-15.01	6.666	-1.481	99.36
in air (293K, 88-91 %)	1.34	-18.35	9.429	-0.2684	98.48

Figure 4.6 displays a supplementary data exploring effects of aqueous environments on crack propagation in Oshima granite samples. A similar nonlinear acceleration of crack velocity with increasing stress intensity factor is observed, influenced by the temperature and pH of the distilled water. At higher temperatures of 327â329 K and pH levels of 5â7, crack velocities surge above $10^{-4}(m/s)$ at stress intensity factors around $1.5(MN/m^{(3/2)})$. The three overlapping datasets showcase the consistency of these observations. When comparing the results directly to the air environment tests, it is evident that distilled water universally enhances crack growth rates and

reduces the required stress intensity for acceleration. This emphasizes water's role in interacting with crack tip bonds, promoting hydrolysis of microcracks that facilitates crack propagation. The combination of thermal energy and water effects dramatically accelerates fracture compared to cooler, drier conditions.

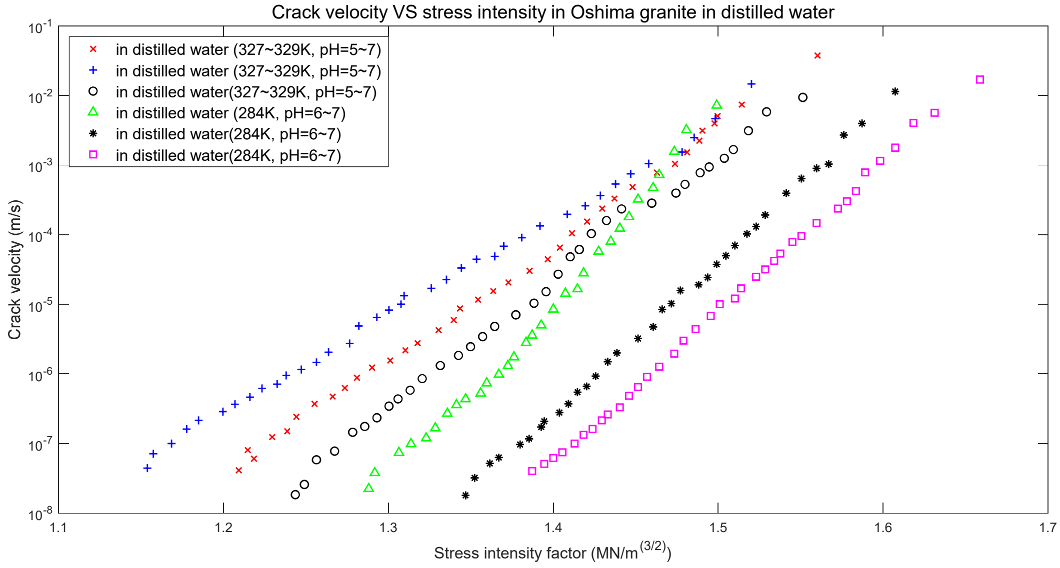

Figure 4.6: Crack velocity versus stress intensity in Oshima Granite (OG) in distilled water under different temperature conditions obtained from six separate datasets [7]

The dimensionless representation of the aqueous granite data further highlights the presence of two distinct cracking modes - a stable, slow growth regime at lower dimensionless stresses up to around -3, transitioning to unstable acceleration beyond this point as shown in figure 4.7. At dimensionless intensities around below -3, crack propagation remains gradual, with microcracking dissipating energy at the crack tips. However, beyond this critical point, the steepening slope reflects runaway fracture breakdown releasing stored elastic strain. The consistency of this transition pattern with the air environment data supports an intrinsic physical principle separating the regimes, potentially universal across different environments and rock types. The subcritical crack growth index appears to be the key marker indicating shift from slow benign microfracturing to dangerous, unstable propagation.

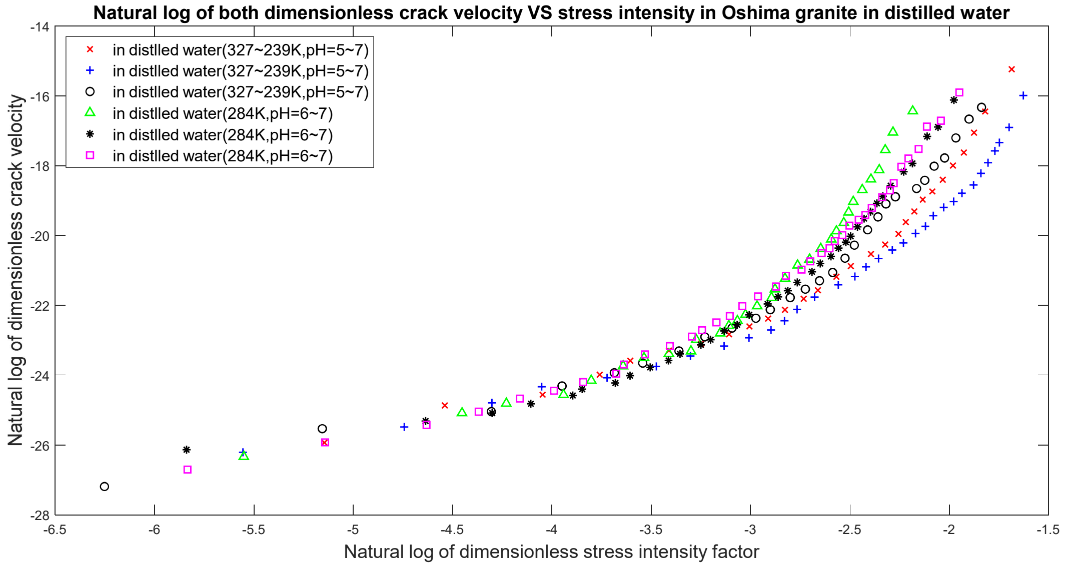

Figure 4.7: Dimensionless crack velocity versus dimensionless stress intensity in Oshima Granite (OG) in distilled water under different temperature conditions obtained from six separate datasets

Table 4.3 shows the piecewise curve fitting results of Oshima granite in distilled water under different temperature condition.

Table 4.3: Piecewise curve fitting results of the Oshima granite in distilled water under different temperature condition

Data sets	Slope (slow)	Intercept (slow)	Slope (fast)	Intercept (fast)	$R^2\%$
in distilled water (284K, pH=6-7)	1.401	-18.7	6.193	-4.327	98.77
in distilled water (284K, pH=6-7)	1.689	-17.39	5.79	-5.097	98.91
in distilled water (284K, pH=6-7)	1.631	-17.71	7.137	-1.224	98.98
in distilled water (327-329K, pH=5-7)	1.369	-18.84	4.937	-8.945	98.82
in distilled water (327-329K, pH=5-7)	1.455	-18.3	5.755	-5.957	99.40
in distilled water (327-329K, pH=5-7)	1.694	-17.42	6.663	-4.614	99.11

Figure 4.8 displays crack propagation data in Kumamoto andesite samples under specific environmental conditions: 50 % air humidity at 348K and distilled water at 344-346K. The nonlinear increase in crack velocity with rising stress intensity factor is evident across these different conditions. The humidity air environment 50 % shows a retardation of velocity compared to full water immersion, with the velocity plateauing at around $10^{-5}(m/s)$ by the maximum tested stress intensity factor. However, the exponential trend still emerges. When comparing these conditions, aqueous exposure

universally promotes faster crack propagation at a given stress intensity. This is likely due to water penetrating microcracks, hydrating the crack tips and bonds, thereby enhancing breakdown reactions and increasing crack mobility. The combined effect of thermal energy and water significantly accelerates the crack propagation rate compared to drier conditions.

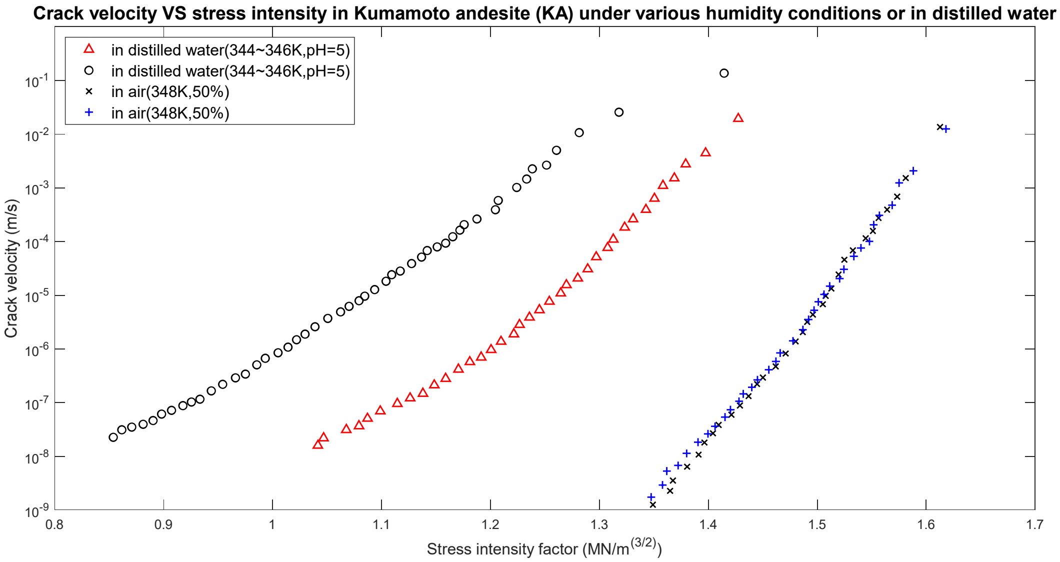

Figure 4.8: Crack velocity versus stress intensity in Kumamoto andesite under various humidity conditions or in distilled water at 344 - 348K from four separate experimental datasets [7]

The dimensionless representation of the Kumamoto andesite data, spanning air and water environments, further reveals the presence of two distinct crack growth modes: a stable, slow growth regime at lower dimensionless stresses up to around -2.5 (considering all datasets simultaneously), transitioning to unstable, fast propagation beyond this point. Figure 4.9 shows these results in detail. At lower dimensionless stress intensities below -2.5, the gradual increase in crack velocity indicates dissipative microfracturing behavior occurring ahead of the crack tips. However, beyond

-2.5, the slope steepens dramatically, reflecting the onset of runaway cracking and the rapid release of stored elastic strain energy. This consistent pattern, observed despite varying humidity and water immersion conditions, suggests an intrinsic physical principle governing the transition from slow, benign microscale damage to unstable macroscale failure.

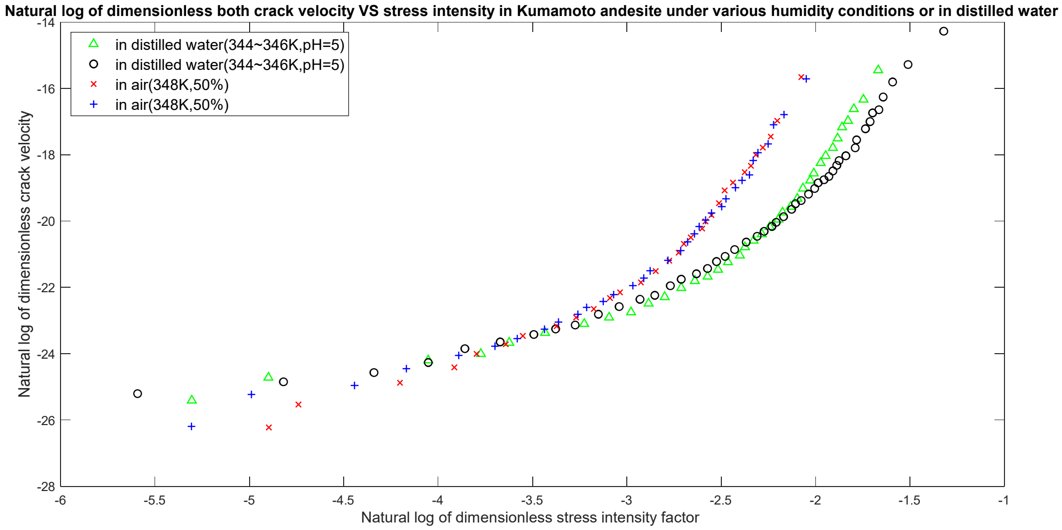

Figure 4.9: Dimensionless crack velocity versus dimensionless stress intensity in Kumamoto andesite under various humidity conditions or in distilled water at at 344-348K obtained from four separate datasets

The obtained slopes and intercepts results in both slow and fast crack regimes in Kumamoto Andesite under various humidity conditions or in distilled water at 344-348K using piecewise curve fitting are summarized in table 4.4:

Table 4.4: Piecewise curve fitting results of the Kumamoto andesite under various humidity conditions or in distilled water at 344-348K

Data sets	Slope (slow)	Intercept (slow)	Slope (fast)	Intercept (fast)	R^2%
in distilled water (344-346K,pH=5)	1.346	-18.52	7.262	-3.797	99.10
in distilled water (344-346K,pH=5)	1.386	-18.26	6.045	-6.651	98.76
in air (348K, 50 percent)	2.152	-15.73	7.588	-0.3494	99.56
in air (348K, 50 percent)	1.785	-16.86	7.398	-0.8861	99.26

Figure 4.10 shows extensive datasets which explores the effects of humidity and water immersion on crack growth rates in Oshima granite. Exponential acceleration of velocity with rising stress intensity persists across diverse environments. In distilled water at 327-329K and pH 5 - 7, velocities surge over $10^{-3}(m/s)$ at stress intensity factors around $1.5(MN/m^{(3/2)})$. The triplicate data showcase reproducibility, with thermal water activity dramatically enhancing propagation. Under 86 % humidity air at 330K, velocity enhancement is present but moderated, plateauing around $10^{-5}(m/s)$ by a stress intensity of approximately $1.9(MN/m^{(3/2)})$. A 71 % humidity shows further retardation but with a nonlinear trend still evident.

Figure 4.11 represents the obtained experimental data in dimensionless form, revealing the dual cracking mode transition - from stable slow propagation at low dimensionless stresses up to around -3, to unstable acceleration beyond this critical point. At lower dimensionless stress intensity factor below -3, the gradual increase in

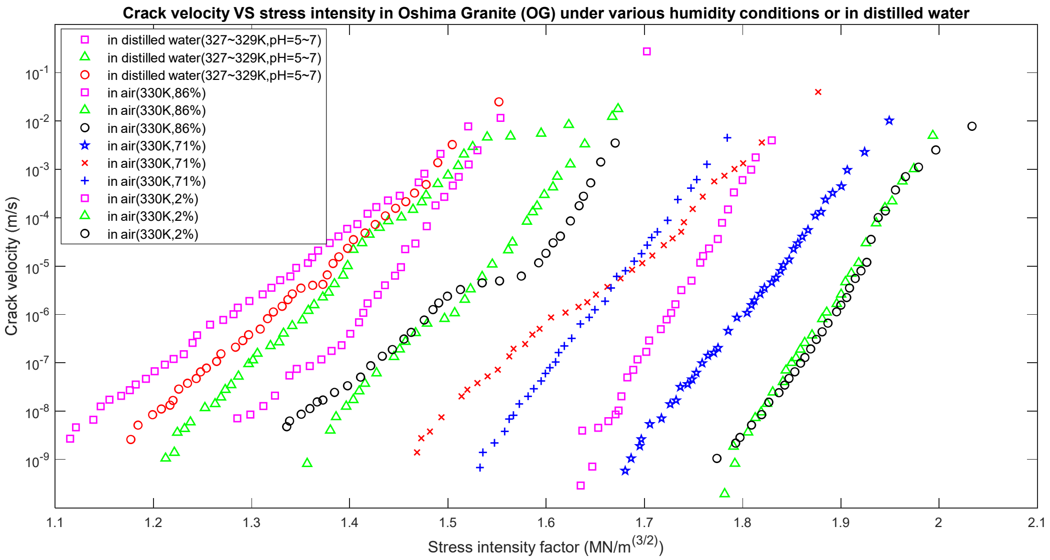

Figure 4.10: Crack velocity versus stress intensity in Oshima granite under various humidity conditions or in distilled water at 327 - 330K from twelve separate experimental datasets [7]

crack velocity indicates dissipative microfracturing behavior ahead of the crack tips. However, beyond -3, the steep slope indicates the onset of uncontrolled cracking, rapidly releasing stored elastic strain energy. The uniform characteristic exhibited by this transition pattern, even in diverse environments with varying humidity levels and water pH, reinforces an inherent physical principle that distinguishes between different regimes. The dimensionless stress intensity factor appears to serve as a universal indicator, signifying the transition from minor microscale damage to critical macroscale failure.

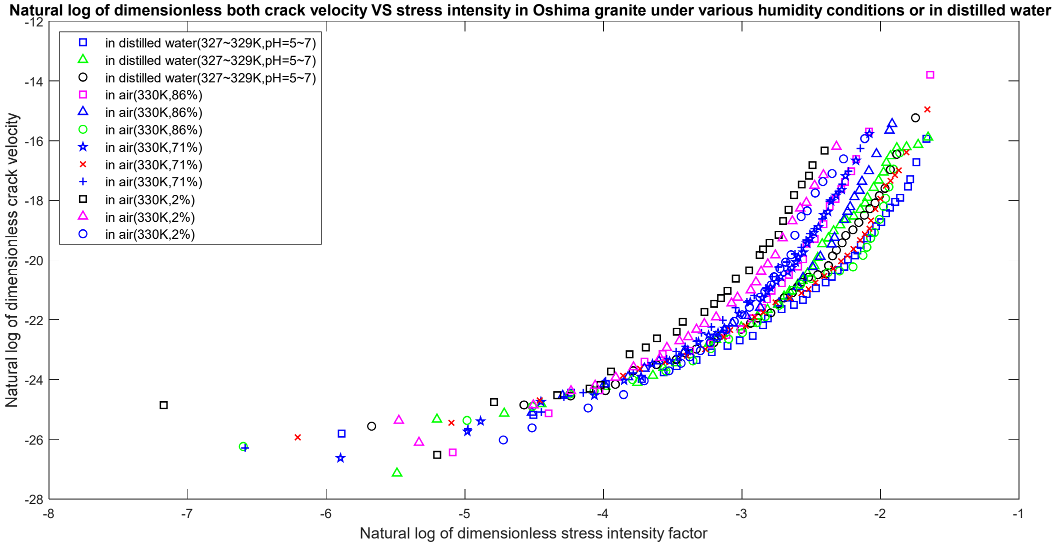

Figure 4.11: Dimensionless crack velocity versus dimensionless stress intensity in Oshima granite under various humidity conditions or in distilled water at 327-330K obtained from twelve separate datasets

The obtained slopes, i.e., subcritical crack growth index and their related intercepts in both slow and fast crack regimes in Oshima granite under various humidity conditions or in distilled water at 327 - 330K using piecewise curve fitting are summarized in table 4.5.

Table 4.5: Piecewise curve fitting results of the Oshima granite under various humidity conditions or in distilled water at 327-330K

Data sets	Slope (slow)	Intercept (slow)	Slope (fast)	Intercept (fast)	R^2%
in distilled water (327-329K,pH=5-7)	1.27	-18.95	5.235	-8.08	98.44
in distilled water (327-329K,pH=5-7)	1.7	-17.32	5.602	-6.112	99.22
in distilled water (327-329K,pH=5-7)	1.392	-18.33	5.727	-6.178	98.31
in air (330K, 86 %)	2.031	-16.11	6.939	-1.87	99.39
in air (330K, 86 %)	2.148	-15.55	8.285	-0.2603	99.72
in air (330K, 86 %)	1.431	-18.01	6.547	-5.201	95.05
in air (330K, 71 %)	1.715	-17.08	7.014	-1.558	99.06
in air (330K, 71 %)	1.459	-17.80	7.284	-3.367	98.24
in air (330K, 71 %)	1.267	-18.78	5.677	-4.663	98.23
in air (330K, 2 %)	0.6626	-21.2	5.759	-2.937	95.65
in air (330K, 2 %)	1.619	-17.26	6.75	-0.9093	98.80
in air (330K, 2 %)	2.24	-15.63	7.35	0.0034	99.20

Figure 4.12 shows the obtained experimental data of crack velocity versus stress intensity factor for Oshima granite under different humidity conditions and in distilled water at at 330K. This additional Oshima granite dataset examines the effects of 70 - 71 % relative humidity and very low humidity of 2 % on crack growth propagation. The characteristic nonlinear acceleration of velocity as stress intensity increases persists in both environmental conditions. Under the elevated 70 - 71 % humidity condition at 330K, crack velocities increase rapidly from approximately $10^{-7}(m/s)$ up to nearly $10^{-3}(m/s)$ as stress intensity factor approaches $2(MN/m^{(3/2)})$. The triplet of overlapping data highlights the reproducibility and consistency of the effects observed under similar conditions.

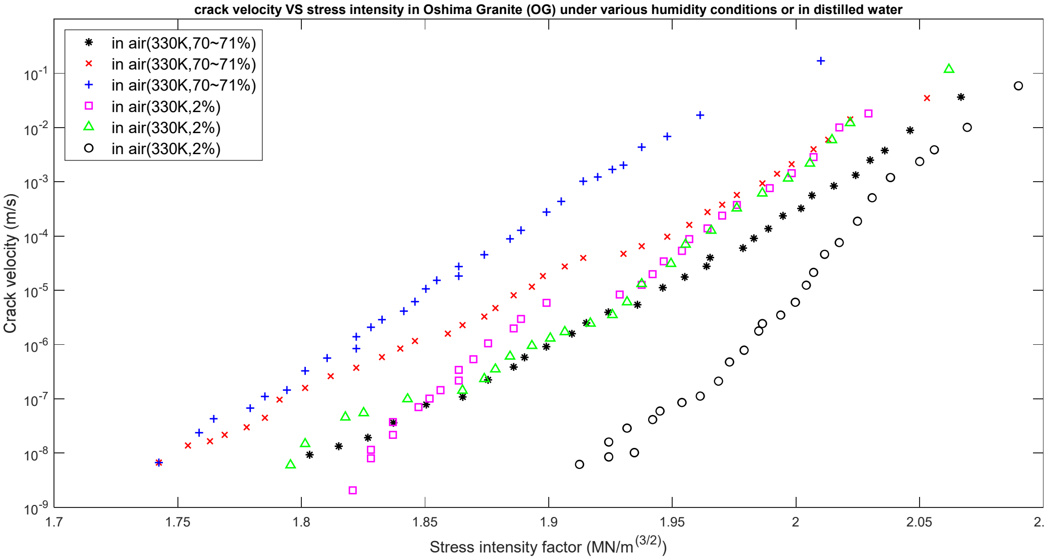

Figure 4.12: Crack velocity versus stress intensity in Oshima granite under various humidity conditions or in distilled water at at 330K from six separate experimental datasets [7]

Applying the introduced dimensionless formulas on both crack velocity and stress intensity experimental data result in the identification of two distinct crack regimes for each separate dataset. Figure 4.13 illustrates the obtained results. The dimensionless representation of the Oshima granite data at 70 - 71 % and 2 % relative humidity continues to showcase the dual-mode cracking behavior - from stable, slow propagation at low dimensionless stress intensities up to around -3, to unstable rapid acceleration beyond this point. For dimensionless stress intensities below -3, there is a gradual increase in crack velocity, indicating dissipative microfracturing processes occurring ahead of the crack tips. In contrast, at dimensionless stress intensities beyond -3, a sudden increase in slope signifies the initiation of uncontrolled cracking, leading to a rapid release of stored elastic strain energy. The consistent pattern of this transition reinforces an intrinsic physical principle governing the shift from benign microscale damage to dangerous macroscale failure, regardless of humidity changes.

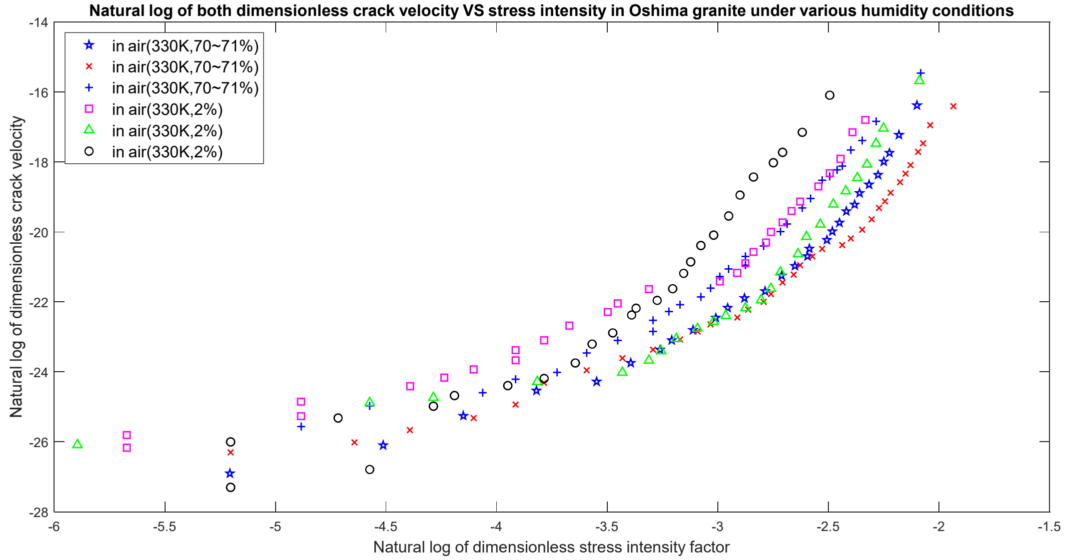

Figure 4.13: Dimensionless crack velocity versus dimensionless stress intensity in Oshima granite under various humidity conditions or in distilled water at at 330K for six separate data sets

The obtained slopes, i.e., subcritical crack growth index and intercepts in both slow and fast crack regimes for Oshima granite under under various humidity conditions or in distilled water at 330K using piecewise curve fitting are summarized in table 4.6.

Table 4.6: piecewise curve fitting results of the Oshima granite under various humidity conditions or in distilled water at 330K

Data sets	Slope (slow)	Intercept (slow)	Slope (fast)	Intercept (fast)	$R^2\%$
in air (330K, 70-71 percent)	2.105	-16.38	7.108	-2.054	98.96
in air (330K, 70-71 percent)	1.878	-17.18	6.042	-5.258	98.76
in air (330K, 70-71 percent)	1.961	-16.26	6.337	-2.543	99.30
in air (330K, 2 percent)	1.783	-16.24	7.332	0.1493	99.10
in air (330K, 2 percent)	1.203	-19.34	8.414	1.678	99.10
in air (330K, 2 percent)	2.075	-16.08	7.219	1.82	98.51

Figure 4.14 shows the obtained experimental data of crack velocity versus stress intensity factor for Inada granite under various humidity conditions or in distilled water at at 293K. This dataset investigates how crack growth rates in Inada granite samples are influenced by exposure to air with 53 % humidity and immersion in distilled water. In both environments (conditions), there is a distinctive nonlinear pattern, wherein the crack velocity accelerates with increasing stress intensity factor. Under full immersion in distilled water at 293K and pH 7 - 8, the crack velocity increases rapidly from $10^{-7}(m/s)$ up to nearly $10^{-2}(m/s)$ as the stress intensity factor reaches $1.6(MN/m^{(3/2)})$. This significant increase compared to dry conditions suggests that

water penetration and chemical reactions mechanisms activating crack propagation. In contrast, under 53 % humidity in air, crack propagation is significantly restrained, with velocities only reaching about $10^{-3}(m/s)$ even at the maximum applied stress intensity. This reduction in crack velocity under humid air conditions implies that humidity alone is insufficient to trigger the same aqueous acceleration observed under full water immersion.

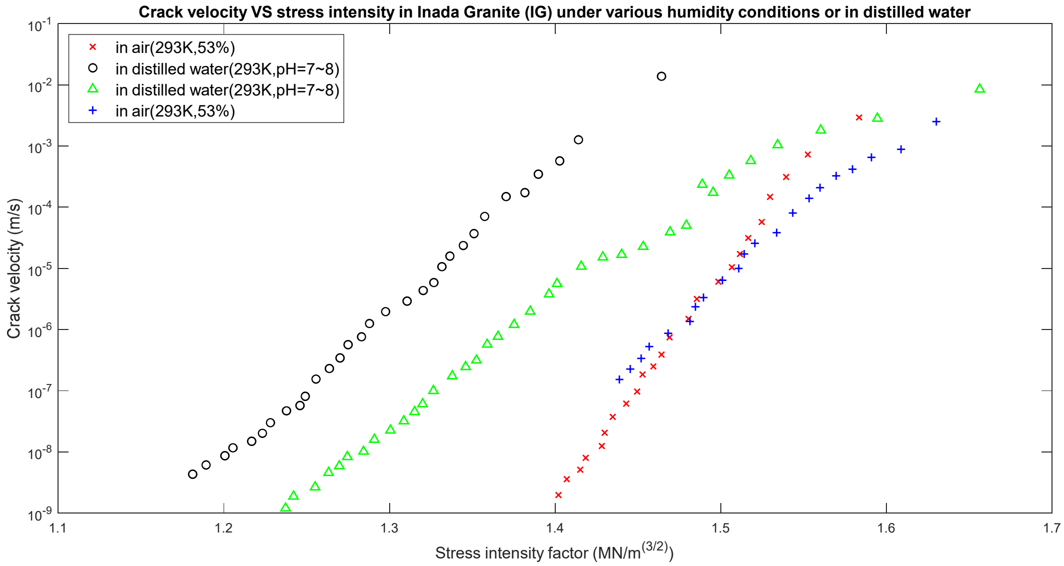

Figure 4.14: Crack velocity versus stress intensity in Inada granite under various humidity conditions or in distilled water at at 293K for four separate experimental datasets [7]

Applying the dimensionless formulas again allows for the identification of two distinct crack growth regimes for each dataset. Figure 4.15 shows the obtained results from this analysis. The dimensionless Inada granite data, covering both air and water environments, further reveals and emphasizes the characteristic dual cracking mode transition - from stable, slow propagation at low dimensionless stress intensities up to -3, to unstable, rapid acceleration beyond this critical thresold. For dimensionless stress intensities below -3, the gradual rise in crack velocity suggests dissipative microfracturing activity occurring ahead of the crack tips. n contrast, at dimensionless stress intensities beyond -3, a significant increase in slope indicates the initiation of uncontrolled cracking, leading to the rapid release of stored elastic strain energy. Additionally, water immersion enhances progression rates within the unstable regime compared to the 53 % air humidity condition likely due to intensified chemical reaction mechanisms. However, the fundamental transition point remains consistent across both environments.

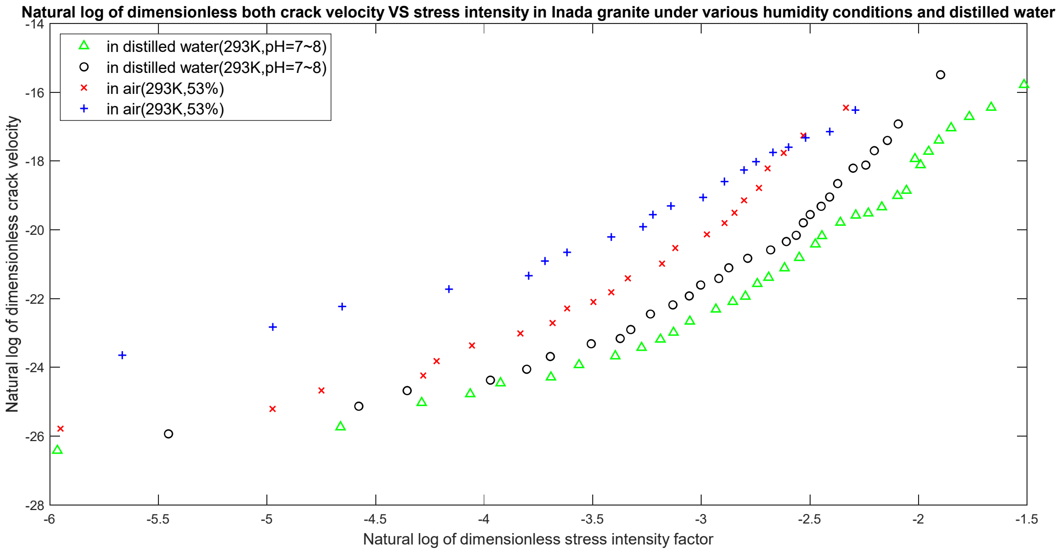

Figure 4.15: Dimensionless crack velocity versus dimensionless stress intensity in Inada granite under various humidity conditions or in distilled water at at 293K for four separate datasets

The obtained slopes, i.e., subcritical crack growth index and intercepts in both slow and fast crack regimes for Inada granite under various humidity conditions or in distilled water at 293K using piecewise curve fitting are summarized in Table 4.7.

Table 4.7: Piecewise curve fitting results of the Inada granite under various humidity conditions or in distilled water at 293K

Data sets	Slope (slow)	Intercept (slow)	Slope (fast)	Intercept (fast)	R^2%
in distilled water (293K,pH=7-8)	1.138	-19.98	4.569	-8.988	99.22
in distilled water (293K,pH=7-8)	1.512	-18.03	5.202	-6.317	98.81
in air (293K, 53 percent)	1.315	-18.28	4.627	-5.969	98.75
in air (293K, 53 percent)	1.255	-16.52	3.093	-9.588	99.71

4.7 Preliminary Analysis of Subcritical Fracture Modes in Rocks

The following observations apply to Nara's crack growth measurements [7], taken in Kumamoto andesite immersed in water, at varying temperature:

Plotting log of relative stress intensity versus log of relative crack growth rate appears to reveal two distinct subcritical crack growth regimes: slow, inter-grain-dominated growth, in which stress concentration of small intergranular cracks remains localized at each small crack, faster, grain-scale cracking in which stress concentration magnitudes and regions of influence of individual cracks both increases, accelerating crack coalescence.

Each regime is described by a distinct power law growth equation. The slow-growth regime is roughly characterized by a linear to quadratic dependence of relative growth rate on relative stress intensity. The fast, grain-scale growth regime is characterized by larger exponents (on the relative stress intensity), ranging from 5.5 to 8. Large exponents appear to reflect predominance of brittle, intergranular cracking, while small exponents may reflect dominance of plastic, intergranular (grain boundary, matrix confined) cracking.

The "elbow" relative stress intensity, i.e., the intersection of the slow and fast growth curves, appears to be defined as determining the threshold stress intensity for initiation of grain-scale cracking. This interpretation, suggested by the apparent fact that fast grain-scale cracking begins at the elbow, is supported by a rough scaling argument showing that experimentally extracted Kth are on the order of ~ 0.1 to $0.2K_C$, consistent with earlier estimates.

Assuming the validity of the interpretation, the grain-scale Kth becomes smaller (to be verified) as water temperature increases. The variation in apparent Kth with temperature is relatively small, however. Both observations are consistent in a way that Kth, to a significant degree, is rock-specific material property.

The observation that fast relative growth exponents are clustered within a relatively narrow range - 5.5 to 8 - over the wide range of water temperatures in Nara's experiments, 284 K - 346 K, appears to be consistent with the interpretation that the fast growth regime corresponds to mechanically-dominated brittle (intergranular) cracking. The slow growth regime might be viewed as defining an "incubation period" -preceding initiation of fast growth - during which the growth of tiny, mechanically isolated, in-matrix cracks is determined by two offsetting features:

a) Small exponents on the relative stress intensity enhance fast growth (since the relative stress intensity is less than one).

b) While small relative stress intensities suppress this enhancement.

Observed variations in rock life-times, combined with the above observation that fast, brittle growth is relatively insensitive to environmental conditions, suggests that the incubation period - during which, environmental and chemical effects are much more prominent - has a major influence on overall rock lifetimes.

4.8 Observation of the Data

Slow or incubation period growth (apparently occurs during every stage of double-torsion stress-relaxation measurements) appears to reflect a mixture of elastic-deformation-induced and plastic-deformation-induced, sub-grain, in-matrix cracking. On the other hand, fast period growth specifically indicates sub-grain cracking induced by plastic deformation within the matrix.

The following notes introduce simple models for two types of cracking that occur within the matrix:one caused by elastic deformation and the other by plastic deformation. Pure elastic-deformation cracking leads to the following relation: $V \propto K_I^2$ Where pure plastic-deformation cracking leads to the following relation: $V \propto K_I$.

The observed slow growth (incubation period) exponents again ranging over $1.1 \leq n_s \leq 2.17$ suggests a mixture of elastic and plastic-deformation, in-matrix, sub-grain-scale cracking.

Slow growth exponents that approach $n_s \rightarrow 2$ indicates elastic-deformation dominated (slow) growth. These, in turn, might provide insight into the relative importance of chemical bond strength of matrix material and chemical composition of matrix material on both elastic and plastic deformation in-matrix fracture.

Slow growth exponents that approach $n_s \to 1$ likewise might serve as an indication of significant bond dissolution/corrosion within the matrix.

CHAPTER 5: CONCLUSIONS AND REMARKS

This dissertation attempts to advance understanding of subcritical fracture processes in rock by introducing novel theoretical and modeling frameworks that allow improved quantitative study and interpretation of grain-scale fracture phenomena. The research is comprised of two distinct, yet complementary parts: a statistical thermodynamics approach for modeling and studying thermally induced microfracture in rock, and application of dimensional analysis to better understand experimentally observed subcritical fracture propagation in rock. Both approaches, which appear to be new in the field of rock fracture, offer valuable insights into the mechanisms driving rock fracture. More importantly, they provide new physics-based, quantitative tools for predicting and interpreting fracture behavior across diverse geological settings.

5.1 Conclusions, Part I

The first part of this work introduces an equilibrium statistical mechanics framework for analyzing thermally induced microfractures in granular rocks. This approach, grounded in energy-based models and macroscopic statistical mechanics, provides a new perspective on the thermal fracture behavior of rocks. The framework:

a) successfully describes the relationship between grain-scale microfracture dynamics and thermal conditions, even in rocks with complex geological histories, and

b) provides theoretical explanations for interpreting widely measured acoustic emission signals obtained during various rock fracture processes.

Key findings, reported here and in a companion publication to be submitted by our research group [3], include the following:

a) Experiments and statistical mechanical modeling reveal the existence of distinct grain boundary fracture mechanisms, each activated in sequential fashion at specific, repeatable temperature thresholds, during thermal loading experiments.

b) Theoretically predicted, temperature-dependent acoustic emission histories well-capture those observed during three different experiments (one reported here, the other two to be reported in [3]).

c) The simple heating and cooling experiment reported here, encompassing several cycles of terrestrial-scale heating and cooling (and again, whose temperature dependent acoustic emission history is well captured by the proposed statistical mechanics model), may provide a useful lab-based analog for studying diurnal, thermally induced fracture of earth surface rock.

d) The results of the analyses detailed here and in [3] provide strong evidence that rock microfracture populations can be treated as history-independent, equilibrium thermodynamic variables. Importantly, this result suggests that field geologists can use readily measured or estimated confining pressures and (say, seasonally averaged) temperatures to estimate microfracture densities - equivalent to rock porosities - for rock anywhere in the world.

e) The results also suggest that similar statistical mechanics=based models can be extended to the study of microfracture in other granular solids.

5.2 Conclusions, Part II

The second part of the dissertation develops a dimensionless modeling approach to analyze grain-scale crack propagation in igneous rocks, subjected to varying stress conditions. By recasting traditional dimensional correlationsâsuch as those in Charles' lawâinto a dimensionless form, the study identified two distinct regimes of subcritical crack growth: a slow growth regime at lower stress intensities, characterized by subcritical crack growth indices (n) ranging between 1.1 and 2.17, and a fast growth regime at higher stress intensities, where n values ranged from 5.5 to 8.

This novel representati,on not only aligns well with the experimental data for different igneous rocks but also facilitates identification of critical thresholds beyond which rapid crack growth and potential failure can occur. The ability to distinguish these propagation modes based on a dimensionless framework offers a powerful tool for assessing rock stability and predicting fracture behavior across various geological environments. By removing dependencies on specific rock properties, this model provides a more generalized understanding of cracking phenomena, potentially aiding in the development of universal models for rock stability, in both terrestrial and extraterrestrial contexts.

The findings presented in this dissertation have several important implications for both scientific understanding and practical applications. The equilibrium statistical mechanics framework and the dimensionless analysis method together provide a more nuanced and physics-based comprehension of grain-scale fracture dynamics in rocks. These approaches are not only valuable for advancing fundamental research but also hold significant potential for practical applications in fields such as civil engineering, geotechnical hazard assessment, and planetary science.

5.3 Future Work

The following items are suggested as potential future extensions of the present work:

1) Further refinement of the models based on additional experimental data, especially under varied environmental conditions, could enhance their predictive accuracy and broaden their applicability to a wider range of rock types and geological settings. Moreover, extending the application of these models to other granular materials that exhibit fracture behavior, such as ceramics and certain types of composite materials, could open up new avenues for interdisciplinary research.

2) Strength estimation in granular rock, based on experimentally estimated subcritical crack growth indices,n, which, for example, take into account climate-dependent fast regime activation on extreme temperature days, should be undertaken.

3) The proposed equilibrium statistical mechanics fracture model should be extended to account for non-equilibrium rock disintegration dynamics. This will involve developing non-equilibrium statistical mechanics models that describe environmentally-induced rock weathering.

REFERENCES

[1] Y. Nara, M. Takada, D. Mori, H. Owada, T. Yoneda, and K. Kaneko, “Subcritical crack growth and long-term strength in rock and cementitious material,” *International Journal of Fracture*, vol. 164, pp. 57–71, 2010.

[2] H. Wang, B. Bonner, S. Carlson, B. Kowallis, and H. Heard, “Thermal stress cracking in granite,” *Journal of Geophysical Research: Solid Earth*, vol. 94, no. B2, pp. 1745–1758, 1989.

[3] R. Keanini, M. Morovati, M. Eppes, M. Rasmussen, U. Shannan, A. Mushkin, A. Sagy, P. Meredith, Y. Nara, P. Baud, M. Heap, L. Griffiths, M. Fichera, and A. Rhinehart, “Equilibrium and nonequilibrium statistical mechanics in rock: estimating history-independent thermal microfracture, diagnosing simultaneous microfracture processes, and connections to rock weathering,” *J. Geophys. Res. Solid Earth, submitted*, 2024.

[4] L. Griffiths, O. Lengliné, M. Heap, P. Baud, and J. Schmittbuhl, “Thermal cracking in westerly granite monitored using direct wave velocity, coda wave interferometry, and acoustic emissions,” *Journal of Geophysical Research: Solid Earth*, vol. 123, no. 3, pp. 2246–2261, 2018.

[5] M. Eppes, L. Griffiths, M. Heap, R. Keanini, and P. Baud, “Experimentally reproducing thermal breakdown of rock at earth’s surface,” in *AGU Fall Meeting Abstracts*, vol. 2016, pp. EP43C–0967, 2016.

[6] Y. A. Cengel, M. A. Boles, and M. Kanoğlu, *Thermodynamics: an engineering approach*, vol. 5. McGraw-hill New York, 2011.

[7] Y. Nara, H. Yamanaka, Y. Oe, and K. Kaneko, “Influence of temperature and water on subcritical crack growth parameters and long-term strength for igneous rocks,” *Geophysical Journal International*, vol. 193, no. 1, pp. 47–60, 2013.

[8] B. K. Atkinson and P. G. Meredith, “Experinmental fracture nmechanics data for rocks and nminerals,” *Fracture mechanics of rock*, p. 477, 1987.

[9] B. K. Atkinson, “Introduction to fracture mechanics and its geophysical applications,” *Fracture mechanics of rock*, pp. 1–26, 1987.

[10] A. R. Ingraffea, “Theory of crack initiation and propagation in rock,” *Fracture mechanics of rock*, vol. 10, pp. 93–94, 1987.

[11] B. K. Atkinson and P. G. Meredith, “The theory of subcritical crack growth with applications to minerals and rocks,” *Fracture mechanics of rock*, vol. 2, pp. 111–166, 1987.

[12] T. Hales and J. J. Roering, “Climatic controls on frost cracking and implications for the evolution of bedrock landscapes,” *Journal of Geophysical Research: Earth Surface*, vol. 112, no. F2, 2007.

[13] B. A. Clarke and D. W. Burbank, “Bedrock fracturing, threshold hillslopes, and limits to the magnitude of bedrock landslides,” *Earth and Planetary Science Letters*, vol. 297, no. 3-4, pp. 577–586, 2010.

[14] D. N. Scott and E. E. Wohl, “Bedrock fracture influences on geomorphic process and form across process domains and scales,” *Earth Surface Processes and Landforms*, vol. 44, no. 1, pp. 27–45, 2019.

[15] N. Cook, “Seismicity associated with mining,” *Engineering Geology*, vol. 10, no. 2-4, pp. 99–122, 1976.

[16] L. House, “Locating microearthquakes induced by hydraulic fracturing in crystalline rock,” *Geophysical Research Letters*, vol. 14, no. 9, pp. 919–921, 1987.

[17] P. G. Meredith, I. G. Main, and C. Jones, “Temporal variations in seismicity during quasi-static and dynamic rock failure,” *Tectonophysics*, vol. 175, no. 1-3, pp. 249–268, 1990.

[18] J. D. Marshall, “Climatic and oceanographic isotopic signals from the carbonate rock record and their preservation,” *Geological magazine*, vol. 129, no. 2, pp. 143–160, 1992.

[19] S. Gruber and W. Haeberli, “Permafrost in steep bedrock slopes and its temperature-related destabilization following climate change,” *Journal of Geophysical Research: Earth Surface*, vol. 112, no. F2, 2007.

[20] M.-C. Eppes and R. Keanini, “Mechanical weathering and rock erosion by climate-dependent subcritical cracking,” *Reviews of Geophysics*, vol. 55, no. 2, pp. 470–508, 2017.

[21] N. Liu, N. Li, S. Wang, G. Li, and Z. Song, “A fully coupled thermo-hydro-mechanical model for fractured rock masses in cold regions,” *Cold Regions Science and Technology*, vol. 205, p. 103707, 2023.

[22] K. Hall, “The role of thermal stress fatigue in the breakdown of rock in cold regions,” *Geomorphology*, vol. 31, no. 1-4, pp. 47–63, 1999.

[23] H. J. Gage, C. H. Eyles, and A. L. Peace, “Winter weathering of fractured sedimentary rocks in a temperate climate: observation of freeze–thaw and thermal processes on the niagara escarpment, hamilton, ontario,” *Geological Magazine*, vol. 159, no. 11-12, pp. 2060–2081, 2022.

[24] M. C. Eppes, B. Magi, B. Hallet, E. Delmelle, P. Mackenzie-Helnwein, K. Warren, and S. Swami, “Deciphering the role of solar-induced thermal stresses in rock weathering,” *Bulletin*, vol. 128, no. 9-10, pp. 1315–1338, 2016.

[25] P. Sumner, W. Nel, and D. Hedding, “Thermal attributes of rock weathering: zonal or azonal? a comparison of rock temperatures in different environments,” *Polar Geography*, vol. 28, no. 2, pp. 79–92, 2004.

[26] J. Walder and B. Hallet, “A theoretical model of the fracture of rock during freezing,” *Geological Society of America Bulletin*, vol. 96, no. 3, pp. 336–346, 1985.

[27] M. Alneasan and A. K. Alzo’ubi, “Comprehensive investigation of rock fracture behaviour in clay-rich rocks under the effect of temperature: Experimental study under three loading modes (i, i/ii, ii),” *Engineering Fracture Mechanics*, vol. 276, p. 108933, 2022.

[28] M. Krautblatter, D. Funk, and F. K. Günzel, “Why permafrost rocks become unstable: a rock–ice-mechanical model in time and space,” *Earth Surface Processes and Landforms*, vol. 38, no. 8, pp. 876–887, 2013.

[29] K. Warren, M.-C. Eppes, S. Swami, J. Garbini, and J. Putkonen, “Automated field detection of rock fracturing, microclimate, and diurnal rock temperature and strain fields,” *Geoscientific Instrumentation, Methods and Data Systems*, vol. 2, no. 2, pp. 275–288, 2013.

[30] M.-E. M. Akara, D. M. Reeves, M. D.-T. Gnazou, and G. Boguido, “Assessing future climate trends and their impact on different fractured rock aquifers in northern togo,” *Journal of Water and Climate Change*, vol. 13, no. 11, pp. 4019–4038, 2022.

[31] J. B. Murton, R. Peterson, and J.-C. Ozouf, “Bedrock fracture by ice segregation in cold regions,” *Science*, vol. 314, no. 5802, pp. 1127–1129, 2006.

[32] Y. Han, H. Jia, T. Wang, L. Wang, Q. Li, and Y. Wang, “Fracture toughness and cracking behavior of frozen sandstone at different freezing temperatures,” *Engineering Fracture Mechanics*, vol. 271, p. 108664, 2022.

[33] Y. Nara, M. Takada, T. Igarashi, N. Hiroyoshi, and K. Kaneko, “Subcritical crack growth in rocks in an aqueous environment,” *Exploration Geophysics*, vol. 40, no. 1, pp. 163–171, 2009.

[34] Y. Nara, R. Nakabayashi, M. Maruyama, N. Hiroyoshi, T. Yoneda, and K. Kaneko, “Influences of electrolyte concentration on subcritical crack growth in sandstone in water,” *Engineering Geology*, vol. 179, pp. 41–49, 2014.

[35] Y. Nara, K. Kashiwaya, Y. Nishida, and T. Ii, “Influence of surrounding environment on subcritical crack growth in marble,” *Tectonophysics*, vol. 706, pp. 116–128, 2017.

[36] C. Ping, J.-T. Li, and H.-P. Yuan, "Testing study of subcritical crack growth rate and fracture toughness in different rocks," *Transactions of Nonferrous Metals Society of China*, vol. 16, no. 3, pp. 709–713, 2006.

[37] J. Ma, D. Li, P. Luo, Q. Zhu, C. Zhang, and X. Su, "Subcritical crack growth and fracture behavior of rocks and long-term strength estimation," *Theoretical and Applied Fracture Mechanics*, vol. 122, p. 103664, 2022.

[38] Y. Nara, T. Harui, and K. Kashiwaya, "Influence of calcium ions on subcritical crack growth in granite," *International Journal of Rock Mechanics and Mining Sciences*, vol. 102, pp. 71–77, 2018.

[39] K. Sadananda, M. N. Babu, and A. Vasudevan, "The unified approach to subcritical crack growth and fracture," *Engineering Fracture Mechanics*, vol. 212, pp. 238–257, 2019.

[40] S. Ji, Z. Wang, and J. Karlovšek, "Analytical study of subcritical crack growth under mode i loading to estimate the roof durability in underground excavation," *International Journal of Mining Science and Technology*, vol. 32, no. 2, pp. 375–385, 2022.

[41] Y. Nara and K. Kaneko, "Sub-critical crack growth in anisotropic rock," *International Journal of Rock Mechanics and Mining Sciences*, vol. 43, no. 3, pp. 437–453, 2006.

[42] Y. Nara and K. Kaneko, "Study of subcritical crack growth in andesite using the double torsion test," *International Journal of Rock Mechanics and Mining Sciences*, vol. 42, no. 4, pp. 521–530, 2005.

[43] T. Y. Ko and J. Kemeny, "Determination of the subcritical crack growth parameters in rocks using the constant stress-rate test," *International Journal of Rock Mechanics and Mining Sciences*, vol. 59, pp. 166–178, 2013.

[44] R. H. Wong and K. Chau, "Effect of cyclic heating on subcritical crack growth of rock beams under four-point bending test," *International Journal of Rock Mechanics and Mining Sciences*, vol. 138, p. 104553, 2021.

[45] J. Ma, D. Li, S. Du, Z. Han, P. Luo, and J. Zhao, "Comparison of subcritical crack growth and dynamic fracture propagation in rocks under double-torsion tests," *International Journal of Rock Mechanics and Mining Sciences*, vol. 170, p. 105481, 2023.

[46] T. Meng, Y. Yue, J. Ma, B. Jiao, H. Niu, L. Wen, and X. Yongbin, "Use of dc voltage fluctuation method to investigate real-time mode i and mode ii subcritical crack growth behavior in gypsum rock," *Engineering Fracture Mechanics*, vol. 234, p. 107104, 2020.

[47] Y. Mahmutoglu, "Mechanical behaviour of cyclically heated fine grained rock," *Rock Mechanics and Rock Engineering*, vol. 31, no. 3, pp. 169–179, 1998.

[48] M. Takarli, W. Prince, and R. Siddique, “Damage in granite under heating/cooling cycles and water freeze–thaw condition,” *International Journal of Rock Mechanics and Mining Sciences*, vol. 45, no. 7, pp. 1164–1175, 2008.

[49] J. Rutqvist, B. Freifeld, K.-B. Min, D. Elsworth, and Y. Tsang, “Analysis of thermally induced changes in fractured rock permeability during 8 years of heating and cooling at the yucca mountain drift scale test,” *International Journal of Rock Mechanics and Mining Sciences*, vol. 45, no. 8, pp. 1373–1389, 2008.

[50] B. Johnson, A. Gangi, and J. Handin, “Thermal cracking of rock subjected to slow, uniform temperature changes,” in *ARMA US Rock Mechanics/Geomechanics Symposium*, pp. ARMA–78, ARMA, 1978.

[51] P. Meredith, A. Daoud, J. Browning, and T. Mitchell, “Microstructural controls on thermal crack damage during temperature-cycling experiments on volcanic rocks.,” in *Geophysical Research Abstracts*, vol. 21, 2019.

[52] T.-B. Yin, D.-D. Zhuang, M.-J. Li, and X.-B. Li, “Numerical simulation study on the thermal stress evolution and thermal cracking law of granite under heat conduction,” *Computers and Geotechnics*, vol. 148, p. 104813, 2022.

[53] X. Wu, Q. Guo, Y. Zhu, F. Ren, J. Zhang, X. Wu, and M. Cai, “Pore structure and crack characteristics in high-temperature granite under water-cooling,” *Case Studies in Thermal Engineering*, vol. 28, p. 101646, 2021.

[54] Z. Ge and Q. Sun, “Acoustic emission (ae) characteristics of granite after heating and cooling cycles,” *Engineering Fracture Mechanics*, vol. 200, pp. 418–429, 2018.

[55] Q. Wu, L. Weng, Y. Zhao, B. Guo, and T. Luo, “On the tensile mechanical characteristics of fine-grained granite after heating/cooling treatments with different cooling rates,” *Engineering Geology*, vol. 253, pp. 94–110, 2019.

[56] F. Kang, T. Jia, Y. Li, J. Deng, X. Huang, *et al.*, “Experimental study on the physical and mechanical variations of hot granite under different cooling treatments,” *Renewable Energy*, vol. 179, pp. 1316–1328, 2021.

[57] M. Du, F. Gao, C. Cai, S. Su, and Z. Wang, “Study on the surface crack propagation mechanism of coal and sandstone subjected to cryogenic cooling with liquid nitrogen,” *Journal of Natural Gas Science and Engineering*, vol. 81, p. 103436, 2020.

[58] X. Li, L. You, Y. Kang, J. Liu, M. Chen, T. Zeng, and Z. Hao, “Investigation on the thermal cracking of shale under different cooling modes,” *Journal of Natural Gas Science and Engineering*, vol. 97, p. 104359, 2022.

[59] P.-Z. Pan and C.-Y. Shao, “Experimental studies on the physical and mechanical properties of heated rock by air, water and high-viscosity fluid cooling,” *Geomechanics for Energy and the Environment*, vol. 31, p. 100315, 2022.

[60] B. L. A. Isaka, R. P. Gamage, T. D. Rathnaweera, M. S. A. Perera, D. Chandrasekharam, and W. G. P. Kumari, “An influence of thermally-induced microcracking under cooling treatments: mechanical characteristics of australian granite,” *Energies*, vol. 11, no. 6, p. 1338, 2018.

[61] Y.-J. Shen, X. Hou, J.-Q. Yuan, and C.-H. Zhao, “Experimental study on temperature change and crack expansion of high temperature granite under different cooling shock treatments,” *Energies*, vol. 12, no. 11, p. 2097, 2019.

[62] J. Browning, P. Meredith, and A. Gudmundsson, “Cooling-dominated cracking in thermally stressed volcanic rocks,” *Geophysical Research Letters*, vol. 43, no. 16, pp. 8417–8425, 2016.

[63] A. Daoud, J. Browning, P. G. Meredith, and T. M. Mitchell, “Microstructural controls on thermal crack damage and the presence of a temperature-memory effect during cyclic thermal stressing of rocks,” *Geophysical Research Letters*, vol. 47, no. 19, p. e2020GL088693, 2020.

[64] W. Zhang, W. Li, X. Zhang, W. Qiao, Y. Wang, and J. Xie, “Study on thermal crack characteristics of granite in shandong province, china under different temperatures and heating/cooling treatments,” 2023.

[65] D. Zhu, H. Jing, Q. Yin, and G. Han, “Experimental study on the damage of granite by acoustic emission after cyclic heating and cooling with circulating water,” *Processes*, vol. 6, no. 8, p. 101, 2018.

[66] K. Kim, J. Kemeny, and M. Nickerson, “Effect of rapid thermal cooling on mechanical rock properties,” *Rock mechanics and rock engineering*, vol. 47, pp. 2005–2019, 2014.

[67] X. Wu, Z. Huang, H. Song, S. Zhang, Z. Cheng, R. Li, H. Wen, P. Huang, and X. Dai, “Variations of physical and mechanical properties of heated granite after rapid cooling with liquid nitrogen,” *Rock Mechanics and Rock Engineering*, vol. 52, pp. 2123–2139, 2019.

[68] G. Rong, S. Sha, B. Li, Z. Chen, and Z. Zhang, “Experimental investigation on physical and mechanical properties of granite subjected to cyclic heating and liquid nitrogen cooling,” *Rock Mechanics and Rock Engineering*, vol. 54, pp. 2383–2403, 2021.

[69] F. Wang and H. Konietzky, “Thermal cracking in granite during a heating–cooling cycle up to 1000Â° c: Laboratory testing and real-time simulation,” *Rock Mechanics and Rock Engineering*, pp. 1–18, 2022.

[70] Y.-j. Shen, J.-s. Hao, X. Hou, J.-q. Yuan, and Z.-p. Bai, “Crack propagation in high-temperature granite after cooling shock: experiment and numerical simulation,” *Bulletin of Engineering Geology and the Environment*, vol. 80, no. 7, pp. 5831–5844, 2021.

[71] T. Yin, Q. Li, and X. Li, “Experimental investigation on mode i fracture characteristics of granite after cyclic heating and cooling treatments,” *Engineering Fracture Mechanics*, vol. 222, p. 106740, 2019.

[72] D. Li, X. Su, F. Gao, and Z. Liu, “Experimental studies on physical and mechanical behaviors of heated rocks with pre-fabricated hole exposed to different cooling rates,” *Geomechanics and Geophysics for Geo-Energy and Geo-Resources*, vol. 8, no. 4, p. 125, 2022.

[73] Y. Nara, N. Hiroyoshi, T. Yoneda, and K. Kaneko, “Effects of relative humidity and temperature on subcritical crack growth in igneous rock,” *International Journal of Rock Mechanics and Mining Sciences*, vol. 47, no. 4, pp. 640–646, 2010.

[74] K. Andersson, M. Nyberg, H. Ogasawara, D. Nordlund, T. Kendelewicz, C. Doyle, G. Brown Jr, L. Pettersson, and A. Nilsson, “Experimental and theoretical characterization of the structure of defects at the pyrite fes 2 (100) surface,” *Physical Review B*, vol. 70, no. 19, p. 195404, 2004.

[75] S.-H. Chang and C.-I. Lee, “Estimation of cracking and damage mechanisms in rock under triaxial compression by moment tensor analysis of acoustic emission,” *International Journal of Rock Mechanics and Mining Sciences*, vol. 41, no. 7, pp. 1069–1086, 2004.

[76] T. Chichinina, I. Obolentseva, and G. Ronquillo-Jarillo, “Anisotropy of seismic attenuation in fractured media: Theory and ultrasonic experiment,” *Transport in Porous Media*, vol. 79, pp. 1–14, 2009.

[77] L. Vernik and A. Nur, “Ultrasonic velocity and anisotropy of hydrocarbon source rocks,” *Geophysics*, vol. 57, no. 5, pp. 727–735, 1992.

[78] M. Möllhoff, C. Bean, and P. Meredith, “Rock fracture compliance derived from time delays of elastic waves,” *Geophysical Prospecting*, vol. 58, no. 6, pp. 1111–1122, 2010.

[79] G. Fair, M. Shemkunas, W. T. Petuskey, and S. Sambasivan, “Layered perovskites as âsoft-ceramicsâ,” *Journal of the European Ceramic Society*, vol. 19, no. 13-14, pp. 2437–2447, 1999.

[80] D. L. Goldsby, A. Rar, G. M. Pharr, and T. E. Tullis, “Nanoindentation creep of quartz, with implications for rate-and state-variable friction laws relevant to earthquake mechanics,” *Journal of materials research*, vol. 19, no. 1, pp. 357–365, 2004.

[81] Z. Haifeng, C. Mian, J. Yan, D. Yunhong, and W. Yonghui, “Rock fracture kinetics of the facture mesh system in shale gas reservoirs,” *Petroleum exploration and development*, vol. 39, no. 4, pp. 498–503, 2012.

[82] M. He, J. Miao, and J. Feng, “Rock burst process of limestone and its acoustic emission characteristics under true-triaxial unloading conditions,” *International Journal of Rock Mechanics and Mining Sciences*, vol. 47, no. 2, pp. 286–298, 2010.

[83] T. Kendelewicz, C. Doyle, B. Bostick, and G. Brown Jr, “Initial oxidation of fractured surfaces of fes2 (100) by molecular oxygen, water vapor, and air,” *Surface science*, vol. 558, no. 1-3, pp. 80–88, 2004.

[84] B. Dverstorp, J. Andersson, and W. Nordqvist, “Discrete fracture network interpretation of field tracer migration in sparsely fractured rock,” *Water Resources Research*, vol. 28, no. 9, pp. 2327–2343, 1992.

[85] A. Sagy, Z. Reches, and I. Roman, “Dynamic fracturing: Field and experimental observations,” *Journal of Structural Geology*, vol. 23, no. 8, pp. 1223–1239, 2001.

[86] F. A. Pacheco and A. M. Alencoão, “Role of fractures in weathering of solid rocks: narrowing the gap between laboratory and field weathering rates,” *Journal of Hydrology*, vol. 316, no. 1-4, pp. 248–265, 2006.

[87] E. A. Hasenmueller, X. Gu, J. N. Weitzman, T. S. Adams, G. E. Stinchcomb, D. M. Eissenstat, P. J. Drohan, S. L. Brantley, and J. P. Kaye, “Weathering of rock to regolith: The activity of deep roots in bedrock fractures,” *Geoderma*, vol. 300, pp. 11–31, 2017.

[88] M. I. Lebedeva and S. L. Brantley, “Weathering and erosion of fractured bedrock systems,” *Earth Surface Processes and Landforms*, vol. 42, no. 13, pp. 2090–2108, 2017.

[89] S. Cuccuru, L. Casini, G. Oggiano, and G. P. Cherchi, “Can weathering improve the toughness of a fractured rock? a case study using the san giacomo granite,” *Bulletin of Engineering Geology and the Environment*, vol. 71, pp. 557–567, 2012.

[90] A. Røyne, B. Jamtveit, J. Mathiesen, and A. Malthe-Sørenssen, “Controls on rock weathering rates by reaction-induced hierarchical fracturing,” *Earth and Planetary Science Letters*, vol. 275, no. 3-4, pp. 364–369, 2008.

[91] K. Zhang, Z. Wang, Y. Jiang, A. Wang, B. Xiang, N. Zhou, and Y. Wang, “Effects of weathering and fracturing on the physical properties of different types of volcanic rock: Implications for oil reservoirs of the zhongguai relief, junggar basin, nw china,” *Journal of Petroleum Science and Engineering*, vol. 193, p. 107351, 2020.

[92] K. Hall and M.-F. André, “New insights into rock weathering from high-frequency rock temperature data: an antarctic study of weathering by thermal stress,” *Geomorphology*, vol. 41, no. 1, pp. 23–35, 2001.

[93] J. Ehlen, "Fracture characteristics in weathered granites," *Geomorphology*, vol. 31, no. 1-4, pp. 29–45, 1999.

[94] M. C. Eppes, L. D. McFadden, K. W. Wegmann, and L. A. Scuderi, "Cracks in desert pavement rocks: Further insights into mechanical weathering by directional insolation," *Geomorphology*, vol. 123, no. 1-2, pp. 97–108, 2010.

[95] J.-C. Maréchal, B. Dewandel, and K. Subrahmanyam, "Use of hydraulic tests at different scales to characterize fracture network properties in the weathered-fractured layer of a hard rock aquifer," *Water resources research*, vol. 40, no. 11, 2004.

[96] J. Aldred, M. C. Eppes, K. Aquino, R. Deal, J. Garbini, S. Swami, A. Tuttle, and G. Xanthos, "The influence of solar-induced thermal stresses on the mechanical weathering of rocks in humid mid-latitudes," *Earth Surface Processes and Landforms*, vol. 41, no. 5, pp. 603–614, 2016.

[97] P. Segall and D. D. Pollard, "Joint formation in granitic rock of the sierra nevada," *Geological Society of America Bulletin*, vol. 94, no. 5, pp. 563–575, 1983.

[98] E. Zhao, J. Li, X. Zhang, C. Zhang, Q. Ren, T. Tan, and Y. Wang, "Failure characteristics and the law of the energy evolution of granite with different pre-crack inclination angles under uniaxial compression loading," *Frontiers in Earth Science*, vol. 11, p. 1218178, 2023.

[99] Z. Yan, F. Dai, Y. Liu, and H. Du, "Experimental investigations of the dynamic mechanical properties and fracturing behavior of cracked rocks under dynamic loading," *Bulletin of Engineering Geology and the Environment*, vol. 79, pp. 5535–5552, 2020.

[100] J. Qi, L. Zhou, H. Zhang, J. Chen, L. Ma, and T. Shi, "Research on crack evolution law and mechanical analysis of three cracked rock masses subjected to compression load," *Theoretical and Applied Fracture Mechanics*, vol. 127, p. 104035, 2023.

[101] Y. Song, H. Hu, and B. Han, "Seismic attenuation and dispersion in a cracked porous medium: An effective medium model based on poroelastic linear slip conditions," *Mechanics of Materials*, vol. 140, p. 103229, 2020.

[102] S. Bastola and M. Cai, "Investigation of mechanical properties and crack propagation in pre-cracked marbles using lattice-spring-based synthetic rock mass (ls-srm) modeling approach," *Computers and Geotechnics*, vol. 110, pp. 28–43, 2019.

[103] S. Zafar, A. Hedayat, and O. Moradian, "Micromechanics of fracture propagation during multistage stress relaxation and creep in brittle rocks," *Rock Mechanics and Rock Engineering*, vol. 55, no. 12, pp. 7611–7627, 2022.

[104] S. Zafar, A. Hedayat, and O. Moradian, “Laboratory investigation of stress relaxation in brittle rocks using acoustic emission and digital image correlation,” in *ARMA US Rock Mechanics/Geomechanics Symposium*, pp. ARMA–2021, ARMA, 2021.

[105] M. Rinne *et al.*, *Fracture mechanics and subcritical crack growth approach to model time-dependent failure in brittle rock.* Teknillinen korkeakoulu, 2008.

[106] S. Zafar, A. Hedayat, and O. Moradian, “Energy partitioning during fracturing in granite under stress relaxation,” in *ARMA US Rock Mechanics/Geomechanics Symposium*, pp. ARMA–2022, ARMA, 2022.

[107] J. Liu, H. Yang, Y. Xiao, and X. Zhou, “Macro-mesoscopic fracture and strength character of pre-cracked granite under stress relaxation condition,” *Rock Mechanics and Rock Engineering*, vol. 51, pp. 1401–1412, 2018.

[108] H. Yang, J. Liu, and X. Zhou, “Effects of the loading and unloading conditions on the stress relaxation behavior of pre-cracked granite,” *Rock Mechanics and Rock Engineering*, vol. 50, pp. 1157–1169, 2017.

[109] J. XU, X.-z. SONG, S.-j. PENG, C.-c. CHEN, X.-m. RAN, and F.-z. YAN, “Experimental study of generalized stress relaxation of rock based on 3d-dic technology,” *Rock and Soil Mechanics*, vol. 42, no. 1, p. 2, 2021.

[110] C. Paraskevopoulou, M. Perras, M. Diederichs, F. Amann, S. Löw, T. Lam, and M. Jensen, “The three stages of stress relaxation-observations for the time-dependent behaviour of brittle rocks based on laboratory testing,” *Engineering Geology*, vol. 216, pp. 56–75, 2017.

[111] Z. Zhong, R. Deng, L. Lv, X. Fu, and J. Yu, “Fracture mechanism of naturally cracked rock around an inverted u-shaped opening in a biaxial compression test,” *International Journal of Rock Mechanics and Mining Sciences*, vol. 103, pp. 242–253, 2018.

[112] B. K. Atkinson, “Subcritical crack propagation in rocks: theory, experimental results and applications,” *Journal of Structural Geology*, vol. 4, no. 1, pp. 41–56, 1982.

[113] M. J. Lato, M. S. Diederichs, and D. J. Hutchinson, “Bias correction for view-limited lidar scanning of rock outcrops for structural characterization,” *Rock mechanics and rock engineering*, vol. 43, pp. 615–628, 2010.

[114] I. Voyat, R. Roncella, G. Forlani, and A. M. Ferrero, “Advanced techniques for geo structural surveys in modelling fractured rock masses: application to two alpine sites,” in *ARMA US Rock Mechanics/Geomechanics Symposium*, pp. ARMA–06, ARMA, 2006.

[115] W. Song, T. W. de Haas, H. Fadaei, and D. Sinton, “Chip-off-the-old-rock: the study of reservoir-relevant geological processes with real-rock micromodels,” *Lab on a Chip*, vol. 14, no. 22, pp. 4382–4390, 2014.

[116] Y. Wang, J. Jiang, J. Darkwa, Z. Xu, X. Zheng, and G. Zhou, “Experimental study of thermal fracturing of hot dry rock irradiated by moving laser beam: Temperature, efficiency and porosity,” *Renewable Energy*, vol. 160, pp. 803–816, 2020.

[117] X.-P. Zhou, G.-Q. Li, and H.-C. Ma, “Real-time experiment investigations on the coupled thermomechanical and cracking behaviors in granite containing three pre-existing fissures,” *Engineering Fracture Mechanics*, vol. 224, p. 106797, 2020.

[118] D. Yang, M. Bornert, S. Chanchole, H. Gharbi, P. Valli, and B. Gatmiri, “Dependence of elastic properties of argillaceous rocks on moisture content investigated with optical full-field strain measurement techniques,” *International Journal of Rock Mechanics and Mining Sciences*, vol. 53, pp. 45–55, 2012.

[119] W. Kumari, P. Ranjith, M. Perera, and B. Chen, “Experimental investigation of quenching effect on mechanical, microstructural and flow characteristics of reservoir rocks: Thermal stimulation method for geothermal energy extraction,” *Journal of Petroleum Science and Engineering*, vol. 162, pp. 419–433, 2018.

[120] K. Wang, K. G. Taylor, and L. Ma, “Advancing the application of atomic force microscopy (afm) to the characterization and quantification of geological material properties,” *International Journal of Coal Geology*, vol. 247, p. 103852, 2021.

[121] L. M. Otter, M. W. Förster, E. Belousova, P. OâReilly, D. Nowak, S. Park, S. Clark, S. F. Foley, and D. E. Jacob, “Nanoscale chemical imaging by photo-induced force microscopy: technical aspects and application to the geosciences,” *Geostandards and Geoanalytical Research*, vol. 45, no. 1, pp. 5–27, 2021.

[122] A. Jahanbakhsh, K. L. Wlodarczyk, D. P. Hand, R. R. Maier, and M. M. Maroto-Valer, “Review of microfluidic devices and imaging techniques for fluid flow study in porous geomaterials,” *Sensors*, vol. 20, no. 14, p. 4030, 2020.

[123] H. S. Viswanathan, J. Ajo-Franklin, J. T. Birkholzer, J. W. Carey, Y. Guglielmi, J. Hyman, S. Karra, L. Pyrak-Nolte, H. Rajaram, G. Srinivasan, *et al.*, “From fluid flow to coupled processes in fractured rock: Recent advances and new frontiers,” *Reviews of Geophysics*, vol. 60, no. 1, p. e2021RG000744, 2022.

[124] A. Gucsik, C. Koeberl, F. Brandstätter, E. Libowitzky, and W. U. Reimold, “Scanning electron microscopy, cathodoluminescence, and raman spectroscopy of experimentally shock-metamorphosed quartzite,” *Meteoritics & Planetary Science*, vol. 38, no. 8, pp. 1187–1197, 2003.

[125] S. J. B. Reed, *Electron microprobe analysis and scanning electron microscopy in geology.* Cambridge university press, 2005.

[126] M. Lubczynski and J. Roy, “Hydrogeological interpretation and potential of the new magnetic resonance sounding (mrs) method,” *Journal of Hydrology*, vol. 283, no. 1-4, pp. 19–40, 2003.

[127] R. Mota, F. M. Santos, A. Mateus, F. Marques, M. Gonçalves, J. Figueiras, and H. Amaral, “Granite fracturing and incipient pollution beneath a recent landfill facility as detected by geoelectrical surveys,” *Journal of Applied Geophysics*, vol. 57, no. 1, pp. 11–22, 2004.

[128] D. H. Rothman, “Nonlinear inversion, statistical mechanics, and residual statics estimation,” *Geophysics*, vol. 50, no. 12, pp. 2784–2796, 1985.

[129] A. Bashkirov and A. Vityazev, “Statistical mechanics of fragmentation processes of ice and rock bodies,” *Planetary and space science*, vol. 44, no. 9, pp. 909–915, 1996.

[130] E. G. Daub and J. M. Carlson, “Friction, fracture, and earthquakes,” *Annu. Rev. Condens. Matter Phys.*, vol. 1, no. 1, pp. 397–418, 2010.

[131] H. Kawamura, T. Hatano, N. Kato, S. Biswas, and B. K. Chakrabarti, “Statistical physics of fracture, friction, and earthquakes,” *Reviews of Modern Physics*, vol. 84, no. 2, p. 839, 2012.

[132] L. Xue, M. Qi, S. Qin, G. Li, P. Li, and M. Wang, “A potential strain indicator for brittle failure prediction of low-porosity rock: part iiâtheoretical studies based on renormalization group theory,” *Rock Mechanics and Rock Engineering*, vol. 48, pp. 1773–1785, 2015.

[133] F. Wu, J. Wu, H. Bao, B. Li, Z. Shan, and D. Kong, “Advances in statistical mechanics of rock masses and its engineering applications,” *Journal of Rock Mechanics and Geotechnical Engineering*, vol. 13, no. 1, pp. 22–45, 2021.

[134] F. Wu, J. Wu, H. Bao, Z. Bai, L. Qiao, F. Zhang, B. Li, F. Si, L. Yu, S. Guan, *et al.*, “Rapid intelligent evaluation method and technology for determining engineering rock mass quality,” *Rock Mechanics Bulletin*, p. 100038, 2023.

[135] R. Bermejo, P. Supancic, C. Krautgasser, R. Morrell, and R. Danzer, “Subcritical crack growth in low temperature co-fired ceramics under biaxial loading,” *Engineering Fracture Mechanics*, vol. 100, pp. 108–121, 2013.

[136] S. Grutzik, K. Strong, and J. Rimsza, “Kinetic model for prediction of subcritical crack growth, crack tip relaxation, and static fatigue threshold in silicate glass,” *Journal of Non-Crystalline Solids: X*, vol. 16, p. 100134, 2022.

[137] S. Mazerat and R. Pailler, "Effect of microstructure and chemical composition on subcritical crack growth in sic-based fiber tows," *Ceramics International*, vol. 47, no. 2, pp. 2888–2891, 2021.

[138] A. Hizebry, M. Saâdaoui, H. Elattaoui, J. Chevalier, and G. Fantozzi, "R-curve and subcritical crack growth in lead zirconate titanate ceramics," *Materials Science and Engineering: A*, vol. 499, no. 1-2, pp. 368–373, 2009.

[139] B. Kumar and S. Ray, "Nano-mechanics based crack growth characterization of concrete under fatigue loading," *Procedia Structural Integrity*, vol. 39, pp. 222–228, 2022.

[140] C. Krautgasser, R. Danzer, M. Deluca, P. Supancic, F. Aldrian, and R. Bermejo, "Subcritical crack growth in multilayer low temperature co-fired ceramics designed with surface compressive stresses," *Journal of the European Ceramic Society*, vol. 36, no. 16, pp. 4095–4105, 2016.

[141] R. Belli, J. I. Zorzin, A. Petschelt, U. Lohbauer, and G. T. Rocca, "Crack growth behavior of a biomedical polymer-ceramic interpenetrating scaffolds composite in the subcritical regimen," *Engineering Fracture Mechanics*, vol. 231, p. 107014, 2020.

[142] J. W. Gibbs, *Elementary principles in statistical mechanics: developed with especial reference to the rational foundations of thermodynamics*. C. Scribner's sons, 1902.

[143] K. Marquardt and U. H. Faul, "The structure and composition of olivine grain boundaries: 40 years of studies, status and current developments," *Physics and Chemistry of Minerals*, vol. 45, no. 2, pp. 139–172, 2018.

[144] T. L. Anderson, *Fracture mechanics: fundamentals and applications*. CRC press, 2017.

[145] P. J. Frings and H. L. Buss, "The central role of weathering in the geosciences," *Elements: An International Magazine of Mineralogy, Geochemistry, and Petrology*, vol. 15, no. 4, pp. 229–234, 2019.

[146] Q. Zhou, Z. Zhu, R. Zhang, Z. Fan, X. Nie, W. Gao, C. Li, J. Wang, and L. Ren, "Rock fracture initiation under deep extreme in situ conditions: A review," *Journal of Rock Mechanics and Geotechnical Engineering*, 2024.

[147] X. Wang, F. Chen, E. Hasi, and J. Li, "Desertification in china: an assessment," *Earth-Science Reviews*, vol. 88, no. 3-4, pp. 188–206, 2008.

[148] C. K. Boyce and J.-E. Lee, "Plant evolution and climate over geological timescales," *Annual Review of Earth and Planetary Sciences*, vol. 45, no. 1, pp. 61–87, 2017.

[149] S. J. Bourne, F. Brauckmann, L. Rijkels, B. J. Stephenson, A. Weber, and E. J. Willemse, "Predictive modelling of naturally fractured reservoirs using geomechanics and flow simulation," in *Abu Dhabi International Petroleum Exhibition and Conference*, pp. SPE–87253, SPE, 2000.

[150] M. C. Eppes, J. Aldred, S. Berberich, M. P. Dahlquist, S. G. Evans, R. Keanini, F. Moser, M. Morovati, S. Porson, M. Rasmussen, *et al.*, "Standardized field methods for fracture-focused surface processes research," *Earth Surface Dynamics Discussions*, vol. 2022, pp. 1–41, 2022.

[151] M. Rasmussen, *The Influence of Time, Rock Properties, and Climate on Mechanical Weathering.* Phd thesis, University of North Carolina at Charlotte, Charlotte, USA, 2024.

[152] K. Kurita and N. Fujii, "Stress memory of crystalline rocks in acoustic emission," *Geophysical Research Letters*, vol. 6, no. 1, pp. 9–12, 1979.

[153] Y. Nara, Y. Oe, S. Murata, T. Ishida, and K. Kaneko, "Estimation of long-term strength of rock based on subcritical crack growth," in *Engineering Geology for Society and Territory-Volume 2: Landslide Processes*, pp. 2157–2160, Springer, 2015.

[154] D. Li, J. Ma, Q. Wan, Q. Zhu, and Z. Han, "Effect of thermal treatment on the fracture toughness and subcritical crack growth of granite in double-torsion test," *Engineering Fracture Mechanics*, vol. 253, p. 107903, 2021.

[155] S. Nakagawa, Y. Zhang, M. Eskandari-Ghadi, and D. W. Vasco, "Inversion-based correction of double-torsion (dt) subcritical crack growth tests for crack profile geometry," *Theoretical and Applied Fracture Mechanics*, vol. 124, p. 103752, 2023.

[156] B. K. Atkinson, "Subcritical crack growth in geological materials," *Journal of Geophysical Research: Solid Earth*, vol. 89, no. B6, pp. 4077–4114, 1984.

[157] R. Charles, "Static fatigue of glass. ii," *Journal of Applied Physics*, vol. 29, no. 11, pp. 1554–1560, 1958.

[158] J. H. Perry, "Chemical engineers' handbook," 1950.

[159] C. H. Scholz, *The mechanics of earthquakes and faulting.* Cambridge university press, 2019.

[160] M. Rasmussen, M. C. C. Eppes, P. G. Meredith, R. Keanini, A. Mushkin, Y. Nara, A. J. Rinehart, U. Shaanan, and M. Dahlquist, "The influence of rock and environmental parameters on natural rock fracturing rates and characteristics," in *AGU Fall Meeting Abstracts*, vol. 2023, pp. EP23F–1993, 2023.

APPENDIX A: ESTIMATING GRAIN BOUNDARY BOND ENERGY, TENSILE STRENGTH AND MINIMUM BOND FRACTURE TEMPERATURE

Consider two adjacent cubical grains with a side length of d_g under a tensile load σ. Assume that the grain boundary is composed of a mono layer of atoms arranged in a square lattice with a side length of d_o, with an atom located at each corner. This mono layer represents the surface atoms of one grain in the pair. Therefore, the grain pair is bonded by $(N \cdot d_o)^2$ bonds, where $d_g = N \cdot d_o$.

Next, estimate the stress at which the bonds break, referred to as the rock tensile strength, σ_T, and label the mean energy of grain boundary bonds as ϵ_{gb}. The energy required to completely separate the two grains by fracture is then given by the following equation:

$$N^2 \epsilon_{gb} \sim \left(N \cdot d_o\right)^2 \sigma_T d_o \tag{5.1}$$

Solving for ϵ_{gb} finally gives us the following equation:

$$\epsilon_{gb} \sim \sigma_T d_o^3 \tag{5.2}$$

Using the parameters for granite given at the bottom of Table. 1, it is shown that grain boundary bond energies are approximately one-tenth of 1% of the bond energy of SiO2 as:

$$\epsilon_{gb} \sim 10^{-3}\ \epsilon_{SiO_2} \tag{5.3}$$

Where ϵ_{gb} is the grain boundary bond energy for granite and ϵ_{SiO_2} is the bond energy of silicon dioxide (SiO2). The key point is that the grain boundary bond energies, which govern the rock tensile strength according to the previous analysis, are remarkably weak compared to the bond energies within the SiO2 molecules that make up a significant portion of the granite material. This significant difference in bond energies (grain boundary bonds being much weaker than covalent bonds in SiO2) provides insights into the relatively low tensile strength and fracture behavior of granite, as the grain boundaries represent a weak point in the material's structure.

Finally, it can be readily shown using the argument in Section 3.13 that the minimum temperature required to break individual grain boundary bonds is given by:

$$T_{bond} \sim \frac{\epsilon_{gb}\,(1-\nu)}{\Delta\alpha E d_o^3} \tag{5.4}$$

Where ϵ_{gb} is the grain boundary bond energy, ν is Poisson's ratio, $\Delta\alpha$ is the difference in thermal expansion coefficients between adjacent grains, E is the Young's modulus and finally d_o is the atomic spacing or side length of the square array in the grain boundary monolayer. This temperature, i.e., T_{bond}, corresponds to the minimum temperature, T_{min}, required to cause thermoelastic fracture of the grain boundary.

APPENDIX B: ESTIMATING MINIMUM TEMPERATURES FOR THERMOELASTIC FRACTURE IN GRANULAR ROCKS

In granular rocks, subcritical fracture primarily occurs along relatively weak, atomically thin grain boundaries. The thermoelastic stress acting on the boundary between two dissimilar grains can be expressed as:

$$\sigma(T) = \left[\frac{E_2\alpha_2}{1-\nu_2} - \frac{E_1\alpha_1}{1-\nu_1}\right] T \tag{5.5}$$

Where T is the absolute temperature, E_1 and E_2 are Young's moduli of the adjacent grain pair, ν_1 and ν_2 are Poisson's ratios of the adjacent grain pair. Again, it should be noted that the adjacent grains are idealized as cubical in shape. In this equation, $\sigma(T)$ represents the thermoelastic stress acting on the grain boundary caused by the difference in thermal expansion properties between the adjacent grains. The thermoelastic stress scales linearly with temperature T and depends on the mismatch in the materials properties (Young's modulus E and Poisson's ratio ν) and thermal expansion coefficients (α_1 and α_2) of the two grains.

Next, assume that the characteristic thermal stress producing grain-scale subcritical fracture is on the order of the bulk tensile strength, σ_T as follows:

$$\frac{\bar{E}\Delta\alpha T_{min}}{1-\bar{\nu}} \sim \sigma_T \tag{5.6}$$

Where T_{min} is the minimum temperature producing fracture, $\Delta\alpha = \alpha_1 - \alpha_2$ is the difference in thermal expansion coefficients between the adjacent grain and finally $\bar{E}$ and $\bar{\nu}$ are the mean Young's modulus and mean Poisson's ratio, respectively, satisfying $E_1 \sim E_2 \sim \bar{E}$ and $\nu_1 \sim \nu_2 \sim \bar{\nu}$. Therefore, solving for T_{min} gives us:

$$T_{min} \sim \frac{\sigma_T(1-\bar{\nu})}{\bar{E}\Delta\alpha} \tag{5.7}$$

And using typical values $\sigma_T \sim 10$ MPa, $\bar{E} \sim 5 \times 10^4$ MPa$\sqrt{m}$, $\bar{\nu} \sim 0.8$, $\Delta\alpha \sim 3 \times 10^{-5}$ K^{-1} from Eppes et al. work [20], we obtain:

$$T_{min} \sim 5 \text{ K} \tag{5.8}$$

Based on the approximate formula in Eq. (5.11), only incipient fractures having diameters on the order of the effective grain boundary diameter, d_g, can grow at temperatures this low.

APPENDIX C: ESTIMATION OF MINIMUM GRAIN BOUNDARY CRACK DIAMETER FOR THERMOELASTIC FRACTURE

Consider a pancake-like grain boundary crack between two adjacent grains having mismatch material properties, subject to the thermal stress given by Eq. (5.5). Assuming that both terms within the bracket are of similar magnitude, we get:

$$\sigma(T) \sim \frac{\bar{E}\bar{\alpha}}{1-\bar{\nu}} \tag{5.9}$$

Where $\bar{E}$ is the mean Young's modulus, with $E_1 \sim E_2 \sim \bar{E}$, $\bar{\alpha}$ is the mean thermal expansion coefficient, with $\alpha_1 \sim \alpha_2 \sim \bar{\alpha}$ and $\bar{\nu}$ is the mean Poisson's ratio, with $\nu_1 \sim \nu_2 \sim \bar{\nu}$.

Using the expression for the position-dependent stress intensity, we assume a fracture propagates when the stress intensity factor K_I exceeds the bulk fracture toughness K_c as follows:

$$K_I(T) > K_c \Longrightarrow \frac{\bar{E}\bar{\alpha}T}{1-\bar{\nu}}\sqrt{d_{min}(T)} \sim \sigma_T\sqrt{30d_g} \tag{5.10}$$

In the above equation, $d_{min}(T)$ is the minimum incipient crack diameter required for crack growth initiation at absolute temperature T (thermal variations in material properties are neglected) and K_c is approximated as $K_c \sim \pi\sqrt{30d_g}\sigma_T$, where σ_T is the bulk tensile strength. The characteristic crack length at which critical fracture begins is $30d_g$, determined by matching $K_c \sim \pi\sqrt{30d_g}\sigma_T$ with a measured value of $K_c = 1.7$ MPa$m^{3/2}$ [9].

This analysis provides a framework for estimating the minimum incipient crack diameter $d_{min}(T)$ that can lead to fracture growth, considering the thermal stress,

stress intensity factor, bulk fracture toughness, and material properties. Therefore, using Eq. (5.10) and the parameter values characteristic of granite which can be found in the caption of Table 3.1 and solving for $d_{min}(T)$, we can get the following equation:

$$\frac{d_{min}(T)}{d_g} \sim \frac{10^3}{T^2} \tag{5.11}$$

where T is the absolute temperature in Kelvin (K). For the range of temperatures considered in Experiment 1, approximately 300 K $< T <$ 723 K, the minimum thermally activated crack diameters are bounded by:

$$10^{-3} < \frac{d_{min}(T)}{d_g} < 10^{-2} \tag{5.12}$$

Additionally, as a consistency check on the estimated minimum temperature $T_{min} \sim$ 5 K (from Table 3.1) at which microfracture is initiated, we solve Eq. (5.11) for the temperature T at which $d_{min} \to d_g$, gives $T \sim 33$ K.

APPENDIX D: ESTIMATING THE SMALLEST DETECTABLE GRAIN BOUNDARY FRACTURE SIZE IN GRANITE UNDER THERMAL STRESS

For granite, with its randomly heterogeneous grain structure, and given that grain boundary microfractures are atomically thin, we make the assumption that the smallest detectable projected fracture area falls within the same order of magnitude as the average projected area of individual grains. This is represented by the scaling relation as:

$$\sim 0.1 \cdot d_g^2 < A_{detect} <\sim d_g^2 \tag{5.13}$$

Where d_g is a characteristic grain size. The qualitative justification is that acoustic waves casting from fractures with areas smaller than $\sim d_g^2$ experience significant dissipation due to repeated refractions at the grain boundaries between the fracture site and the acoustic transducer used for detection. The upper limit in Eq. (5.13) assumes that, for the moderate temperatures considered in this study, thermal microfractures on average terminate at or near the grain boundary junctions where three or more adjacent grains meet along their boundaries. This represents a reasonable upper bound on the detectable fracture area within a polycrystalline material like granite.

The estimate given in Eq. (5.13) for the minimum detectable crack size is indirectly supported by experimental observations. In the experiment, the first detected cracks appeared at a temperature of approximately 300 K during the initial heating and cooling cycle.

The reasoning behind associating these first detected cracks with the area range $\sim d_g^2$ proposed in Eq. (5.13) is twofold:

1) Fractures with maximum area $\sim d_g^2$, release the maximum acoustic energy upon cracking.

2) Due to their size being on the order of an average grain diameter, these "pancake" fractures with area $\sim d_g^2$ have the highest transmissibility through the polycrystalline material, suffering less cumulative dissipation from repeated refractions at grain boundaries between the fracture site and acoustic transducer.

Therefore, we make the assumption that the first detected fracture events correspond to crack areas on the order of d_g^2, as cracks of this size optimally balance acoustic energy release and transmissibility enabling their detection.

The acoustic energy released, $E_{ac}(T)$, is related to the acoustic energy detected by a transducer, E_{det}, as:

$$E_{ac}(T)\frac{\Delta A_{trans}}{4\pi R^2} \sim E_{det} \tag{5.14}$$

The above equation relates the acoustic energy released at the crack site to the energy detected by the transducer, accounting for the geometric spreading of the acoustic wave over the distance R. Also we have:

$$E_{ac}(T) \sim E\alpha^2 d_m d_g^2 T^2 \tag{5.15}$$

Here, ΔA_{trans} is the area of the transducer, and R is the distance between the crack site and transducer, which is on the order of the sample diameter for the cylindrical samples used. Additionally, the approximations $E \sim E_1 \sim E_2$ and $\alpha \sim \alpha_1 \sim \alpha_2$ are made. Eq. (5.15) approximates the acoustic energy released as being proportional to material parameters like the elastic modulus E, thermal expansion coefficients α, grain size d_g, and temperature T, as well as a characteristic microscopic length d_m.

Focusing on Experiment 2 [3], we can obtain an estimate of the smallest fracture area detected, ΔA_{min}, by applying the energy balance relationship from Eq. (5.14) at the maximum temperature imposed, $T_{max} = 723$ K as follows:

$$E_{ac}(T_{max})\frac{\Delta A_{trans}}{4\pi R^2} \sim E_{det} \tag{5.16}$$

Where the acoustic energy released $E_{ac}(T_{max})$ can be approximated as:

$$E_{ac}(T_{max}) \sim E\alpha^2 d_m \Delta A_{min} T_{max}^2 \tag{5.17}$$

The same apparatus, sample rock type and dimensions, were used in Experiment 1. By rearranging the equations and using the detected acoustic energy, E_{det}, along with known material parameters and geometric factors, an estimate of the minimum detectable fracture area, ΔA_{min}, can be obtained for the maximum temperature cycle of Experiment 2 [3]. Since the right-hand sides of Eqs. (5.14) and (5.16) are equal, equating the left-hand sides gives us the following result:

$$\frac{\Delta A_{min}}{d_g^2} \sim \frac{(300)^2\ \text{K}}{(723)^2\ \text{K}} = 0.17 \tag{5.18}$$

This provides an estimate of the ratio of the minimum detectable fracture area, ΔA_{min}, to the square of the grain size, d_g^2, using the first observed fracture temperature of 300 K from the experiment. Alternatively, if we use a more typical threshold temperature of $T \sim 350$ K for the first observed acoustic emission events, we obtain:

$$\frac{\Delta A_{min}}{d_g^2} \sim \frac{(350)^2\ \text{K}}{(723)^2\ \text{K}} = 0.23 \tag{5.19}$$

Therefore, the qualitative estimate of detectable thermally generated crack sizes given by Eq. (5.13), which is valid for moderate temperatures not exceeding around 1000 K, is indirectly supported by these experimental observations relating fracture areas to detection temperatures.

APPENDIX E: CALCULATIONS REGARDING ENERGY EQUATION DERIVATION FOR ELASTIC DEFORMATION OF THERMALLY INDUCED ROCKS' MICROCRACKS

The derivation of the energy equation for elastic deformation of incipient microcracks in rock is based on a statement of conservation of energy for $\tilde{N}$ fixed mass rock samples within a canonical ensemble, as well as a continuum-based description of expansion-compression work within each sample. The primary simplifications, which are believed to be consistent with the conditions present in the heating and cooling experiments, are as follows:

1) Due to relatively small temperature variations which are $\Delta T \approx 50$ K in Experiment 1, plastic deformation remains negligible.

2) Due to small grains and relatively homogeneous grain structure, thermal expansion, as well as contraction during Experiment 1, are spatially isotropic.

3) Material properties are spatially homogeneous and fixed. Additionally, due to the small volumes of the samples, on the order of 10^{-5} m^3, and the small temperature variations, the work associated with thermoelastic deformation against gravity is neglected.

Importantly, based on work in another study [160], it is assumed that the thermally-induced formation of any given microcrack reflects a two-step process:

1) Elastic deformation of the solid rock surrounding the crack occurs at near-crack stresses that surpass the bulk rock's yield strength.

2) This is followed by the relaxation of near-crack stress due to the formation of microfractures.

In order to isolate the prefracture elastic deformation energy states, $E^{(k)}$, where $k = 1, 2, 3, ...$, whose enumeration is required to complete the statistical mechanics fracture model, any given rock sample is decomposed into a set of small solid volumes surrounding each incipient and thermally activated microcrack. Therefore, we have:

$$V_{crack,tot} = \sum_{j=1} \sum_{k=1} r_j^{(k)} \delta V^{(k)} \tag{5.20}$$

Where $\delta V^{(k)}$ is the volume of a thin solid shell surrounding a microcrack of volume $\delta V_{crack}^{(k)}$, and $r_j^{(k)} = j$ is the number of microcracks having volumes V in the range of $\delta V_{crack}^{(k)} \leq V < \delta V_{crack}^{(k)} + \Delta V$, in which $\Delta V / \delta V_{crack}^{(k)} \ll 1$. In other words, random microcrack volumes are grouped into bins of size ΔV to facilitate the analysis and modeling. The remainder of the sample volume, V_{solid}, is idealized as crack-free. Note that for clarity, an index referring to individual rock samples within an ensemble has been suppressed in the above equation.

Now, consider a set of $\tilde{N}$ rock samples located within an insulated enclosure, such as an air-filled container. Each rock sample undergoes the same unspecified surface heating-cooling process, denoted as $q_{surf}(t)$. The change in internal energy for these rock samples can be expressed by the following equation:

$$
\begin{aligned}
\tilde{E}\left(\tilde{N}, V, T\right) - \tilde{E}\left(\tilde{N}, V, T_o\right) = \\
\tilde{N}\left[\bar{Q}_{in} - \bar{Q}_{out}\right] - \sum_{p=1}^{\tilde{N}} \oint_{S_p} t_{(\mathbf{p})}^{(\hat{\mathbf{n}})} \cdot dx_{(\mathbf{p})} dA^{(p)} \\
- \sum_{j=1} \sum_{k=1} n_j^{(k)} r_j^{(k)} E^{(k)} + \sum_{j=1} \sum_{k=1} n_j^{(k)} r_j^{(k)} E_{crack}^{(k)}
\end{aligned}
\qquad (5.21)
$$

In this equation, $\tilde{E}(\tilde{N}, V, T)$ and $\tilde{E}(\tilde{N}, V, T_o)$ represent the internal energy at the final temperature T and the initial temperature T_o, respectively, for the given number of rock samples $\tilde{N}$ and volume V. Also, the right-hand side consists of four terms as follows:

1) $\tilde{N}[\bar{Q}_{in} - \bar{Q}_{out}]$ accounts for the net heat transfer into the rock samples, where $\bar{Q}_{in}$ and $\bar{Q}_{out}$ are the average heat input and output, respectively.

2) $\sum_{p=1}^{\tilde{N}} \oint_{S_p} t_{(\mathbf{p})}^{(\hat{\mathbf{n}})} \cdot d\mathbf{x}_{(\mathbf{p})} dA^{(p)}$ represents the elastic deformation including compression or expansion work done on each rock sample that is uncracked, involving the traction vector $t_{(\mathbf{p})}^{(\hat{\mathbf{n}})}$ and the surface area element $d\mathbf{x}_{(\mathbf{p})} dA^{(p)}$.

3) $\sum_{j=1} \sum_{k=1} n_j^{(k)} r_j^{(k)} E^{(k)}$ accounts for the energy released due to the formation of new crack surfaces, where $n_j^{(k)}$ is the number of cracks of type k on the j-th rock sample, $r_j^{(k)}$ is the corresponding crack surface area, and $E^{(k)}$ is the energy required to create a unit area of crack surface of type k.

4) $\sum_{j=1} \sum_{k=1} n_j^{(k)} r_j^{(k)} E_{crack}^{(k)}$ represents the energy associated with the formation of new crack surfaces, where $E_{crack}^{(k)}$ is the energy required to create a unit area of crack surface of type k.

In developing a statistical mechanics model for the temperature-dependent, crack-inducing elastic deformation states $E^{(k)}$, the left-hand terms and the first two right-hand terms in the energy equation, i.e., Eq. (5.21) are grouped together. These combined terms represent the energy exchanges between internal energy, heat transfer, and expansion/compression work occurring in the solid, non-cracked portions of each rock sample. The statistical mechanics model primarily addresses the random equilibrium fluctuations in the $E^{(k)}$ states, which are influenced by the last two terms which are the near-crack elastic deformation energy and the energy released during fracture of the samples.

In order to further connect the desired crack-inducing elastic deformation energy states, $E^{(k)}$, to the physical conditions in our experiments, we first interpret the terms in Eq. (5.21), and close by introducing a crucial approximation for the fracture-inducing elastic deformation term, $\sum_{j=1}\sum_{k=1}^{K_{max}} n_j^{(k)} r_j^{(k)} E^{(k)}$.

Note that the average internal energy change for each sample in the ensemble can be written using the following equation:

$$U\left(V,T\right)-U\left(V,T_o\right)=\frac{1}{\tilde{N}}\left[\tilde{E}\left(\tilde{N},V,T\right)-\tilde{E}\left(\tilde{N},V,T_o\right)\right] \tag{5.22}$$

In our experiments, we make certain assumptions regarding heat transfer. During the heating portion of each experiment, each sample is heated by a fixed surface heat flux, denoted as q_{in}. The natural convective cooling is facilitated by either a fixed convective heat transfer coefficient, $h_h(T)$, in Experiment 1. The convective heat transfer coefficients remain nominally fixed when the surface temperature variations, represented by ΔT, which drive natural convective air currents, are small relative to the initial air temperature, denoted as T_o. In Experiment 1, the ratio $\Delta T/T_o \approx 0.2$, indicating that the temperature variations are small compared to the initial air temperature. Similarly, in Experiment 1, the associated convective heat transfer coefficient for cooling, denoted as h_c, remains nominally fixed. Therefore, the mean thermal energy input into each sample, represented by $\bar{Q}_{in}$, and the mean thermal energy lost by each sample in Experiment 1, denoted as $\bar{Q}_{out}$, are given by the following formulas:

$$\bar{Q}_{in} = \bar{Q}_{in}\left(T\left(t\right)\right) = q_{in}\ A_{sample}\ t - \int_0^t h_h\left[T\left(t'\right) - T_o\right]\ A_o\ dt' \tag{5.23}$$

and

$$\bar{Q}_{out} = \bar{Q}_{out}\left(T\left(t\right)\right) = \int_{t_{heat}}^t h_c\left[T\left(t'\right) - T\left(t' = t_{heat}\right)\right]A_o\ dt' \tag{5.24}$$

where t_{heat} is the time when the sample's temperature reaches to its maximum value, and A_o is the lateral surface area of the cylindrical sample.

The next term to consider is the work energy lost during heat-induced thermal expansion, or gained during cooling-induced compression, within the solid, uncracked volume of sample p. This term is represented by the surface integral as follows:

$$\begin{aligned}
\sum_{p=1}^{\tilde{N}} \oint_{S_p} \mathbf{t}_{(\mathbf{p})}^{(\hat{\mathbf{n}})} \cdot \mathbf{dx}_{(\mathbf{p})} dA &= \sum_{p=1}^{\tilde{N}} \oint_{S_p} \sigma_{ij}^{(p)} n_j^{(p)} dx_i^{(p)} dA^{(p)} \\
&= \pm \sum_{p=1}^{\tilde{N}} \oint_{S_p} \left[\sigma\left(T\right) - \sigma\left(T_{ref}\right)\right] \delta_{ij} n_j^{(p)} dx_i^{(p)} dA^{(p)} \\
&= \pm \sum_{p=1}^{\tilde{N}} \oint_{S_p} \left[\sigma\left(T\right) - \sigma\left(T_{ref}\right)\right] n_j^{(p)} dx_j^{(p)} dA^{(p)} \\
&= \pm \sum_{p=1}^{\tilde{N}} \left[\sigma\left(T\right) - \sigma\left(T_{ref}\right)\right] \oint_{S_p} dV^{(p)} \\
&= \pm \left[\sigma\left(T\right) - \sigma\left(T_{ref}\right)\right] \tilde{N}\ \langle \Delta V \rangle
\end{aligned} \tag{5.25}$$

Where S_p represents the surface of the solid, uncracked volume of sample p, $\mathbf{t}_{(\mathbf{p})}^{(\hat{\mathbf{n}})}$ is the traction vector (surface force per unit area) acting on the surface in the outward normal direction $\hat{n}$, $\mathbf{dx}_{(\mathbf{p})}$ is the displacement vector field within the solid volume, $dA^{(p)}$ is the differential area element on the surface, $\sigma(T)$ is the thermal stress at temperature T, $\langle \Delta V \rangle$ is either the average volumetric expansion over the ensemble of $\tilde{N}$ samples as the ensemble is heated from $T_{ref} = T_o$ to T, or average volumetric contraction as the ensemble cools from $T_{ref} = T_{max}$ to T. Note that we choose the plus sign during heating/expansion and the minus sign during cooling/contraction phases. This surface integral calculates the work done by the traction forces on the surface due to the thermal expansion/compression displacements within the uncracked solid volume of sample p. To complete the microfracture model, the fracture-inducing elastic deformation term is approximated by the following equation:

$$\sum_{j=1} \sum_{k=1} n_j^{(k)} r_j^{(k)} E^{(k)} \approx \sum_q n_q r_q E_c \tag{5.26}$$

In this approximation, $n_j^{(k)}$ is the number of samples with $r_j^{(k)}$ near-crack regions undergoing elastic deformation, $E^{(k)}$, before microfracture in the original term, n_q represents the number of samples with r_q near-crack regions experiencing elastic deformation prior to microfracture, and finally E_c is a fixed elastic deformation energy, derived in Section 5.3.

This approximation is considered reasonable when the initial microcrack volumes $\delta V_1, \delta V_2, ...$ (evaluated at $T = T_o$ during heating or $T = T_{max}$ during cooling) are tightly clustered around a mean initial microcrack volume $\langle \delta V \rangle$, with small variance in δV_i about $\langle \delta V \rangle$. Given the relatively small temperature variations in the experiments and the visually uniform grain structure across samples makes the assumption to be valid. The key idea is replacing the sample-specific elastic deformations, $E^{(k)}$, with a fixed E_c, justified by the uniformity of initial microcrack volumes across the sample ensemble.

APPENDIX F: CALCULATIONS REGARDING DERIVATION OF ENERGY CONSTRAINTS FOR THERMAL AND MECHANICAL GRAIN BOUNDARY PREFRACTURE

In this section we try to derive a necessary constraint on the total thermal and mechanical energy exchanged within the $\tilde{N}$ samples in the ensemble, resulting in the following equation:

$$\begin{aligned}\tilde{E}\left(\tilde{N},V,T\right)-\tilde{E}\left(\tilde{N},V,T_o\right)= &\ \tilde{N}\left[\bar{Q}_{in}-\bar{Q}_{out}\right]-\textstyle\sum_{p=1}^{\tilde{N}}\oint_{S_p}\mathbf{t}_{(\mathbf{p})}^{(\hat{\mathbf{n}})}\cdot\mathbf{dx}_{(\mathbf{p})}dA^{(p)} \\ &-\textstyle\sum_{j=1}\sum_{k=1}n_j^{(k)}r_j^{(k)}E_c^{(k)}+\sum_{j=1}\sum_{k=1}n_j^{(k)}r_j^{(k)}E_{acoustic}^{(k)}\end{aligned} \tag{5.27}$$

The quantities $\tilde{E}(\tilde{N},V,T)$ and $\tilde{E}(\tilde{N},V,T_o)$ represent the total energy, including both thermal and mechanical components, contained within $\tilde{N}$ samples, each having volume V, at the temperatures T and T_o, respectively. T_o is a reference temperature. $\bar{Q}_{in}-\bar{Q}_{out}$ represents the average net heat transferred to or from each sample during an arbitrary, cyclic heat transfer process.

The term $\oint_{S_p}\mathbf{t}_{(\mathbf{p})}^{(\hat{\mathbf{n}})}\cdot\mathbf{dx}_{(\mathbf{p})}dA^{(p)}$ accounts for the total thermoelastic deformation experienced by the solid, non-porous, non-fractured portion of sample p during the process. $\sum_{j=1}\sum_{k=1}n_j^{(k)}r_j^{(k)}E_c^{(k)}$ quantifies the total pre-fracture thermoelastic deformation of the thin solid shells surrounding all grain boundary microfractures formed. $\sum_{j=1}\sum_{k=1}n_j^{(k)}r_j^{(k)}E_{acoustic}^{(k)}$ represents the total acoustic energy released due to these microfractures.

In this general model, grains can have any shape. At any absolute temperature T, elliptical grain boundary cracks can have a minor axis length $c^{(k)}$ ranging from the single-atom scale d_o up to the grain size d_g. The quantity $n_j^{(k)}$ is the number of samples containing $r_j^{(k)}$ elliptical grain boundary fractures, where $r_j^{(k)}$ can take values 1, 2, 3, etc. The superscript k indicates the minor axis length $c^{(k)}$. The energies $E_c^{(k)}$ and $E_{acoustic}^{(k)}$ are the prefracture deformation and post-fracture acoustic energies associated with each fracture process.

To establish an energy constraint on the distribution of rock samples in each prefracture elastic energy deformation state, $E_c^{(k)}$, a fixed grain boundary scaffold thickness, δ_{GB}, is chosen such that $E_c^{(k)}$ is much greater than $E_{acoustic}^{(k)}$. Considering each rock sample as composed of random crystalline grains embedded in the scaffold, the total thermoelastic deformation, the sum of the second and third terms on the right side of Eq. (5.27) is then approximately fixed at any temperature T.

From a physical standpoint, the scaffold is made sufficiently thick so that the total deformation energy of the scaffold dominates over the total acoustic energy released from atomically thin microcracks. Mathematically, we decompose second and third terms in Eq. (5.27) into:

$$\begin{aligned}
&\sum_{p=1}^{\tilde{N}} \oint_{S_p} \mathbf{t}_{(\mathbf{p})}^{(\hat{\mathbf{n}})} \cdot \mathbf{dx}_{(\mathbf{p})} dA^{(p)} - \sum_{j=1}\sum_{k=1} n_j^{(k)} r_j^{(k)} E_c^{(k)} = \\
&\pm\tilde{N}\left[\sigma\left(T\right) - \sigma\left(T_{ref}\right)\right]\ \langle \Delta V_{solid}\rangle\ \pm \tilde{N}\left[\sigma\left(T\right) - \sigma\left(T_{ref}\right)\right]\ \langle \Delta V_{scaff}\rangle - \\
&\sum_{j=1}\sum_{k=1} n_j^{(k)} r_j^{(k)} E_c^{(k)} = \pm\tilde{N}\left[\sigma\left(T\right) - \sigma\left(T_{ref}\right)\right]\ \langle \Delta V_{solid}\rangle\ - \\
&\sum_{\alpha=1}\sum_{\beta=1} n_\alpha^{(\beta)} r_\alpha^{(\beta)} E_{uc}^{(\beta)} - \sum_{j=1}\sum_{k=1} n_j^{(k)} r_j^{(k)} E_c^{(k)} \qquad (5.28)
\end{aligned}$$

Where the first two terms in the middle line express the mean thermoelastic deformation energies for the solid and scaffold portions of the ensemble rock samples, respectively. Here, $\langle \Delta V_{solid}\rangle = \langle \Delta V_{solid}(T)\rangle$ and $\langle \Delta V_{scaff}\rangle = \langle \Delta V_{scaff}(T)\rangle$ represent the mean change in volumes produced in the solid and scaffold at temperature T.

In the third line, the unfractured and fractured scaffold is discretized into N_{max} subvolumes, each encompassing a single incipient grain boundary fracture location. The sum over uncracked potential fracture sites uses the indices α and β, and the associated deformation energies for these sites are denoted as $E_{uc}^{(\beta)}$.

Since we are neglecting the acoustic energy term in Eq. (5.27), and because the heat transfer, deformation energy, and pre-fracture deformation energies (terms one, two, and three) are each fixed for any given heat transfer process and equilibrium temperature T, the total ensemble energy, $\tilde{E}(\tilde{N}, V, T)$, is also fixed. Consequently, we obtain a constraint on the scaffold deformation energy:

$$\sum_{\alpha=1}\sum_{\beta=1} n_{\alpha}^{(\beta)} r_{\alpha}^{(\beta)} E_{uc}^{(\beta)} + \sum_{j=1}\sum_{k=1} n_{j}^{(k)} r_{j}^{(k)} E_{c}^{(k)} = \tilde{F}\left(\tilde{N}, V, T\right) \tag{5.29}$$

where

$$\begin{aligned}\tilde{F}\left(\tilde{N}, V, T\right) = -\tilde{E}\left(\tilde{N}, V, T\right) + \tilde{E}\left(\tilde{N}, V, T_o\right) + \tilde{N}\left[\bar{Q}_{in} - \bar{Q}_{out}\right] \\ \pm \tilde{N}\left[\sigma\left(T\right) - \sigma\left(T_{ref}\right)\right]\left\langle \Delta V_{solid}\right\rangle\end{aligned}$$

From a physical perspective, Eq. (5.29) states that at any given temperature T and for any rock volume V, the total prefracture deformation energy within the scaffold, $\tilde{F}(\tilde{N}, V, T)$, which encompasses all rock grains, is a fixed quantity. In the present model, we idealize detectable cracks as having a fixed projected area, $A_c = (f \cdot d_g)^2$, where f is a factor and d_g is the grain size. This simplifies the penultimate term in Eq. (5.27) to:

$$\sum_{j=1}\sum_{k=1} n_j^{(k)} r_j^{(k)} E_c^{(k)} = \sum_{j=1} n_j r_j E_c \tag{5.30}$$

In this equation, $E_c = E_c(T)$ is the pre-fracture elastic deformation energy which depends on temperature (T).

APPENDIX G: CALCULATIONS OF CRACK MODEL-ENERGY REQUIRED TO OPEN A SINGLE CRACK

Initially, we assume that the coefficient of thermal expansion, α_1, for grain 1 is greater than α_2 for grain 2. We then impose a temperature change, ΔT, on both grains. Consequently, grain 1 will expand in one direction (for example, the Z direction) more than grain 2 due to the differences between thermal expansion coefficients (See Fig. (5.1)).

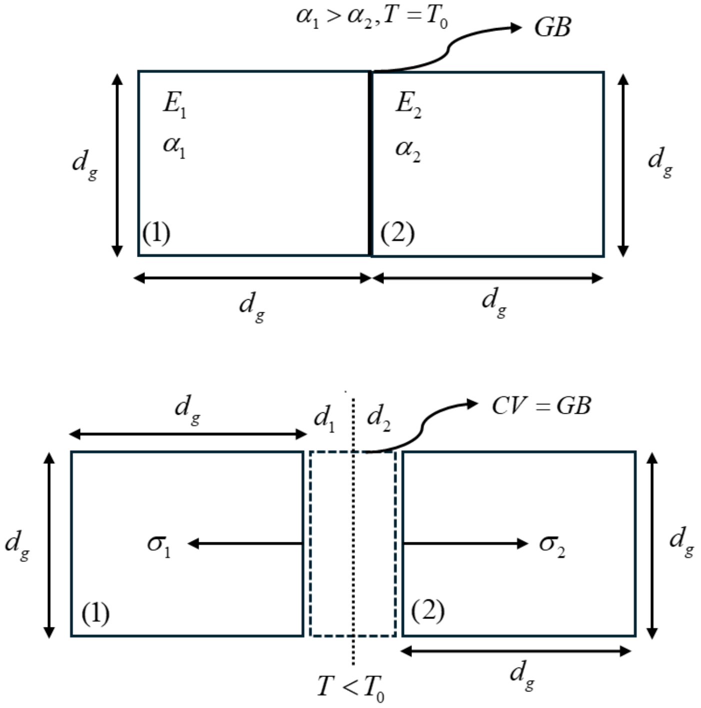

Figure 5.1: Schematic representation of two adjacent grains having different thermal expansion coefficients α_1 and α_2, showing grain boundaries (GB), control volume (CV), and dimensions under thermal conditions

The thermal stress pushing the top surface of grain 1 upward can be calculated using the following equation:

$$\sigma_1 = E_1 \times \alpha_1 \times \frac{\Delta T}{1 - \nu_1} \tag{5.31}$$

Similarly, the thermal stress pushing the top surface of grain 2 upward can be determined using the following equation:

$$\sigma_2 = E_2 \times \alpha_2 \times \frac{\Delta T}{1 - \nu_2} \tag{5.32}$$

Consider the scenario where the bottom (square) surfaces of both grains remain fixed at the same vertical location, z_0. Grain 1 expands in the vertical direction by a distance Δz_1, while grain 2 expands by Δz_2. During this thermal expansion process, the work-energy done on the thin vertical grain boundary separating the two grains is given by the following expression:

$$E_{\text{expansion}} = (\sigma_2 \times dA - \sigma_1 \times dA) \times (\Delta z_2 - \Delta z_1) = dA \times (\sigma_2 - \sigma_1) \times (\Delta z_2 - \Delta z_1) \tag{5.33}$$

Where $dA = d_g^2$ is the initial area of the two grains' vertical side area, with both grains having four vertical sides, each with an initial area of dA. Eq. (5.33) can be interpreted physically as follows:

The first term represents the "net" or "relative" vertical force pulling the vertical side area of grain 1 upward past the "effectively fixed/non-expanding" grain 2. The second term represents the "net/relative" vertical displacement of the vertically expanding grain 1 relative to the effectively fixed grain 2.

Therefore, Eq. (5.33) gives the total "shear" work done (in units of Newtons) on the thin grain boundary due to the temperature increase ΔT. Assuming that the thermal expansion is "elastic," which is the assumption for the relatively small temperature changes used in all three experiments, then the "thermoelastic" displacements Δz_1 and Δz_2 can be found as follows:

$$\sigma_1 = E_1 \times \varepsilon_1 \tag{5.34}$$

The equation provided above represents the fundamental constitutive relationship in linear elasticity theory, where ε_1 denotes the vertical strain experienced by grain 1, and its expression is given as follows:

$$\varepsilon_1 = \frac{\Delta z_1}{d_g} \tag{5.35}$$

In the given context, d_g represents the side length of the grain. By substituting Eq. (5.31) and Eq. (5.33) into Eq. (5.34), we can obtain the following equation:

$$E_1 \times \alpha_1 \times \frac{\Delta T}{1 - \nu_1} = E_1 \times \frac{\Delta z_1}{d_g} \tag{5.36}$$

Solving the last equation for Δz_1 finally yields the following equation:

$$\Delta z_1 = d_g \times \alpha_1 \times \frac{\Delta T}{1 - \nu_1} \tag{5.37}$$

Following the same steps for grain 2 gives the following equation:

$$\Delta z_2 = d_g \times \alpha_2 \times \frac{\Delta T}{1 - \nu_2} \tag{5.38}$$

In this context, ΔT is defined as $\Delta T = (T - T_0)$, where T is the current temperature and T_0 is the initial/reference temperature. It's important to note that for shear cracking, the reference length should be considered as d_l, implying that $d_g = d_l$. Furthermore, referring back to Eq. (5.33), by substituting σ_1 and σ_2 using Eqs. (5.31) and (5.32), respectively, and also substituting Δz_1 and Δz_2 by Eqs. (5.37) and (5.38), respectively, we can derive the following equation:

$$E_c^{(\alpha)} = f^{(\alpha)} \times d_g^3 \left[\frac{E_2^{(\alpha)}\alpha_2^{(\alpha)}}{1-\nu_2^{(\alpha)}} - \frac{E_1^{(\alpha)}\alpha_1^{(\alpha)}}{1-\nu_1^{(\alpha)}} \right] \left[\frac{\alpha_1^{(\alpha)}}{1-\nu_1^{(\alpha)}} - \frac{\alpha_2^{(\alpha)}}{1-\nu_2^{(\alpha)}} \right] \left(T - T_0^{(\alpha)} \right)^2 \quad (5.39)$$

There is one missing term in the equation, which is the pressure-dependent "fudge factor", denoted by f. This factor accounts for the effect of increasing confining pressure, P, which suppresses thermal expansion. Additionally, we consider the following two assumptions:

1) For any given mode α of grain boundary fracture, we postulate that the two grains involved are of a specific type, for example, quartz and feldspar, quartz and quartz, quartz and olivine, etc.

2) Mode 1 fractures occur for grain boundary pairs having the lowest bond energy at the grain boundary, while mode 2 has the next lowest grain boundary bond energy, and so on.

These assumptions relate to the characteristics of the grain boundaries and the fracture modes associated with them, based on the types of mineral grains involved and their bond energies at the grain boundaries.

We consider the case where the stress is spatially isentropic, having radial (r) and angular (θ) components. Therefore, the total stress can be written as follows:

$$\sigma(T) = \sigma_0 + \frac{E}{(1-\upsilon)}\alpha(T - T_0) \quad (5.40)$$

In this equation, σ_0 represents the spatially uniform, in-core stress distribution at the reference temperature $T = T_0$. $T = T(t)$ is the time-varying core sample temperature, which is assumed to be spatially uniform. E is the rock's bulk Young's modulus, ν is the rock's bulk Poisson's ratio, α is the rock's bulk thermal expansion coefficient, and T_0 is the reference temperature, typically taken as room temperature.

This equation describes how the total stress, $\sigma(T)$, in the rock sample depends on the initial stress, temperature change, and material properties such as Young's modulus, Poisson's ratio, and thermal expansion coefficient.

The stated equations relate the energy required to open a grain-scale crack, E_c, to various parameters such as thermal stress change, grain size, matrix thickness, and material properties like Young's modulus, Poisson's ratio, and thermal expansion coefficient.